

TECHNISCHE UNIVERSITÄT MÜNCHEN



WALTER SCHOTTKY INSTITUT

**Zentralinstitut für Physikalische Grundlagen
der Halbleiterelektronik**



**BERICHT
2008
ANNUAL REPORT**

Walter Schottky Institut, TU München, Am Coulombwall, 85748 Garching, Germany

Contents

	Preface	I
1.	The Walter Schottky Institut	V
2.	Scientific Activities	
	Basic Semiconductor Physics	1
	Charge and spin readout scheme for single self-assembled quantum dots	2
	A Schottky top-gated two-dimensional electron system in a nuclear spin free Si/SiGe heterostructure	4
	InAs nanowire and quantum dot arrays	6
	Density enhanced diffusion of dipolar excitons within a one-dimensional channel	8
	Optical detection of single-electron spin resonance in a quantum dot	10
	Dynamic photoconductive gain effect in shallow-etched AlGaAs/GaAs quantum wires	12
	Electrical control of spontaneous emission and strong coupling of a single quantum dot	14
	Dielectric screening versus quantum confinement of P-donors in silicon nanocrystals	16
	Asymmetry between absorption and photoluminescence line shapes of TPD: Spectroscopic fingerprint of the twisted biphenyl core	18
	Electrically controllable g factors in quantum dot molecules	20
	Materials Science	23
	Growth mechanisms of molecular beam epitaxy GaAs nanowires	24
	Prismatic heterostructures on GaAs nanowire facets	26
	Growth and characterization of ZnO/Zn _{1-x} Mg _x O quantum wells	28
	AlN growth on (100) and (111) diamond by plasma-assisted molecular beam epitaxy	30
	GaN/AlN and GaN/AlGaIn nanowire heterostructures grown by PAMBE	32
	Application of catalytic nanoparticles to gallium nitride surfaces	34
	Low temperature polycrystalline silicon prepared by aluminum-induced layer exchange for transistor applications	36
	Planar nanogap electrodes by direct nanotransfer printing	38
	Morphological and optoelectronic properties of pentacene thin films on hydrogen- and oxygen-terminated diamond substrates	40
	Light-induced charge transfer in hybrid composites of organic semiconductors and silicon nanocrystals	42
	Characterization of boron-doped nanocrystalline diamond electrodes for electrochemical applications	44
	Optoelectronic sensitization of carbon nanotubes by CdTe nanocrystals	46

	Device Physics	47
	Towards an electro-optically driven single photon device	48
	1.55 μm VCSEL with enhanced bandwidth and temperature range	50
	Low-threshold and high-performance injectorless quantum cascade lasers using four different material alloys	52
	Active regions for GaSb-based laser diodes in the mid-infrared wavelength range	54
	Low-resistive ohmic contacts to $n\text{-InAs}_{0.91}\text{Sb}_{0.09}$ for GaSb-based VCSELs in the mid-infrared range	56
	Single-mode (electro-)thermally tunable GaSb-based VCSEL with buried tunnel junction	58
	Calibration-free carbon monoxide sensor without separate reference cell using 2.3 μm VCSEL	60
	Principles of widely tunable MEMS VCSEL devices based on InP	62
	Planarization of overgrown tunnel junctions for InP-based VCSEL by MOVPE	64
	High-speed tuning in vertical-cavity surface-emitting lasers	66
	Quantum transport theory in Terahertz quantum cascade lasers	68
	Bioelectronics	71
	Diamond transistors for the recording of cell action potentials	72
	PNA functionalization of silicon nanowires for label-free DNA detection and PNA-PEG modified silicon platforms for applications in DNA microarrays	74
	Theoretical model for the detection of charged proteins with a silicon-on-insulator sensor	76
	A micron-sized nanoporous multifunction sensing device	78
	Alkylation of silicon carbide	80
	Electrochemical scanning tunneling microscopy for nanoscale studies at the solid/liquid interface	82
3.	Research Funding and Collaborations	85
4.	Members of the Institute, Postdocs, and Guest Scientists	92
5.	Doctorate, Diploma, Master, and Bachelor Theses	95
6.	Publications	99
7.	Invited Talks	113
8.	Courses and Seminars	120
9.	Selected Topics of Semiconductor Physics and Technology	124
	Addresses	132

Preface

Dear friends, partners, sponsors, and former members of the Walter Schottky Institut!

It is not only our obligation but also our pleasure to keep you updated and to inform you about the diverse scientific activities which took place at the WSI in the last year. So please have a look at our new Annual Report 2008, the 15th in a series started in 1994. In addition to concise summaries of ongoing research projects and their major results, you will also find hopefully interesting data about publications, collaborations, teaching activities, as well as the students and scientists who make the WSI the lively place that it is.

The year 2008 marked the 20th anniversary of the Walter Schottky Institut, and this special occasion was duly celebrated with a scientific colloquium and a great party on July 17th. We all enjoyed very much the scientific presentations of former members of the institute and of international scientists engaged in active collaborations with the WSI. Afterwards, several hundred people joined together in the inspiring atmosphere of a Bavarian beer tent for further in-depth discussions. Also, a special brochure about the scientific activities of the WSI was prepared for this event, particularly addressing a more general audience, which can be downloaded at the following URL address: <http://www.wsi.tum.de/downloads/festschrift.pdf>

As the number of members of the WSI has continued to grow from less than 100 scientists and students in the early 90ies to currently more than 150, appropriate space for laboratories and offices has become an everyday problem. Fortunately, because of the successful initiative of Gerhard Abstreiter for a new laboratory extension of WSI (Center for Nanotechnology and Nanomaterials), there is hope for significant improvements in the near future. This new annex to the WSI with 2000 m² of additional office and lab space is now under construction and should become operational in early 2010.

Despite of this continuous expansion of the WSI, we are very much committed to support and promote individual young scientists in their career. The success of this endeavor can be judged by its recognition within the international scientific community. We are, therefore, very pleased that the work of Dominique Bougeard, Roland Enzmann, Jonathan Finley, Michael Kaniber, and Dance Spirkoska has been honored with various national or international awards and prizes in 2008.

Finally, let me mention our annual Sommerfest with the traditional soccer tournament. This time, the teams of Gerhard Abstreiter and Christian Amann had qualified for the finals. However, even after extra time and penalty shoot-out still no winner could be identified. Since everybody was tired and hungry, it was decided to leave the WSI-Cup with the Amann team for another year.

I take this opportunity to thank all members of the Walter Schottky Institut for the hard work and dedication during the year and all our partners and friends for their continued support!

Garching, June 2009


Martin Stutzmann

Our PhD's of 2008



Andrea Friedrich



Oliver Dier



Georg Steinhoff



Emanuele Ucelli



Stefan Ahlers



Shivaji Dasgupta

1. The Walter Schottky Institute

Brief History

The Walter Schottky Institute (WSI) is a Central Institute of the Technical University of Munich (TUM). It was founded in order to strengthen the interaction between basic physics and semiconductor electronics research and development. After the decision was made to create such an interdisciplinary research institute in early 1986 it took about two years until the new laboratories became operational in May 1988. This exceptionally short time for planning and construction of a modern institute building was made possible by the excellent cooperation between the Siemens AG, the Bavarian ministries, and TUM.

Resources

The WSI building contains laboratories and offices with a total area of about 2400 m². It is well equipped with state-of-the-art facilities for semiconductor preparation, characterization, and device technology. The main resources are listed in the following:

Materials preparation and semiconductor technology

Epitaxy systems for GaAs, InP, GaSb, GaN/AlGaIn, and SiGe based heterostructures (MBE, CBE, plasma-induced MBE, MOCVD)

Ultrahigh purity GaAs MBE machine (electron mobilities > 10 Mio cm²/Vs)

UHV evaporation equipment for SiGe on glass

Plasma-enhanced Si-CVD

Pulsed laser processing

Laboratory for surface modification / biofunctionalization

250 m² class 100 clean room facility with photolithography, e-beam lithography, reactive ion etching, metallization

Characterization and spectroscopy tools

High resolution X-ray diffraction

Atomic force microscopy

Electron microscopy and EDX equipment

Photoluminescence and Raman spectroscopy (from IR to UV)

DLTS, Optical DLTS, CV-profiling

FTIR spectroscopy

X-ray photoelectron spectroscopy

High frequency parameter analyzers

Electron spin resonance (ODMR, EDMR)

Low temperature high magnetic field setups for magneto-transport and magneto-optics

Special characterization facilities for laser diodes

Computational facilities

High end workstations

Research groups

The number of researchers at the Walter Schottky Institut has grown continuously. Today it accommodates the research groups headed by **Gerhard Abstreiter, Markus-Christian Amann, Martin Brandt, Anna Fontcuberta i Morral, Jonathan J. Finley, Alexander Holleitner, Martin Stutzmann, and Peter Vogl**, with a total headcount of about 140, including junior research group leaders, scientific and technical staff, postdocs and visiting researchers, secretaries, and doctorate as well as diploma (master) students. Out of these, about 30 positions are funded by TUM, while basically all the doctorate positions are financed via research projects with external funding. Available laboratory and office space is by far not sufficient anymore and the WSI urgently needs an expansion. A new Center for Nanotechnology and Nanomaterials is currently in the planning stage and it is expected that this shared facility will become operational in fall 2010.

The main research interests are:

- Fabrication and characterization of new semiconductor materials, material combinations, as well as functionalisation of surfaces
- Development of novel methods for fabrication and characterization of nanostructures
- Basic physics with emphasis on electronic and optical properties of low dimensional systems
- Realisation of new semiconductor devices for applications in ultrafast electronics, optoelectronics, and as biological / chemical sensors
- Theory and simulation of modern semiconductor materials and devices

Experimental Semiconductor Physics I (Gerhard Abstreiter, Jonathan J. Finley, Anna Fontcuberta I Morral, Alexander Holleitner):

Research projects of these groups deal with various aspects of electronic and optical properties of low-dimensional, mesoscopic semiconductor structures, the heteroepitaxy of group IV and III-V semiconductors, the development of novel methods for lateral patterning and self assembly of quantum wires and quantum dots, the use of various analytical tools for the characterization of nanometer-sized structures in collaboration with external groups, as well as the fabrication and test of new, unconventional electronic and optoelectronic devices. Examples for basic research are optical spectroscopy of single quantum dots, cleaved edge overgrowth on GaAs, magnetotransport in ultrahigh mobility GaAs heterostructures as well as electronic transport and tunneling in edge channels and one-dimensional systems. Device and technology oriented work aims at novel concepts for charge and spin storage in quantum dots, coherent devices based on quantum dots for future quantum information technology, photonic crystal microcavities for efficient single photon sources and the test of semiconductor nanostructures for chemical/biological sensors. A new area of research is the controlled manipulation of oligonucleotides on gold surface for possible protein detection and the development of SOI based lab-on-a-chip systems. Also of increasing interest are carbon based nanostructures and combinations with organic molecules.

Semiconductor Technology (Markus-Christian Amann):

The research activities in this group are concentrated on modern technologies for III-V compound semiconductors and their use for developing advanced electronic and optoelectronic devices. This comprises the development of epitaxial, patterning, microstructuring, etching and coating techniques as well as the design and fabrication of semiconductor laser diodes and other photonic components. The applied material systems are GaAs-AlGaAs, InGaAsP-InP and antimonite based compounds that are grown with molecular beam epitaxy (MBE) and chemical beam epitaxy (CBE) with an accuracy in the nanometer regime. Device structuring in the 100-nm-range is obtained by using electron-beam lithography. Reactive ion etching enables the well-defined processing of the various devices with a high material selectivity of the etching rate. The group is also well equipped with evaporation and sputtering techniques for passivation and contacting of the devices. Among the key devices are single-mode and wavelength-tunable laser diodes for the wavelength range between 1300 and 2200 nm using lattice-matched and strained InGaAsP layers on InP substrates, InGaAsP and AlInGaAs vertical cavity surface-emitting laser diodes in the 1300-2000 nm wavelength range. Recent work also covers the development of wavelength-tunable laser diodes for wavelengths above 2 μm using antimonite based compounds and quantum cascade lasers in the range of 5 to 15 μm for gas sensing. In the field of high-frequency electronic devices, the generation of rf-output power at millimeter-wave frequencies up to 300 GHz is aspired. Active transit-time diodes as well as passive varactor structures for multipliers are investigated.

Experimental Semiconductor Physics II (Martin Stutzmann, Martin Brandt):

The work of this semiconductor physics group deals with various aspects of new and non-conventional semiconductor materials and material combinations:

- semiconductors with a wide bandgap (GaN, InGaN, AlGaN, diamond, SiC),
- disordered semiconductors (amorphous, nanocrystalline, and polycrystalline),
- advanced thin film systems (silicon-based luminescent layers, thin film solar cells, organic/anorganic heterosystems, biofunctionalized semiconductors, semimagnetic semiconductors)

Most of these material systems are prepared by suitable deposition techniques (MBE, Plasma-enhanced CVD, e-beam evaporation, sputtering). Their efficient optimization is based on the large pool of structural, optical, and electrical characterization techniques available in our institute. Complementary to the usual spectroscopic techniques we have developed and employ a variety of highly sensitive methods which enable us to study in particular the influence of defects on the electronic performance of materials and devices. Such techniques include subgap absorption spectroscopy, optically induced capacitance spectroscopy and, in particular, modern spin resonance techniques which are applied to various materials systems and devices for spintronics.

In addition to the preparation and characterization of new semiconductor materials we also work on the modification and processing of semiconductors with pulsed high power laser

systems (laser-crystallization, holographic nanostructuring, laser-induced etching) and investigate the potential of new material systems for novel device structures. Recent examples include nanostructured thin film solar cells, high electron mobility transistors based on AlGaN/GaN heterostructures, as well as UV-detectors, sensors and biosensors.

Theoretical Semiconductor Physics (Peter Vogl):

The activity of this group focuses on the theoretical study of structural, electronic and optical properties of semiconductors. The work deals with mesoscopic structures, new materials, and novel devices, in the attempt to understand their basic physics and to predict their behavior. The research conducted in the group aims at the development of theoretical tools which can support present experimental activities and propose new ideas and solutions for the future, as indicated by the strong interaction with industrial laboratories and with engineering university departments. Sophisticated quantum mechanical calculations are used for determining the electronic structures and the optical properties of a variety of semiconductor materials and systems. The information from such fundamental studies constitutes the basis for the analysis of the transport properties of such materials and for the development of reliable numerical tools for device modeling. Recent activities in this group include ab-initio studies of spin devices, prediction of novel magnetic field effects, development of multiscale methods for film growth, and the design and modeling of semiconductor based quantum information devices.

The research activity of the institute thus covers a wide spectrum from basic physics in low-dimensional semiconductor structures to the development of novel or improved electronic, optoelectronic and sensor devices based on semiconductor hetero- and nanostructures. The close collaboration between the different groups and the availability of various experimental techniques are the essential basis for the successful development of novel semiconductor devices. Close contacts with industrial partners have also proven to be very fruitful and stimulating in developing new ideas and in following new directions which may be relevant for future applications.

Apart from the extensive research activities all groups are involved in teaching within their respective departments. Besides the usual teaching responsibilities in undergraduate and graduate courses, special emphasis is put on the education of diploma and doctoral students in the physics and technology of present and future nano-devices and of low dimensional semiconductor structures.

Basic Semiconductor Physics

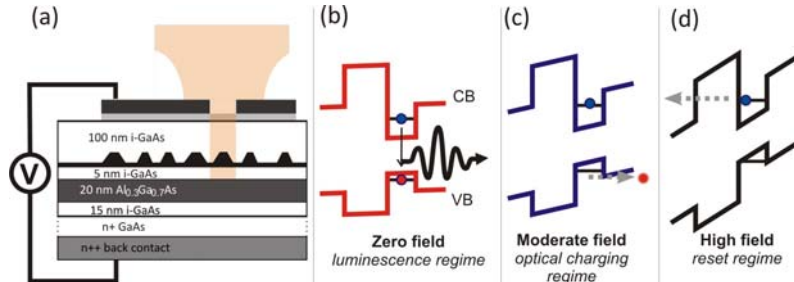
Charge and spin readout scheme for single self-assembled quantum dots

D. Heiss, V. Jovanov^{*}, F. Klotz, M. Bichler, G. Abstreiter, and J. J. Finley

We propose a new scheme for optical spin readout in self-assembled InGaAs QDs and experimentally demonstrate its feasibility. Our readout scheme would allow the investigation of spin relaxation and decoherence mechanisms over the long timescales, predicted by theory.

Our approach is based on a gateable single dot photodiode structure that can be switched between charge and readout modes [1]. In order to perform optical charging experiments on a single self-assembled QD, precise control of the local electric field is necessary. This can be achieved by embedding the dot in the intrinsic region of a Schottky photodiode structure formed by a heavily n -doped back contact and a 5-nm thick semitransparent Ti top contact with an extension of $200 \times 300 \mu\text{m}^2$. The epitaxial layer sequence of the devices investigated is depicted schematically in Fig. 1(a). To ensure that the tunneling escape of holes from the dot is much faster than that for electrons, thus, enabling optical charging, an asymmetric $\text{Al}_{0.3}\text{Ga}_{0.7}\text{As}$ barrier with a width of 20 nm was grown below the QD layer. By controlling the voltage V_{app} applied to the Schottky gate, the device can be operated in one of three regimes: (i) if the device is biased in forward direction so that the electric field across the QDs is small, both the tunneling times of electrons and holes are longer than the excitonic radiative lifetime τ_{rad} , and photoluminescence (Fig. 1(b)) will be observed.

Fig. 1: (a) Schematic of the sample structure. We distinguish three electric-field regimes: (b) The luminescence regime at low electric fields. (c) The hole tunneling at moderate electric fields leads to the charging regime. (d) The reset regime, where electrons tunnel to the back contact.

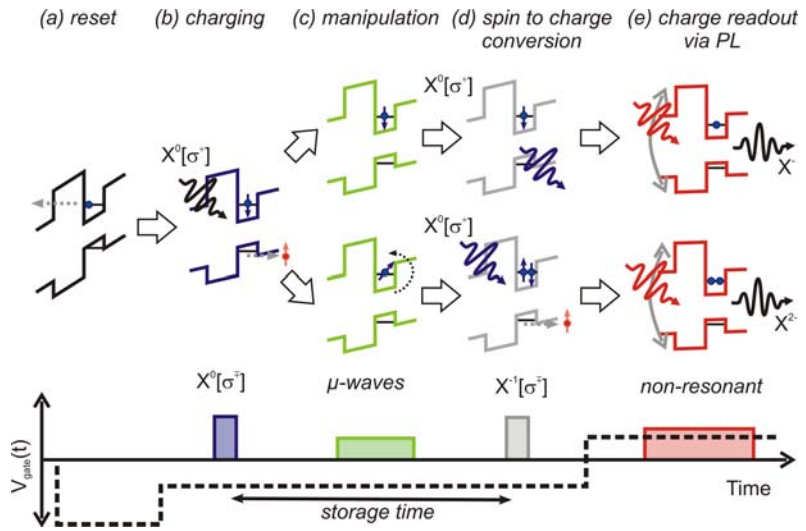


(ii) If the electric field is increased to the point where photogenerated holes tunnel out of the dot over timescales shorter than τ_{rad} , the dot charges up with electrons (Fig. 1(c)). (iii) If a large electric field is applied, electrons can tunnel through the AlGaAs barrier, hence, reducing the charge accumulation in the dot (Fig. 1(d)).

We proceed by proposing a spin readout mechanism for single dots based on this concept. Fig. 2 illustrates schematically a scheme for spin generation, manipulation, initialization, and readout. Each measurement cycle starts by resetting the QD to an empty state to avoid cumulative errors. This is done simply by applying high electric fields that ensure tunneling escape of the electrons (Fig. 2(a)). Following this, the field is reduced to switch the device into charging mode and a single electron with a defined spin orientation is optically pumped into the QD, illuminating the device with laser light tuned to the X_0 transition.

^{*}phone: +49-89-289-13882, fax: +49-89-320 6620, email: jovanov@wsi.tum.de

Fig. 2: Schematic of the spin readout scheme. The individual steps are: (a) reset by fast electron tunneling, (b) charging with resonant excitation followed by hole tunneling, (c) spin manipulation with, e.g., microwave pulses, (d) spin to charge conversion by spin-conditional resonant absorption, and (e) charge readout via nonresonant photoluminescence.



Using circularly polarized light, the spin orientation of the optically generated electron is controlled by the helicity of the polarization (Fig. 2(b)) and, for the purposes of illustration, in Fig. 2, we depict the creation of a spin-down electron using σ^+ polarized light. Following initialization, the spin can be stored, thermally relax, or be externally manipulated, for example, using microwave pulses for a time $\Delta\tau_{\text{store}}$. In Fig. 2(c) we schematically depict a π -rotation of the spin in the lower row while the spin in the upper row of images remains unchanged. After such controlled manipulation, the spin orientation is measured by applying a second circularly polarized laser pulse tuned to the X^- transition. A laser pulse at X^- with σ^+ helicity would create an additional spin-down electron if the spin orientation of the resident electron is up while the charge status would remain unperturbed if the resident electron is spin down. This step performs a spin-to-charge conversion: after the optical pulse tuned to X^- , one or two electrons populate the dot depending on the spin projection of the resident electron. In a final step in the measurement, the device is biased away from the optical charging regime and time integrated PL is used to nonperturbatively test the charge occupancy ($1e$ or $2e$) and, thus, the spin orientation of the resident electron. The charge state of the dot can be deduced with high fidelity from the relative intensity of the X^- or the X^{2-} luminescence lines since, as our results show, PL readout only weakly disturbs the charge state of the dot for timescales up to $100 \mu\text{s}$. While this destructive measurement technique is probably not suited for single shot measurements, a systematic optimization of the experimental setup and the sample design, as well as the implementation of photonic band-gap materials or solid immersion lenses, could increase the luminescence yield by up to three orders of magnitude and allow an increase of the storage time accordingly.

[1] D. Heiss, V. Jovanov, M. Bichler, G. Abstreiter, and J. J. Finley, Phys. Rev. B **77**, 235442 (2008)

A Schottky top-gated two-dimensional electron system in a nuclear spin free Si/SiGe heterostructure

Jürgen Sailer, Volker Lang, Gerhard Abstreiter, and Dominique Bougeard¹

Quantum dots offer a promising two-level system for applications in solid state based quantum information processing. In III-V-materials, electrostatically defined quantum dots are a well studied system. A major source of decoherence in such devices is the interaction of the confined electron spin with the surrounding semiconductor host matrix, in particular with the nuclear spin bath. Isotopical purification of the group-IV source materials Si and Ge can give access to virtually nuclear spin free materials.

Recently, we have reported on the realization and reliable gating of two-dimensional electron systems (2DES) in a nuclear spin free environment [1]. A 2DES forms in a strained ^{28}Si layer embedded into $^{28}\text{Si}^{70}\text{Ge}$. The ability to control the 2DES via top-gates is demonstrated by the implementation of split-gate structures which are able to locally deplete the 2DES.

The inset in Figure 1 shows the typical layout of our isotopically engineered Si/SiGe heterostructures. A SiGe virtual substrate with natural isotopic composition is first deposited onto a (100) oriented Si substrate. The virtual substrate is fully relaxed within the experimental error of 10% and typically displays a density of threading dislocations of about 10^6 cm^{-2} . The active part is then realized in the same fabrication process but from isotopically purified material. It is composed of a 15 nm thick, fully strained and dislocation free ^{28}Si layer embedded

into a $^{28}\text{Si}^{70}\text{Ge}$ cladding. The lower part of the cladding separates the nuclear spins of the virtual SiGe substrate from the 2DES. The upper part of the cladding contains a modulation doping realized with a 15 nm $^{28}\text{Si}^{70}\text{Ge}$ spacer layer and a 15 nm volume doped $^{28}\text{Si}^{70}\text{Ge}:\text{P}$ layer. Finally, the active part of the heterostructure is capped with 45 nm natural SiGe and protected against oxidation by a 10 nm thick Si layer on top. Fig. 1

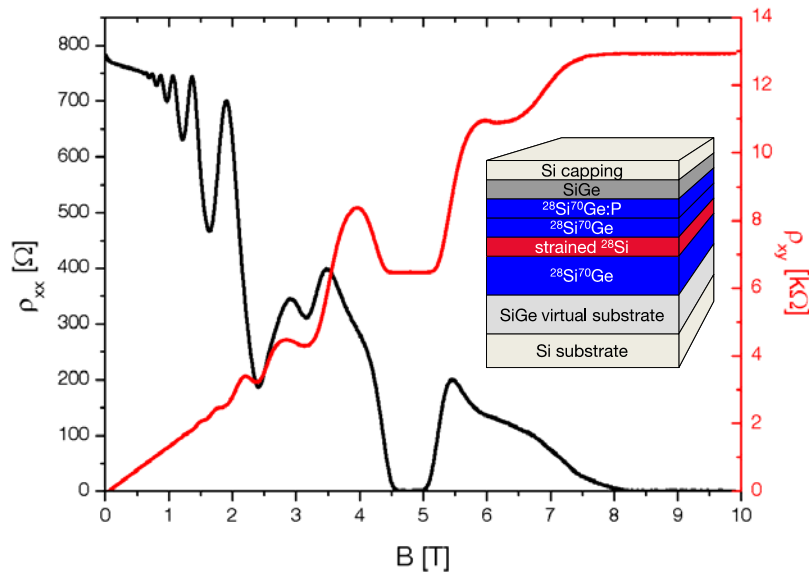


Fig. 1: Longitudinal (black) and transversal (red) Hall resistance for the isotopically engineered 2DES measured at $T = 340 \text{ mK}$. Inset: Layer structure of the isotopically engineered Si/SiGe heterostructure.

shows a typical result obtained during a magnetic-field sweep from $B = 0 \text{ T}$ to $B = 10 \text{ T}$ at

¹phone: +49-89-289-12777, email: bougeard@wsi.tum.de

340 mK after illumination of the sample until saturation of the charge carrier density. Relevant parameters deduced from the measurement prove the high quality of the 2DES. The zero-field Hall mobility of the sample shown in Fig. 1 amounts to $18000 \text{ cm}^2/\text{Vs}$ at a 2D sheet carrier density of $4.6 \cdot 10^{11} \text{ cm}^{-2}$. Shubnikov-de Haas oscillations in ρ_{xx} start to develop at B-fields as low as 0.6 T and show the 4-fold periodicity characteristic for 2DES in Si/SiGe, originating from both, the valley- and spin-degeneracy. The highest filling factors observed are 32 in ρ_{xx} and 12 in ρ_{xy} . Spin split levels can be resolved for filling factors lower than 10. In the high B-field regime, two very well defined quantum Hall effect plateaus with corresponding minima of the Shubnikov-de Haas oscillations for filling factors four and two are visible. Our structures show no sign for any parallel conduction which might for example arise in the dopant supply layer. This absence of parallel conduction has additionally been confirmed by Hall mobility spectrum analysis measurements. The remarkable Hall resistance overshoot visible before filling factors 3, 4, 6 and 8 is generally observed in our Si/SiGe heterostructure 2DES with narrow Hall bars and is not induced by the use of isotopically enriched source material.

Electron beam written symmetric split gates with tip-to-tip distances ranging from 130 nm to 200 nm have been realized on nuclear spin free 2DES with palladium (Pd). The Pd gates proved to be very stable and reliable over time even after several thermal cycles of the sample between room temperature and cryogenic temperatures. For all samples, the leakage current of the Pd gates was below the detection limit of 2 pA of our measurement setups for the whole range of operation of the gates. Remarkably, the Pd gates deplete the 2DEG underneath already at zero applied. Fig.2 shows results obtained for electrical transport along a narrow conducting channel defined by the narrowest and the widest, 130 nm and 200 nm wide, nano-constrictions fabricated on one Hall-bar. The measurements have been taken on different days. Complete pinch-off of the narrow conducting channels is achieved for gate voltages as low as -0.6 V and 0.5 V respectively, opening the possibility to design a Schottky top-gated quantum dot in a nuclear spin free environment.

- [1] J.Sailer, V. Lang, G. Abstreiter, G. Tsuchiya, K. M. Itoh, J. W. Ager III, E. E. Haller, D. Kupidura, D. Harbusch, S. Ludwig, and D. Bougeard *Physica status solidi Rapid Research Letters* **3**, No. 2, 61-63 (2009)

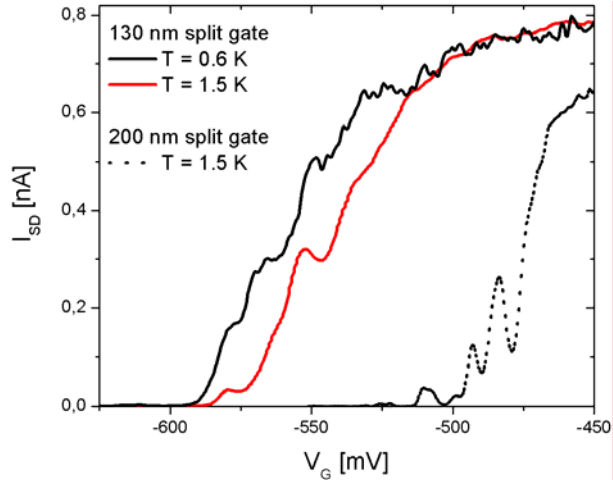


Fig. 2: Transport through two different split-gates defined on the same isotopically engineered Si/SiGe heterostructure. Measurements have been done after different cool-downs of the sample and in two different measurement setups.

InAs nanowire and quantum dot arrays

Emanuele Uccelli, Matthias Fehr, Max Bichler, Gerhard Abstreiter, Anna Fontcuberta i Morral

We present experimental results on the controlled synthesis of InAs ordered nanostructures with three different grades of complexity: nanowire, quantum dot (QD) arrays, and double quantum dot arrays. These nanostructures are obtained by combining the atomic resolution capabilities of Molecular Beam Epitaxy (MBE) and the Cleaved Edge Overgrowth (CEO) technique. CEO permits to grow InAs on a freshly *in situ* cleaved surface. We have used pre-structured (001) substrates with AlAs and GaAs quantum wells, which give AlAs and GaAs (110) oriented nanostructures upon cleaving.

We have studied the growth mechanism of InAs on the above mentioned AlAs/GaAs patterned (110) surfaces [1]. Detailed investigations of the different growth parameters and conditions have permitted to control in a reproducible way the formation of InAs QD chain, obtaining a low broadening in the QD dimensions and also avoiding the undesired formation of large InAs defects, which naturally nucleate on the (110) GaAs surface. Furthermore, InAs nanowire and dual QD chains have been realized by combining deposition of different amounts of InAs with a wide range of AlAs stripe thicknesses. Typically, InAs nanowires form on very narrow AlAs stripes (<15nm), while QD chains appear on larger AlAs stripes (15-50nm), even by deposition of nominal 1 monolayer of InAs (Fig. 1). For wide AlAs stripes (>50nm), parallel double-chains of QD grow on the same stripe.

The InAs height increases with the AlAs stripe thickness for both NWRs and QD chains. By carefully analyzing the growth results, we have been able to understand the growth mechanism of selective nucleation of these nanostructure arrays as function of the growth parameters. This has enabled us to reproducibly synthesize the InAs nanostructures with the desired geometry and to develop a comprehensive growth model, based on the different properties of In and As adatom characteristics on the AlAs and GaAs layers, and on the InAs mass redistribution on the AlAs/GaAs stripes surface [2].

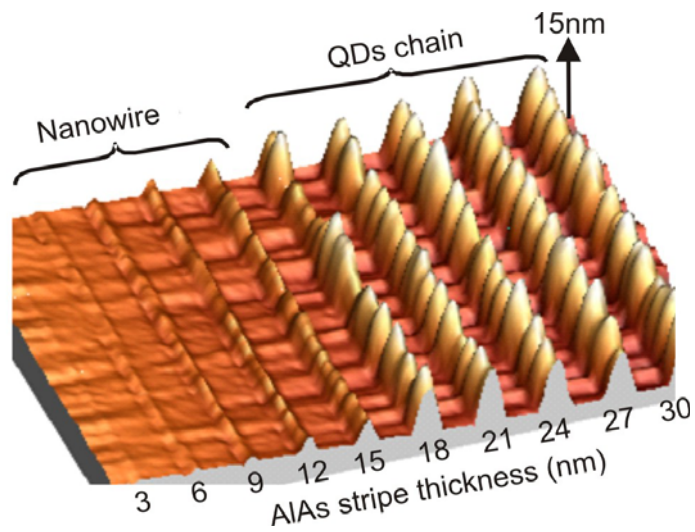


Fig. 1: Three-dimensional atomic force micrograph of a cleaved facet with AlAs stripes of widths from 3 to 30 nm, after having nominally grown 1.0 ML of InAs. The formation of InAs nanowire structures on AlAs stripes narrower than 15 nm and InAs QD chains on larger AlAs stripes is observed.

A contacting scheme of the obtained InAs nanostructures has been developed. In this case the InAs nanowire or QDs chain has been grown on a AlAs quantum well hosting a two dimensional electron gas (2DEG) [3]. In a transistor-like schematic of the device (Fig.

2a), the AlAs 2DEG acts as a contact to the InAs nanostructure. A top gate is used to deplete the 2DEG, thereby defining the InAs nanostructure as a channel between source and drain. Electrical measurements at low temperature show that the linear source-drain ($V_{sd}=0$) conductance G can be controlled by changing the top gate bias (Fig. 2b). At the threshold voltage $V_T=-1.52\text{V}$, G approaches zero as the AlAs 2DEG channel is pinched off. Furthermore, the conductance trace does not exhibit a stepwise increase or plateaus at discrete conductance values typical for conductance quantization in one-dimensional systems, meaning that the InAs nanowire is electrically isolated from the AlAs 2DEG leads by a broad depletion zone. Numerical calculations of the electron density and the device band structure confirm that a depletion zone is present in the AlAs layer close to the cleaved edge and the InAs nanowire. The latter is a result of a local redistribution of electrons to the InAs nanowire, thereby depleting the 2DEG. Additional doping of the CEO barrier layer should increase the electron density in the depletion region but does not remove the barrier completely. Further device concepts like a side gate on the CEO facet have been proposed, which should enable a defined control of the electric field at the cleavage plane.

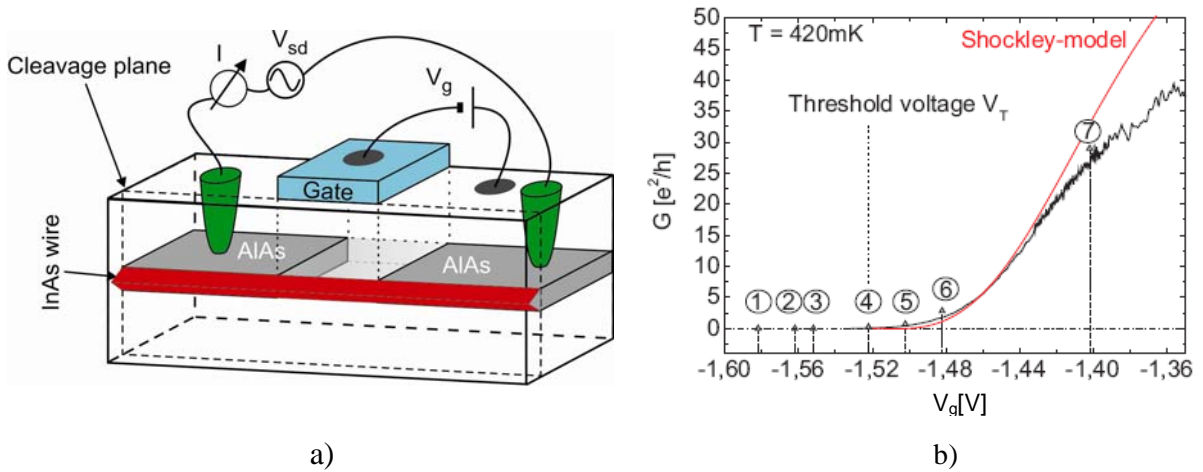


Fig 2: a) Drawing of the device proposal. A 2DEG hosted in the AlAs layer is used to contact the InAs nanowire on the cleaved edge. A gate on top of the sample splits the 2DEG into two parts. b) Source-drain conductance as function of the top-gate voltage for a 12nm thick InAs NWR.

- [1] E. Uccelli, M. Bichler, S. Nürnberg, G. Abstreiter, and A. Fontcuberta i Morral, *Nanotechnology* 19, 045303 (2008).
- [2] E. Uccelli, S. Nürnberg, M. Bichler, G. Abstreiter, and A. Fontcuberta i Morral, *Superlattices and Microstructures* 44, 425 (2008).
- [3] M. Fehr, E. Uccelli, S. Dasgupta, M. Bichler, L. Steinke, G. Abstreiter, M. Grayson, and A. Fontcuberta i Morral, accepted by *physica status solidi a*.

Density Enhanced Diffusion of Dipolar Excitons within a One-Dimensional Channel

X. P. Vögele¹, D. Schuh², W. Wegscheider², J. P. Kotthaus¹, and A.W. Holleitner

Excitons with the electron and the hole separated in two different quantum wells are called dipolar excitons. A small tunnel barrier between the quantum wells causes a relatively long recombination lifetime of the dipolar excitons of up to several microseconds [1]. This property and the fact that the excitons are bosons, makes it interesting to investigate the collective properties of dipolar excitons like superfluidity and Bose-Einstein condensation at high exciton densities and low temperatures. To achieve a high dipolar exciton density it is necessary to trap them within the two-dimensional (2D) quantum well plane.

Recently, A. Gärtner et al. reported on a new method to trap dipolar excitons within one-dimensional (1D) channels [Figure 1(a)] [2],[3]. The channel exhibits an almost harmonic trapping potential [Figure 1(b)]. Now, X. Vögele et al. investigated the lateral expansion of the excitons along such a one-dimensional channel and compared the corresponding dynamics to the exciton expansion in the free two-dimensional quantum well [4]. In two dimensions X. Vögele observe an exciton expansion that obeys non-linear temporal dynamics due to the repulsive dipole pressure at a high exciton density, in accordance with recent reports. In contrast, the observed one-dimensional expansion behaves linearly in time even at high exciton densities. The corresponding one-dimensional diffusion coefficient exceeds the one in two dimensions by far and depends linearly on the exciton density. X. Vögele et al. attributed the findings in one dimension to an effective screening of quantum well disorder by the dipolar excitons [4].

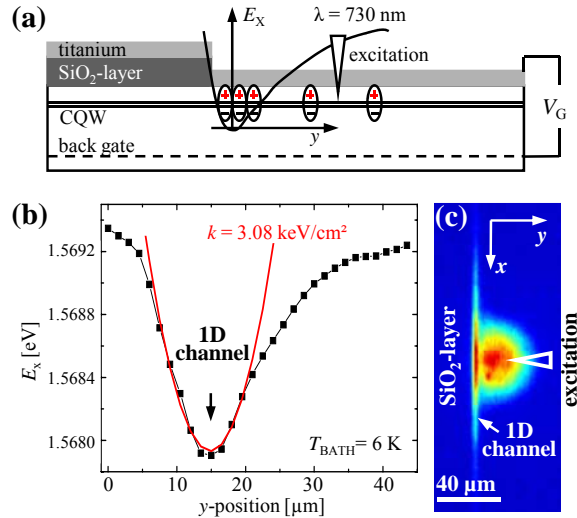


Fig. 1. (a) Sample sketch. Bent line symbolizes 1D trapping potential below the perimeter of a SiO₂-layer on top of a coupled quantum well (CQW) [2,3]. Dipolar excitons are excited at the triangle. (b) Recombination energy E_x of the excitons as a function of the y -position in (a). (c) Spatial image of a typical spatial photoluminescence (PL) distribution of such a circuit. Dashed line indicates the edge of the SiO₂-layer [4].

¹Lehrstuhl für Festkörperphysik Prof. Dr. Jörg. P. Kotthaus, Ludwig-Maximilians-Universität München, Geschwister-Scholl Platz 1, 80539 München.

²Institut für Angewandte und Experimentelle Physik II, Lehrstuhl Prof. Dr. W. Wegscheider, Universität Regensburg, Universitätsstr. 31, 93040 Regensburg.

- [1] A. Gärtner, A. W. Holleitner, J. P. Kotthaus, D. Schuh, Appl. Phys. Lett. 89, 052108 (2006).
- [2] A. Gärtner, L. Pecht, D. Schuh, A. W. Holleitner, J. P. Kotthaus, Phys. Rev. B 76, 085304 (2007).
- [3] A. Gärtner, D. Schuh, A. W. Holleitner, J. P. Kotthaus, Phys. E 40, 1828 (2008).
- [4] X. P. Vögele, J. P. Kotthaus, D. Schuh, W. Wegscheider, A. W. Holleitner, arxiv:0901.4875

Optical Detection of Single-Electron Spin Resonance in a Quantum Dot

Martin Kroner¹, Kathrina M. Weiss¹, Benjamin Biedermann¹, Stefan Seidl¹, Stephan Manus¹, Antonio Badolato², Pierre Petroff², Brian Gerardot³, Richard J. Warburton³, Khaled Karrai¹, Alexander W. Holleitner

In this project, semiconductor quantum dots have been investigated, which can be optically manipulated with high precision [1-5]. In particular, M. Kroner et al. demonstrated for the first time optically detected spin resonance of a single electron confined to a self-assembled quantum dot [6].

The quantum dot is rendered dark by resonant optical pumping of the spin with a laser. The optical contrast is restored by applying a radio frequency (rf) magnetic field at the spin resonance [Fig. 1(a)]. The scheme is sensitive even to rf-fields of just a few μT . M. Kroner et al. showed that the spin resonance in quantum dots can behave as a driven 3-level λ -system with weak damping [6]. In another case, Martin Kroner et al. demonstrated that quantum dots can exhibit remarkably strong (67% signal recovery) and narrow (0.34 MHz) spin resonances with fluctuating resonant positions, evidence of unusual dynamic processes [Fig. 1(b)] of electron states in self-assembled quantum dots.

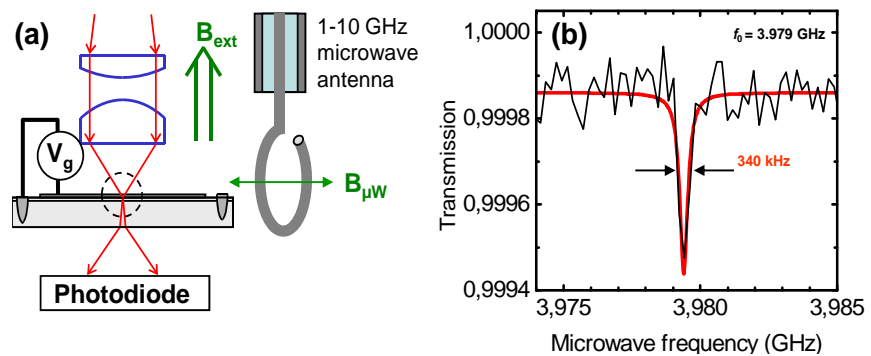


Fig. 1. (a) Schematic of experimental setup used in ref.[6]. The laser excitation at wavelengths around 950 nm is focused onto the sample with an objective with numerical aperture 0.5 and gives a spot size of $\sim 1\mu\text{m}$ at the sample. The transmitted light is detected with an in situ photodiode. A dc magnetic field, B_{ext} , is applied perpendicular to the sample. An ac magnetic field, $B_{\mu\text{W}}$, is generated with a closed loop antenna of diameter 2 mm positioned 2 mm along its axis from the quantum dot. The loop is connected to a microwave oscillator via a high frequency cable. The objective, sample, and antenna are all at 4.2 K. (b): Optically detected spin resonance for a self-assembled quantum dot at $B_{\text{ext}} \sim 0.5\text{ T}$: Optical transmission versus microwave frequency at zero optical detuning showing electron spin resonance (ESR) close to 3.98 GHz.

- [1] M. Kroner, C. Lux, S. Seidl, A. W. Holleitner, K. Karrai, R. J. Warburton, A. Badolato, P.M. Petroff, Appl. Phys. Lett. 92, 031108 (2008).
 [2] S. Seidel, M. Kroner, C. Lux, S. Seidl, A. W. Holleitner, K. Karrai, R. J. Warburton, A. Badolato, P.M. Petroff, Appl. Phys. Lett. 92, 153103 (2008).

¹ Center for NanoScience (CeNS), Fakultät für Physik, and Lehrstuhl für Festkörperphysik Prof. Dr. Jörg. P. Kotthaus, Ludwig-Maximilians-Universität, Geschwister-Scholl Platz 1, 80539 München, Germany.

² Materials Department, University of California, Santa Barbara, California 93106, USA.

³ School of Engineering and Physical Sciences, Heriot-Watt University, Edinburgh EH14 4AS, United Kingdom.

- [3] S. Seidl, B. D. Gerardot, P. A. Dalgarno, K. Kowalik, A. W. Holleitner, P. M. Petroff, K. Karrai, R. J. Warburton, *Phys. E* 40, 2153 (2008).
- [4] M. Kroner, S. Remi, A. Högele, S. Seidl, A.W. Holleitner, R.J. Warburton, B.D. Gerardot, P.M. Petroff, K. Karrai, *Phys. E* 40, 1994 (2008).
- [5] M. Kroner, K.M. Weiss, B. Biedermann, S. Seidl, A.W. Holleitner, A. Badolato, P.M. Petroff, P. Öhberg, R.J. Warburton, K. Karrai, *Phys. Rev. B* 78, 075429 (2008).
- [6] M. Kroner, K. M. Weiss, B. Biedermann, S. Seidl, S. Manus, A. W. Holleitner, A. Badolato, P.M. Petroff, B.D. Gerardot, R.J. Warburton, and K. Karrai, *Phys. Rev. Lett.* 100, 156803 (2008).

Dynamic photoconductive gain effect in shallow-etched AlGaAs/GaAs quantum wires

Klaus-Dieter Hof¹, Clemens Rössler¹, D. Schuh², W. Wegscheider², J. Simon, S. Ludwig¹, J. P. Kotthaus¹, and A.W. Holleitner

K.-D. Hof et al. discovered a dynamic photoconductive gain effect in quantum wires which are lithographically fabricated in an AlGaAs/GaAs quantum well via a shallow-etch technique

[1,2]. The effect allows resolving the one-dimensional subbands of quantum wires as maxima in the photoconductance of the quantum wires. K.-D. Hof et al. interpreted their results by the dominating influence of optically induced holes in the valence band of the quantum well which shift the chemical potential of the quantum wire [2,3]. Hereby, the circuit in Figure 1 allows exploring charge dynamics at the transition of two-dimensional and one-dimensional electron systems [4,5]. The non-linear current-voltage characteristics of the quantum wires allowed K.-D. Hof et al. also detecting the photoconductive gain effect of the excess charge carriers in the conduction band of the quantum well. The dynamics of the photoconductive gain are limited by the recombination time of both electrons and holes [2].

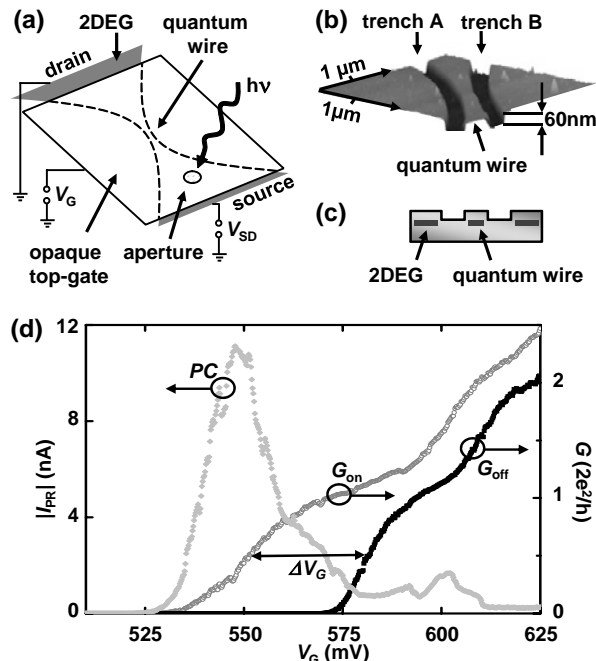


Fig. 1. (a) Experimental circuit to detect the photoconductive gain effect in low-dimensional circuits: A lateral constriction of a 2DEG forms a quantum wire between source and drain contacts. The central area of the device is covered with an opaque gate (bright rectangle). An aperture in this top gate close to the constriction defines the position where the underlying 2DEG of the source region is optically excited. (b) and (c): The quantum wire is defined by two adjacent trenches A and B in the 2DEG via a shallow-etch technique [1]. (d): Conductance and photoresponse data of sample A at $T_{BATH} = 2.3$ K, $f_{chop} = 117$ Hz, and $V_{SD} = 1.5$ mV [2].

¹Lehrstuhl für Festkörperphysik Prof. Dr. Jörg. P. Kotthaus, Ludwig-Maximilians-Universität München, Geschwister-Scholl Platz 1, 80539 München.

²Institut für Angewandte und Experimentelle Physik II, Lehrstuhl Prof. Dr. W. Wegscheider, Universität Regensburg, Universitätsstr. 31, 93040 Regensburg.

- [1] K.-D. Hof, C. Rössler, W. Wegscheider, S. Ludwig, A.W. Holleitner, Phys. E 40, Issue 6, 1828 (2008).
- [2] K.-D. Hof, C. Rössler, S. Manus, J.P. Kotthaus, A.W. Holleitner, D. Schuh, W. Wegscheider, Phys. Rev. B 78, 115325 (2008).
- [3] C. Rossler, K.-D. Hof, S. Manus, S. Ludwig, J.P. Kotthaus, J. Simon, A. W. Holleitner, D. Schuh, W. Wegscheider, Appl. Phys. Let. 93, 071107 (2008).
- [4] A.W. Holleitner, V. Sih, R.C. Myers, A.C. Gossard, D.D. Awschalom, Phys. Rev. Let. 97, 036805 (2006).
- [5] A.W. Holleitner, V. Sih, R. Myers, A.C. Gossard, D.D. Awschalom, New J. of Phys. 9, 342 (2007).

Electrical control of spontaneous emission and strong coupling of a single quantum dot

Arne Laucht, Michael Kaniber, Felix Hofbauer, Norman Hauke, Malte Huck, Abbas Mohtashami, Jakob Angele, Andre Neumann, Max Bichler, Gerhard Böhm, Jonathan J. Finley¹

Spontaneous emission is very fundamental and is often regarded as an inherent property of an excited atom, molecule or quantum dot (QD). However, this view overlooks the fact that it is not only a property of the emitter, but also a property of the combined emitter–vacuum system. The irreversibility of spontaneous emission comes about due to the infinite number of vacuum states available to the emitted photon. If the photonic environment is modified, for instance by placing the emitter within an optical cavity, spontaneous emission can be inhibited, enhanced or even made to become reversible. For semiconductor QDs in high finesse cavities, a wide range of novel optoelectronic devices have been realized using such cavity quantum electrodynamics phenomena. Examples include high efficiency single photon sources [1], low threshold, high bandwidth nanocavity lasers and even single-QD optical components such as mirrors and phase shifters.

All such single-QD cavity quantum electrodynamics devices call for a method to precisely control the spectral detuning between the QD and the cavity mode ($\Delta = \hbar(\omega_{\text{QD}} - \omega_{\text{cav}})$) [2]. Until now, this has been done by slowly tuning the lattice temperature or by condensing inert gases at low temperatures. A major drawback of both these methods is that they are slow, rendering them impractical for future single-QD devices. In contrast to that, we demonstrate an electrically contacted single-QD photonic crystal (PC) nanocavity that allows Δ to be rapidly and reversibly switched over ~ 4 meV using the quantum confined Stark effect [3]. In the weak-coupling regime of cavity quantum electrodynamics, we observe a voltage switchable Purcell effect which is depicted in Fig. 1. The upper panel shows a false colour photoluminescence plot of the QD-cavity emission spectra as a function of applied bias voltage. While the QD transitions change in energy due to the quantum confined Stark effect, the position of the cavity mode remains unaffected by the electric field. This allows us to tune a QD exciton in resonance with the cavity mode and conduct measurements of the spontaneous emission lifetime, therefore, probing the Purcell effect. In the lower panel

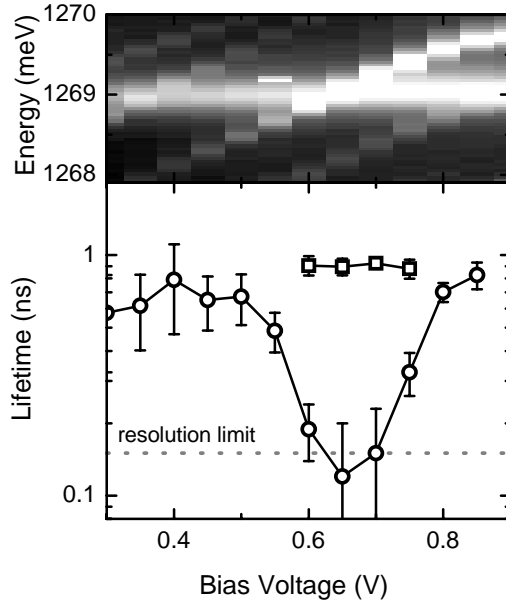


Fig. 1: Electrically controlled weak coupling of QD and cavity mode. The upper panel shows a false colour photoluminescence plot of the emission spectra as a function of the bias voltage. The lower panel shows spontaneous emission lifetime measurements conducted on the spectral position of the QD.

¹phone: +49-89-289-12776, fax: +49-89-320 6620, email: finley@wsi.tum.de

of Fig. 1, we plot the measured lifetime of the QD when it is tuned into resonance with the cavity mode. We observe a clear decrease in the emission lifetime from $\tau_{\text{off resonance}} \approx 0.8 \text{ ns}$ to $\tau_{\text{resonance}} \approx 0.12 \text{ ns}$ when the QD is spectrally well coupled to the cavity mode (open circles). Simultaneously, a second decay time is measured, which we can attribute to the always-present and constant background emission into the cavity mode (open squares) [4]. This measurement shows unambiguously the $\approx 7\times$ enhancement of the spontaneous emission rate by the Purcell effect.

For cavities with $Q > 10\,000$, we observe strong coupling with vacuum Rabi splittings up to $\approx 120\mu\text{eV}$, representing a voltage switchable optical nonlinearity. In Fig. 2(a), we show a series of photoluminescence spectra recorded with high spectral resolution for different bias voltages and observe clear QD-cavity anticrossing. This anticrossing unambiguously demonstrates that the QD-cavity system is in the strong coupling regime and becomes even clearer when we plot the center peak position of both peaks as a function of applied bias as in Fig. 2(b). The solid lines are obtained from theory with parameters fitted to the data. From the fits, we extract a vacuum Rabi splitting of $121\mu\text{eV}$, similar to values reported by other groups. Fig. 2(c) shows the peak intensities of the higher and lower energy peaks normalized to the total emission intensity, plotted for various detunings. These observations unequivocally prove the strong coupling character of this anticrossing in an electrically tunable system. In summary, we have demonstrated single-QD photonic crystal nanocavities operating in the weak and strong coupling regimes of the light-matter interaction, where the electrical tunability offers the unique advantage to quickly and reversibly turn on and off the exciton-photon interaction.

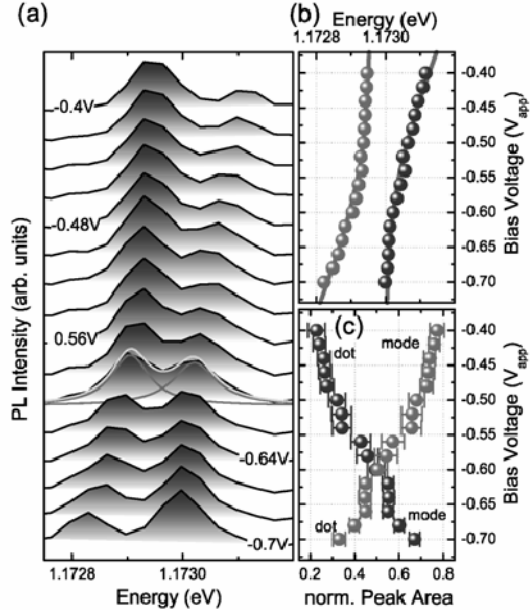


Fig. 2: Demonstration of electrically controlled strong coupling. (a) Waterfall plot of photoluminescence spectra for different bias voltages. (b) Peak center position for the left (bright trace) and the right (dark trace) peak for various detunings. The solid lines show fits to the data. (c) Normalized peak area for the left (bright trace) and the right (dark trace) peak.

- [1] M. Kaniber, A. Laucht, T. Hürliemann, M. Bichler, R. Meyer, M.-C. Amann, and J. J. Finley, *Physical Review B*, **77**, 073312 (2008)
- [2] M. Kaniber, A. Laucht, A. Neumann, M. Bichler, M.-C. Amann and J. J. Finley, *Journal of Physics: Condensed Matter*, **20**, 454209 (2008)
- [3] A. Laucht, F. Hofbauer, N. Hauke, J. Angele, S. Stobbe, M. Kaniber, G. Böhm, P. Lodahl, M.-C. Amann and J. J. Finley, accepted in *New Journal of Physics*, (2009)
- [4] M. Kaniber, A. Laucht, A. Neumann, J. M. Villas-Bôas, M. Bichler, M.-C. Amann, and J. J. Finley, *Physical Review B*, **77**, 161303(R) (2008)

We acknowledge the financial support of the Deutsche Forschungsgemeinschaft via the Sonderforschungsbereich 631, Teilprojekt B3 and the German Excellence Initiative via the Nanosystems Initiative Munich (NIM).

Dielectric screening versus quantum confinement of P-donors in silicon nanocrystals

Andre R. Stegner¹, Rui N. Pereira¹, T. Andlauer¹, K.Klein¹, H. Wiggers², Martin S. Brandt¹ and Martin Stutzmann¹

The recently developed capability of producing macroscopic amounts of freestanding silicon nanocrystals (Si-NCs) has opened up the route for applications such as cost-effective large area electronics using printable Si inks, thermoelectric devices, or solar cells, where properties are tailored via electronic doping at the nanoscale, a process quite distinct from the bulk. Underlying fundamental questions such as dopant confinement, which also influences doping efficiency, are the subject of intense current debate.

So far, experimental data have only been available for Si-NCs with radii smaller than 3.5 nm in a SiO₂ matrix and have been explained only on the basis of quantum confinement imposed by the matrix. However, it has been proposed by theory that dopant localization can also result from a decrease of dielectric screening (dielectric confinement). Using electrically detected magnetic resonance (EDMR), we have investigated networks of densely packed, freestanding Si-NCs with radii between 2.8 nm and 14 nm, produced by microwave-induced decomposition of silane in a low pressure microwave plasma reactor, to monitor the localization of the P donor wave function versus particle size. We have further compared our data with a theoretical model which, unlike previous first principles approaches, can be applied to large NCs and accounts for quantum and dielectric confinement separately in order to assess the contribution of dielectric confinement.

Figure 1 shows EDMR spectra recorded with P-doped Si-NCs with different mean sizes. The strongest feature in each spectrum located at $g=2.006$ originates from different configurations of Si dangling bonds dominantly located at the surface of the Si-NCs. The resonances indicated by the arrows ($hf(^{31}\text{P})$) are attributed to the hyperfine-split EDMR signal of isolated, neutral P donors in Si. For the 14 nm sample, we find a $hf(^{31}\text{P})$ line splitting of about 4.2 mT and a central position at $g=1.998$, which are characteristic for substitutional P in bulk c-Si. In the spectra of smaller NCs, this hyperfine splitting (hfs) increases, whereas the center position of the $hf(^{31}\text{P})$ lines remains constant at $g=1.998$. The observed increase of

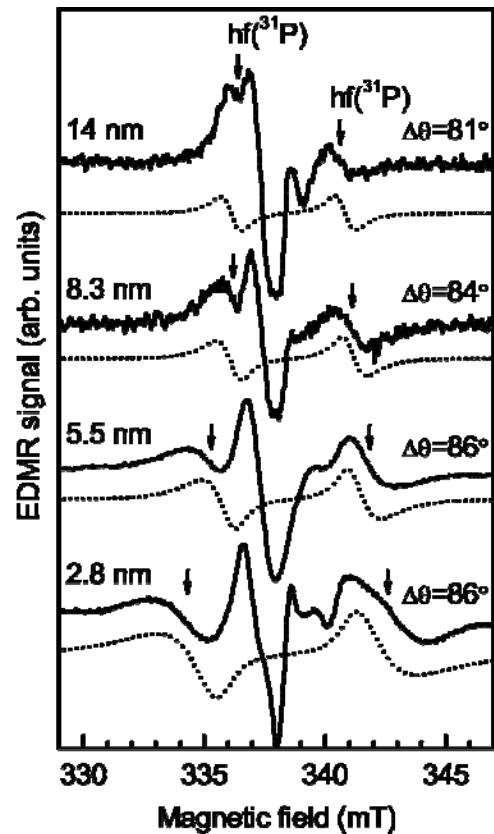


Fig. 1: EDMR spectra of P-doped Si-NCs with 14 to 2.8 nm mean radii (solid traces). Dotted traces depict simulated $hf(^{31}\text{P})$ line shapes.

¹WSI. Corresponding author : ARS, phone: +49-89-289-12783, email: stegner@wsi.tum.de

²Institut für Verbrennung und Gasdynamik, Universität Duisburg-Essen

the hfs is a direct measure for the enhanced wave function localization at small NC radii (R), since the Fermi contact hyperfine interaction between the ^{31}P nuclear spin and the donor electron spin is proportional to the probability density of the donor electron at the ^{31}P nucleus. Figure 1 also shows that the $\text{hf}(^{31}\text{P})$ lines become broader and asymmetric when the NCs size is decreased. To verify that these effects are due to the size distribution of the NCs, we simulated the expected line shapes taking into account the known log-normal size distribution of our particle ensemble and the $R^{-1.5}$ dependence of the hfs proposed by pseudopotential studies. As can be seen in Fig. 1, the simulated resonances (dotted lines) reproduce the experimental observations quite well. In Fig. 2, the hfs size dependence obtained from our measurements (solid circles) is compared with data from an earlier electron spin resonance study of Si-NCs embedded in a-SiO₂ in the radius range of 1.5-3.5 nm (open circles) by M. Fujii et al. The R^{-3} dependence (dashed trace) used to describe these previous results, assuming a pure quantum confinement model, clearly deviates from our data. We use a continuous medium model assuming a single band effective-mass, with the P nucleus represented by a positive charge at the center of a spherical NC that considers both the surface confining potential and a NC size-dependent screening of the Coulomb interaction between the P nucleus and the donor electron. A decrease of the screening of the Coulomb potential of hydrogen-like systems in NCs with respect to the bulk has been predicted in various theoretical works, where it is often described with the use of a size-dependent dielectric constant $\epsilon_{\text{NC}}(R)$, which is parameterized using a generalization of the Penn model to NCs, i.e. $\epsilon_{\text{NC}}(R)=1+(\epsilon_{\text{bulk}}-1)/[1+(\alpha/R)^l]$. We use the parameters $\alpha=0.97$ nm and $l=1.3$. As can be seen in Fig. 3, the results of our model (solid trace) describe very well both our experimental data and the previously reported data. To understand the relative contributions of quantum confinement and dielectric screening, we considered two additional variations of the model: (i) pure quantum confinement, where the dielectric screening size-dependence is neglected by substituting $\epsilon_{\text{NC}}(R)$ with ϵ_{bulk} (dotted trace), and (ii) pure dielectric confinement, where the confining surface potential is neglected (dash-dotted trace). The quantum confinement model is sufficient to describe the experimentally observed hfs for Si-NCs with radii below 3 nm, while the pure dielectric confinement model gives a good description of the data for Si-NCs with radii larger than 6 nm. For intermediate NC sizes, both dielectric and quantum confinement have a sizeable contribution to donor electron wave function localization.

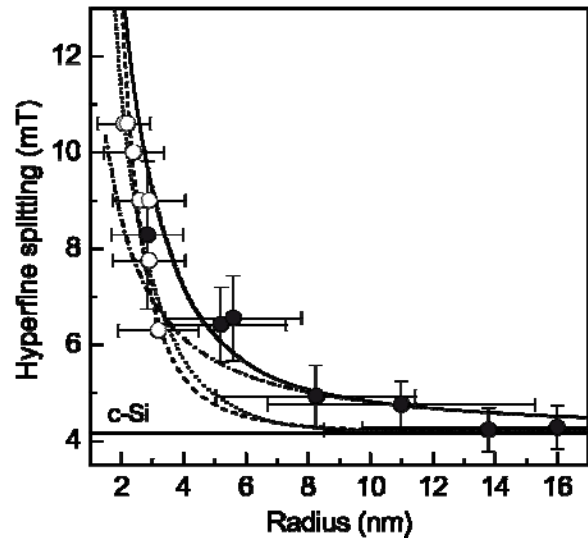


Fig. 2: Dependence of the ^{31}P hyperfine splitting on the mean radius of Si-NCs. Details are described in the text.

Reference: R. N. Pereira, A. R. Stegner, T. Andlauer, K. Klein, H. Wiggers, M. S. Brandt, and M. Stutzmann, Phys. Rev. **B 79**, 161304(R) (2009)

Asymmetry between absorption and photoluminescence line shapes of TPD: Spectroscopic fingerprint of the twisted biphenyl core

Reinhard Scholz¹, Linus Gisslén

For TPD, absorption, photoluminescence, and resonant Raman spectra are interpreted with model calculations based on density functional theory (DFT) and time-dependent DFT. The peculiarities of the potential energy surfaces related to a twisting around the central bond in the biphenyl core of TPD allow a quantitative interpretation of the asymmetry between the line shapes observed in absorption and emission.

During the last decade, N,N'-diphenyl-N,N'-bis(3-methylphenyl)-(1,1'-biphenyl)-4,4'-diamine (TPD, see Fig. 1) was mainly attracting attention due to its transport properties, so that it became a prototypical hole-conducting compound used in light emitting diodes. Recent applications of TPD in UV detectors have revealed that the photo-response is determined by the absorption coefficient of the material, even in blends with Alq₃. Moreover, due to the very large Stokes shift of about 0.5 eV, TPD is transparent to its photoluminescence (PL),

so that it has a promising potential for laser applications, showing stimulated emission even in the form of neat films. This finding is quite surprising, as most molecules with this property need to be diluted in a host matrix or in a solvent in order to show laser activity.

Absorption and PL line shapes of molecules are directly related to the elongations of internal vibrations in their relaxed excited geometry. These elongations can be quantified with resonant Raman spectroscopy, and different variants of density functional theory (DFT) can be used for a calculation of the deformation in the relaxed excited state [1]. A projection of the vibrational eigenvectors onto this deformation pattern reveals the Huang-Rhys factor of each vibration, defining in turn its Raman activity and the vibronic progressions observed in absorption and photoluminescence.

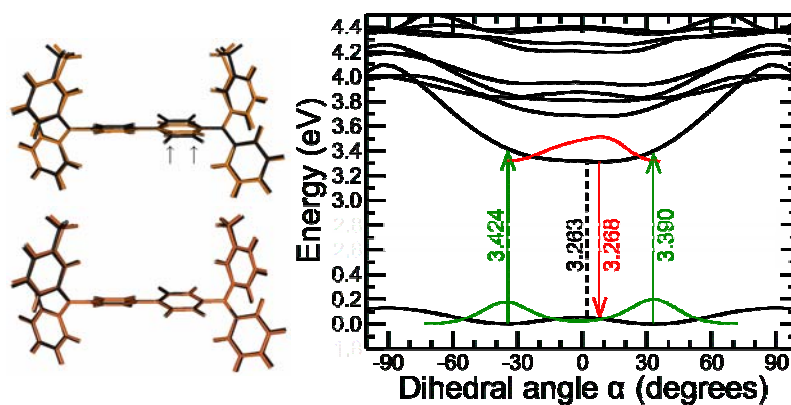


Fig. 1: Left: Geometry of TPD in its electronic ground state (black), and in the lowest excited state (orange). Upper: excited geometry as calculated with time-dependent DFT, lower: after elimination of changes of the dihedral angles. Right: Potential energy surfaces along the central dihedral angle, from DFT and time-dependent DFT, and Boltzmann distributions in electronic ground state (green) and lowest excited state (red). Transition energies revealing the large Stokes shift are highlighted.

¹phone: +49-89-289-12752, fax: +49-89-12737, email: reinhard.scholz@wsi.tum.de

Fig. 1 shows the excited state deformation obtained with time-dependent DFT. The deformation of the various phenyl rings results in the elongation of high frequency internal modes, and the peculiarities of the potential energy surfaces along the central dihedral angle reveal a substantial Stokes shift. The elongation of high-frequency internal modes can be summarized in terms of an effective vibration at 158 meV with an effective Huang-Rhys factor of 0.87. The Boltzmann distribution in the ground and excited potential energy surfaces (PES) can be transformed into a distribution over transition energies, defining in turn the line shape of each subband of the

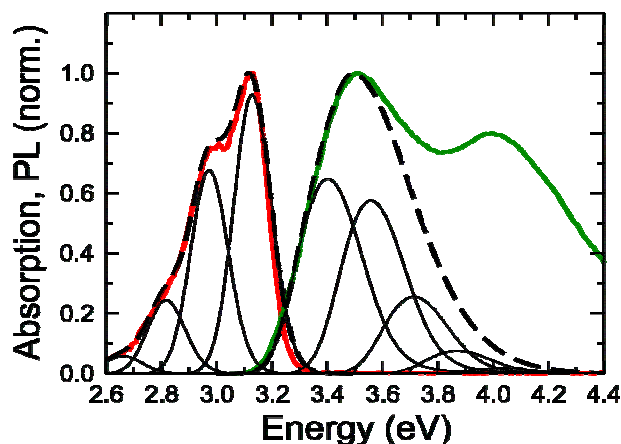


Fig. 2: Measured absorption (green) and emission (red), and calculated line shapes (dashed). The calculation includes an effective high-frequency internal vibration at 158 meV with a Huang-Rhys factor of 0.87 calculated with DFT, and subband shapes obtained from Boltzmann distributions over the central dihedral angle according to Fig. 1.

internal effective mode. The shape of the two PES along the central dihedral angle in the biphenyl core results directly in a large asymmetry between the densities of states and broadenings involved in absorption and PL. This is also reflected in different contributions to the respective reorganization energies. Further low-frequency modes involving torsional motion around other bonds connecting the various phenyl rings contribute to the large Stokes shift and to the broadening of the vibronic subbands of the effective mode.

In conclusion, the complementary information contained in absorption, photoluminescence, and resonant Raman spectroscopy can be rationalized by a comprehensive analysis of the photophysics with time-dependent DFT calculations. It was found that the twisted shape of the central biphenyl group allows a quantitative understanding of the different linewidths observed in absorption and PL together with an asymmetry between the reorganization energies on the two potential energy surfaces involved. The torsional modes at low frequencies contribute substantially to the different broadenings of absorption and PL spectra. As a result, the vibronic subbands of high-frequency internal modes remain visible in PL, but in absorption, they are washed out by the larger broadening arising from the flat ground state potential along the twisting around the central bond. Our detailed model calculations have demonstrated that the photophysics of TPD can be understood from the properties of the molecule itself. The influence of intermolecular interactions is restricted to a small dependence of the Stokes shift on the solvent or matrix material, but the contribution of the surroundings to the broadening remains much smaller than the influence of the torsional modes of TPD at very low frequency.

- [1] R. Scholz, L. Gisslén, C. Himcinschi, I. Vragović, E. M. Calzado, E. Louis, E. S. Maroto, and M. A. Díaz-García, *J. Phys. Chem. A* **113**, 315 (2009).

Electrically controllable g factors in quantum dot molecules

Till Andlauer¹ and Peter Vogl

Spins of confined carriers in quantum dots are promising candidates for the logical units in quantum computers. In many concepts developed so far, the individual spin-qubits are being manipulated by magnetic fields, which is difficult to achieve in practice. An alternative procedure is to address individual spin-qubits by their own electric gate which allows fast changes of the spin splitting and quantum gate operations. In any case, progress in this field requires a detailed understanding of the mechanisms that allow one to modify spin-related electronic structure properties such as gyromagnetic factors.

We have performed a quantitative theoretical analysis of electron, hole, and exciton g factors of vertically coupled InAs/GaAs quantum dot pairs in external electric and magnetic fields [1]. To this end, we calculate the energies of electron and hole ground and first-excited states of a mesoscopic system using a relativistic eight-band $\mathbf{k}\cdot\mathbf{p}$ envelope function method including strain that accounts for magnetic fields in a gauge-invariant manner. The quantum dot molecules are characterized by the dot separation d , the quantum dot height h , the dot width w , and the alloy profile within the individual dots (see inset in Fig. 1). We model the dots as truncated pyramids that sit on 0.5 nm InAs wetting layers on a [001]-

GaAs substrate. From the Zeeman splitting of the molecular electron (e) and hole (h) states in a magnetic field, we have calculated the g factors associated with the ground (0) and first-excited states (1). In terms of these g factors $g_e(0)$ and $g_h(0/1)$, the lowest neutral exciton g factors are given by $g_x(0/1)=g_e(0)+g_h(0/1)$. In Fig. 1, we have calculated these exciton g factors for the magnetic field lying in the vertical [001]-direction, as a function of a vertically applied electric field. The exciton g factors can be tuned by more than 100% by the electric field and show a pronounced resonance behavior that can be understood qualitatively as follows. The electric field tunes the energies of the individual dot hole states relative to each other. For a particular field F_{res} , the two ground

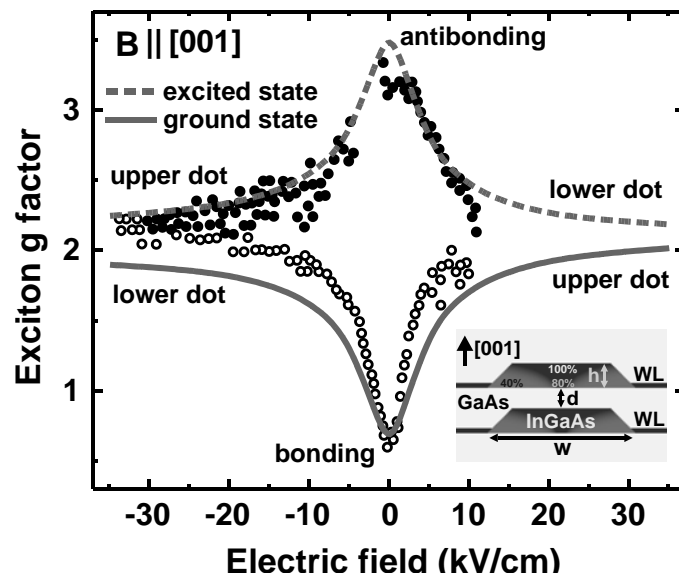


Fig. 1: Exciton g factors of coupled quantum dots, for magnetic and electric fields lying in the vertical [001] direction. The dots are characterized by $h=2.5\text{nm}$, $w=15\text{nm}$, and $d=1.5\text{nm}$. All electric field values are specified relative to the resonance field $F_{res}=7\text{kV/cm}$. The full and dashed lines indicate calculated results for the ground state and the first excited state, respectively. For comparison, we also show experimental results from Ref. [2] (circles).

¹phone: +49-89-289-124486, fax: +49-89-289 12737, email: andlauer@wsi.tum.de

states are tuned into resonance and form molecular bonding and antibonding orbitals. Our calculations show that the hole g factors of the isolated quantum dots are positive, while the hole g factor of bulk GaAs is negative. Now, for the present coupled quantum dots, the formation of bonding (antibonding) states as a function of the electric field increases (decreases) the overlap of the molecular states with the GaAs barrier region in between the coupled quantum dots which leads to a decrease (increase) in the molecular hole g factor. The trends in the exciton g factors entirely reflect the trends of the hole g factors, whereas the electron g factor only shifts the absolute values slightly since it remains almost constant. This comes from the fact that the lowest molecular electron state forms an extended bonding state for all electric fields considered. To illustrate the resonant behavior of the exciton g factor, in Fig. 1, we have indicated the localization of the hole states in the coupled dots for the different electric field regimes. As can also be seen from the figure, our calculations are in excellent agreement with the experimental results from Ref. [2].

We have also calculated g factors for magnetic field directions other than the growth axis. In Fig. 2, we show the calculated molecular hole g factors for magnetic fields oriented along the planar directions $[110]$ and $[1-10]$. Since the electron g factors remain constant over the shown electric field range, the figure applies to exciton g factors as well. Analogous to the situation for vertically applied magnetic fields, we obtain a resonant reduction and enhancement of the g factors for the bonding and antibonding states, respectively. In addition, the results indicate a highly efficient bias induced switching of the molecular g factor between a value close to zero and a finite negative value for the extremal electric field values. This switching behavior is a robust effect and neither sensitive to small changes in the bias, as can be deduced from Fig. 2, nor to small changes in the quantum dot widths. Importantly, the calculations predict a pronounced anisotropy of the ground and excited-state hole g factors. By orienting the magnetic field along the $[1-10]$ instead of the $[110]$ direction, the results indicate that the role of the upper and lower dot in the molecular states are effectively swapped. The present effect is caused by the piezoelectric charge distribution near the edges of the quantum dots that deform the hole charge distribution differently in the two coupled quantum dots that form the molecule [1].

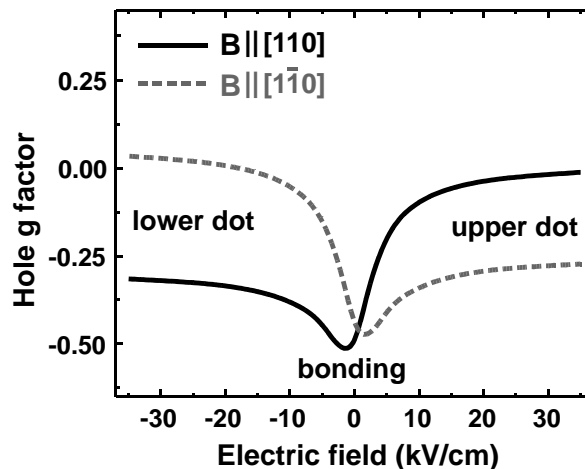


Fig. 2: Calculated molecular g factors of hole ground state as a function of vertically applied electric field relative to the resonance field F_{res} . The constant lateral magnetic field lies along the $[110]$ (full line) and $[1-10]$ direction (dashed line), respectively.

- [1] T. Andlauer and P. Vogl, Phys. Rev. B **79**, 045307 (2009)
 [2] M. F. Doty, M. Scheibner, I. V. Ponomarev, E. A. Stinaff, A. S. Bracker, V. L. Korenev, T. L. Reinecke and D. Gammon, Phys. Rev. Lett. **97**, 197202 (2006)

Materials Science

Growth mechanisms of Molecular Beam Epitaxy GaAs nanowires.

Carlo Colombo², Danče Spirkoska, Gerhard Abstreiter, and Anna Fontcuberta i Morral^{1,2}

Semiconductor nanowires are of interest for use as building blocks of future nanoscale devices and circuits. Equally important, nanoscale objects often exhibit new properties that can be exploited into new device concepts such as thermoelectric applications and/or solar cells. One issue of crucial importance has been the control on the crystalline quality and impurity concentrations, as well as the reproducibility of the structures. With regards to the purity, one of the key issues has been to avoid the use of gold as nucleation and growth seed of the nanowires. Gold is a fast-diffusing metal that significantly harms the properties of semiconductors. One way to avoid the use of gold for the synthesis of nanowires is directly to grow without the need of an external catalyst. This method is called “catalyst-free” growth.

We have achieved catalyst-free growth of GaAs nanowires by growing GaAs under gallium rich conditions. In this way, gallium droplets form and gather the arsenic As_4 molecules. The arsenic species diffuse through the droplets to finally precipitate gallium arsenide underneath, forming a nanowire. This type of growth has been linked to the existence of a full or patterned SiO_2 surface. We have presented a detailed study on the nucleation stage of the nanowires and on the role of the SiO_2 . We have found that the use of an oxide is necessary for the nucleation. We attribute this to the wetting properties of gallium on SiO_2 , which allows the formation of small droplets. For oxide thicknesses below 30 nm, the nanowires grow oriented with respect to the crystalline orientation of the substrate underneath. This can be clearly observed in Fig.1, where scanning electron micrographs of nanowires grown on (001) and (111)B oriented substrates is shown.

The growth mechanisms of the nanowires were investigated by varying the growth conditions. In order to validate the role of the gallium droplet in the gathering of the arsenic species, a series of synthesis runs was realized by varying the total arsenic beam flux. The morphology of the nanowires and growth rate was monitored. It was found that the axial growth rate of the nanowires is proportional to the total arsenic beam flux. This result is shown in Fig.2. We have also developed a model to explain the growth. The first thing to consider is that the sticking coefficient of Ga adatoms on SiO_2 at the growth temperatures is close to zero, due to a combination of an increase in the desorption rate and the diffusion length.

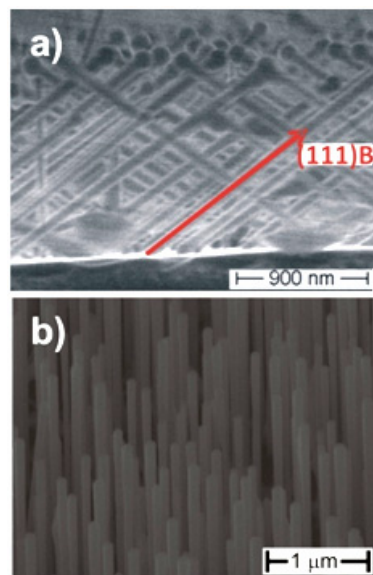


Fig. 1: Scanning electron micrograph of GaAs nanowires grown on 001 substrates (a) and (111)B substrates (b).

¹phone: +49-89-289-12779, fax: +49-89-320 6620, email: annafm@wsi.tum.de

²auch an Ecole Polytechnique Federale de Lausanne, Schweiz

The consequence of this is that Ga adatoms are mobile on the SiO₂ surfaces and can diffuse towards GaAs regions, where they can be incorporated. In this way, the atoms impinging on the substrate are supposed to diffuse through the oxide and then along the nanowire side-walls, and to the tip of the nanowire contributing to the Ga droplet. During their path along the nanowire facets, they can also be incorporated or desorb. In stationary conditions the diffusion of Ga adatoms along the facets towards the tip of the nanowire is described with the following equation:

$$D_f \frac{\partial^2 \eta}{\partial z^2} - \frac{\eta + 1}{\tau_f} - \frac{1}{\tau_a} = 0$$

where D_f is the diffusion coefficient, η is the supersaturation of Ga atoms, and τ_f and τ_a are the characteristic time for desorption and for incorporation, respectively. As the incorporation time (20 s) is several orders of magnitude larger than the desorption time (10^{-4} s), the last term of the eq. 3 can be neglected and the process is assumed to take place with a constant diameter. The boundary conditions are: (i) constant flux at the bottom of the nanowire and (ii) constant supersaturation at the top. We calculated the flux of Ga atoms along the nanowire. As the diffusion coefficient D_f of Ga atoms on GaAs (110) surface is about $1,6 \cdot 10^5 \text{ \AA}^2/\text{s}$ at growth temperature around 600°C ; the equilibrium concentration n_{eq} is equal to $2,27 \cdot 10^{-4} \text{ atoms/\AA}^2$ and a typical value for the nanowire radius R is 30nm. This flux provides Ga atoms to the catalytic droplet in order to keep it liquid and it is not the growth limiting factor, otherwise a decreasing in the growth rate should be observed for longer nanowires due to the reduction in the incoming flux. The flux of Ga atoms at the top of the nanowire decreases as the nanowire grows. In order to maintain the same axial growth rate, the Ga diffusing flux at the top of the nanowire $J(L)$ has to be equal or higher than the incorporation rate Γ of Ga atoms from the liquid droplet into the nanowire. The condition for which the arrival of gallium atoms at the droplet is exactly enough to fulfill the nanowire growth is reached for nanowire about $40\mu\text{m}$ long. For longer nanowires, the flux $J(L)$ is not able to keep the size of the droplet. Then, the droplet should diminish in size, resulting in a tapering of the nanowire. After the droplet is completely consumed, the axial growth rate should stop.

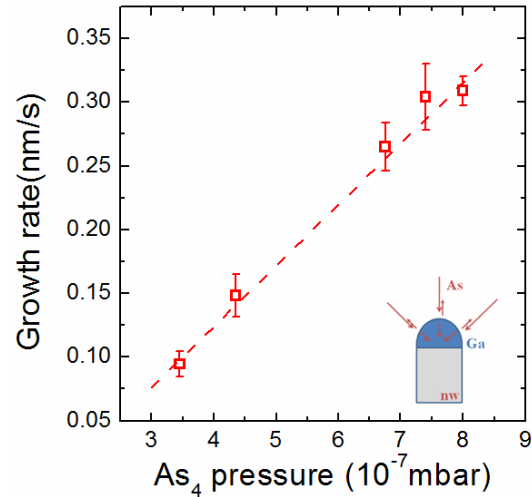


Fig. 2: Growth rate of the GaAs nanowires as a function of the arsenic beam flux.

- [1] C. Colombo, D. Spirkoska, M. Frimmer, G. Abstreiter, A. Fontcuberta i Morral, Phys. Rev. B, 77, 155326 (2008), featured in Virtual Journal of Nanotechnology
- [2] A. Fontcuberta i Morral, C. Colombo, J. Arbiol, J.R. Morante, G. Abstreiter, Appl. Phys. Lett. 92 063112 (2008)

Prismatic heterostructures on GaAs nanowire facets.

Danče Spirkoska, Matthias Heigoldt, Gerhard Abstreiter, and Anna Fontcuberta i Morral^{1,2}

Molecular Beam Epitaxy (MBE) is nowadays a standard tool to fabricate semiconductor heterostructures of very high quality. In this sense, epitaxial growth on the facets of the nanowires can be viewed as a nanometer scale version of the classical MBE growth. At the same time, it is a natural extension to the MBE growth of nanowires. In the following we present the fabrication principle, as well as the results on the structural characterization of the structures grown on the facets of the nanowires.

Once the nanowire GaAs cores were grown (simple GaAs NWs), the conditions were changed towards planar MBE growth. The arsenic pressure was increased from 8×10^{-6} mbar to 5×10^{-5} mbar and the temperature decreased down to 550°C . This resulted in defect-free growth on the $\{110\}$ facets. Due to the directionality of the molecular beams, the deposition occurs only on the exposed surfaces. In the cases where the wires are perpendicular to the surface and the substrate is rotated during growth, the layers grown on the facets should have equal thickness. One example of nanowires that have been overgrown on their facets is shown in Fig. 1. As it can be observed specially in Fig. 1b, the Ga droplet has crystallized due to the large As_4 pressure applied. The diameter of the nanowire is constant along the whole length, indicating that the growth on the facets has been produced in a homogeneous way.

In order to get more insight into the growth process on the facets, cross sectional high-resolution transmission electron microscopy (HRTEM) and high angular annular dark field (HAADF) analysis as well as 3D HAADF Electron Tomography reconstructions were carried out on the grown structures on the nanowires. All these techniques were used in order to precisely measure the thickness of the different prismatic shells grown on the NW core $\{110\}$ facets. For the structural HRTEM and HAADF investigations, the samples were prepared in the following way: First, they were transferred on a silicon substrate in a way that the nanowires were lying parallel. Then, they were coated with a 100 nm thick SiO_2 layer. After that, cross-sections of these structures were fabricated following standard TEM preparation methods.

In order to systematically correlate the nominal planar thickness with the obtained thickness of each of the layers, AlAs and GaAs layers with nominal thickness between 1.7 and 24 nm were deposited. A typical cross-sectional TEM measurement of a multi quantum wells grown on nanowires obtained on a (111)B GaAs substrate is shown in Figure 2b.

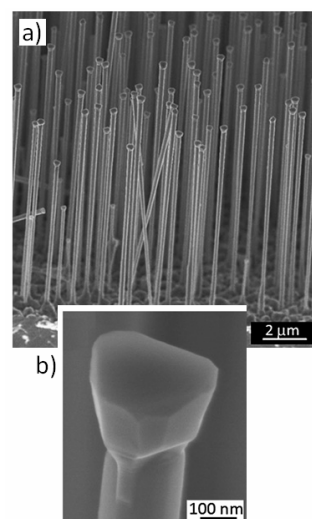


Fig. 1: Scanning electron micrograph of GaAs nanowires grown on 001 substrates (a) and (111)B substrates (b).

¹phone: +49-89-289-12779, fax: +49-89-320 6620, email: annafm@wsi.tum.de

²auch an Ecole Polytechnique Federale de Lausanne, Schweiz

As the wire is oriented parallel to the surface normal and the sample holder inside the MBE chamber is rotated, the total amount of deposited material was equal for the six sidewalls of the wire. Also the epitaxial growth on the

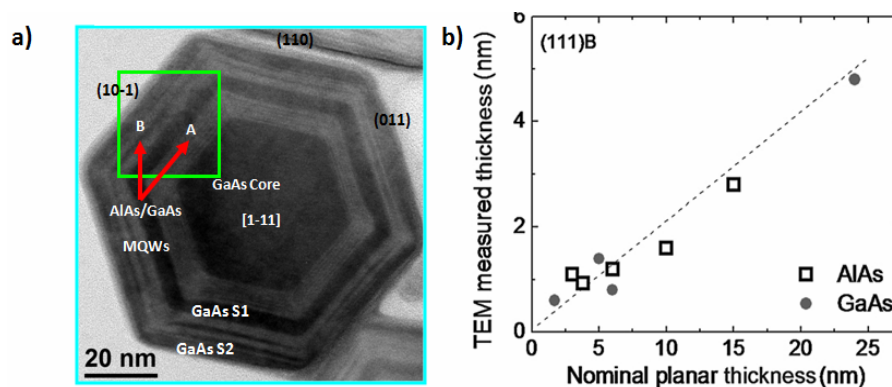


Fig. 2: a) Transmission Electron Micrograph of a cross section of a nanowire with a series of AlAs/GaAs layers. b) Correspondence between the nominal thickness and the thickness of the layers grown on the facet as measured by TEM.

side facets was verified, which enabled the NW to conserve its hexagonal shape. The thicknesses of the different AlAs and GaAs layers were measured and compared to the different amounts of material grown. The correlation between the nominal and measured thickness of each of the layers is shown in Fig. 2b. As expected, the AlAs and GaAs layers fall into the same relation. According to what it is expected due to the geometry, one fifth of the nominal layer is deposited on each of the facets, independently of the total amount.

The optical properties of the quantum wells grown on the facets were also investigated by spatial resolved confocal photoluminescence spectroscopy. More information can be found in the references here below.

- [1] M. Heigoldt, J. Arbiol, D. Spirkoska, J.M. Rebled, S. Conesa-Boj, G. Abstreiter, F. Peiro, J.R. Morante, A. Fontcuberta i Morral, J. Mater. Chem. 19, 840 (2009)
- [2] Anna Fontcuberta i Morral, Dance Spirkoska, Jordi Arbiol, Matthias Heigoldt, Joan Ramon Morante and Gerhard Abstreiter, Small 4, 899-903 (2008); highlighted in Nature Materials, 7, 608 (2008)

Growth and Characterization of ZnO/Zn_{1-x}Mg_xO Quantum Wells

Bernhard Laumer¹, Thomas A. Wassner, Jochen Bruckbauer, Martin Stutzmann, and Martin Eickhoff

Zinc oxide (ZnO) is a potential candidate for the fabrication of blue and ultraviolet optoelectronic devices, as it exhibits a direct band gap of 3.4 eV and, most remarkably, an exciton binding energy of 60 meV. The high exciton binding energy well above thermal energies at room temperature facilitates effective radiative recombination of electrons and holes. By alloying ZnO with Mg, the band gap can be increased up to 4.2 eV. This allows the fabrication of ZnO/Zn_{1-x}Mg_xO quantum well structures, in which the excitons can be locally confined, thus further enhancing the efficiency of the radiative recombination process.

ZnO/Zn_{1-x}Mg_xO quantum wells (QWs) were grown on c-plane sapphire substrates by plasma assisted molecular beam epitaxy (PAMBE), employing a MgO/ZnO double buffer layer similar to [1]. For the growth of heterostructures, a 2-dimensional growth mode is essential in order to accomplish abrupt interfaces. To achieve this, first the ZnO growth on the buffer was optimized by investigating the influence of the II/VI-flux-ratio on the morphology of the resulting ZnO thin films at a fixed substrate temperature of 500°C. For Zn-rich growth conditions the surface exhibits pits, whereas under O-rich conditions terrace-like structures are observed, which is in agreement with the results of other groups [2]. The smoothest surfaces are obtained for stoichiometric growth conditions with a root mean square (rms) roughness of less than 0.5 nm.

Single ZnO/Zn_{1-x}Mg_xO QWs were grown on an approximately 250 nm thick and atomically flat intermediate ZnO layer on top of the annealed MgO/ZnO double buffer. First, a 25 nm thick Zn_{1-x}Mg_xO barrier was deposited, followed by the ZnO well whose thickness varied from 2.5 to 4 nm for different samples and a 25 nm thick Zn_{1-x}Mg_xO capping layer. The substrate temperature was set to 500 °C for all growth steps following the buffer

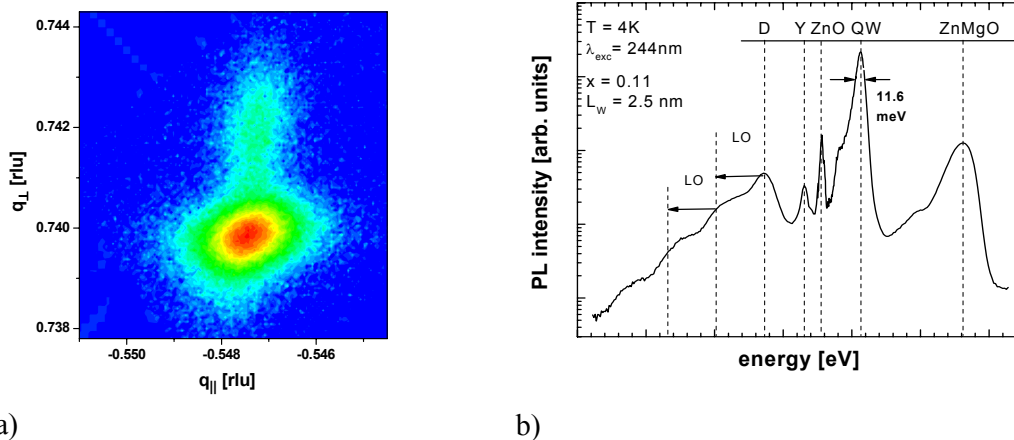


Fig. 1: a) Reciprocal spacemap of the 205 reflex: the tail extending parallel to q_{\perp} originates from the pseudomorphically grown Zn_{1-x}Mg_xO barriers. b) Low-temperature PL spectrum of a ZnO/Zn_{1-x}Mg_xO QW

¹ phone: +49-89-289-12783, email: bernhard.laumer@wsi.tum.de

growth and no additional annealing steps were carried out. In this manner, a Mg-content up to $x = 0.2$ was obtained, corresponding to a barrier height of 350 meV. By trying to further increase the Mg-content, a transition from 2-dimensional to 3-dimensional growth occurred, evidenced in-situ by reflection high energy electron diffraction (RHEED) and ex-situ by atomic force microscopy (AFM). High resolution X-ray diffraction (HRXRD) measurements on these samples revealed the appearance of a rock salt $\text{Mg}_{1-x}\text{Zn}_x\text{O}$ phase.

For QWs with $x \leq 0.2$, reciprocal spacemaps of the 205 X-ray reflex showed that the $\text{Zn}_{1-x}\text{Mg}_x\text{O}$ barrier layers grow pseudomorphically on ZnO (Fig. 1a). The photoluminescence spectra of these QWs (Fig. 1b) are dominated by an emission line that is blue-shifted with respect to the emission of bulk ZnO. The blue-shift as well as the integrated PL intensity of the dominant emission line increases with increasing barrier heights and decreasing well width and is, therefore, attributed to the recombination of excitons confined in the QW. Furthermore, an emission line (D) below that of ZnO with pronounced phonon replicas appears, which red-shifts with increasing x . For all samples an emission line at 3.333 eV is observed (Y) which has been assigned to extended structural defects in ZnO [3].

Temperature-dependent PL measurements (Fig. 2) reveal that the intensity of the Y-line decreases rapidly with increasing temperature, supporting this assignment. The excitonic emission of the QWs is found to actually consist of two emission lines. The low energy peak (LX) which is dominant at low temperatures is attributed to localized excitons. For temperatures above 150 K, the peak labeled with FX becomes the dominant contribution and is therefore assigned to the recombination of free excitons in the QW. The emission energy of the ZnMgO barrier exhibits a S-shape typical for alloys with compositional disorder.

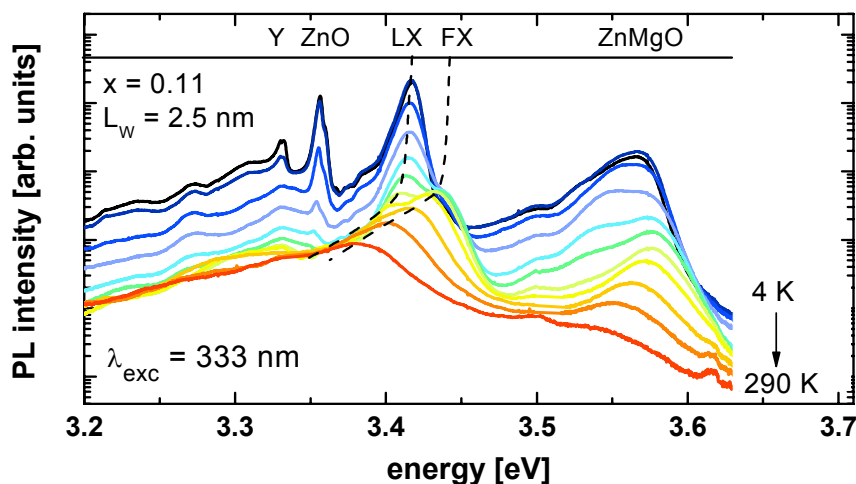


Fig. 2: Temperature dependence of the photoluminescence of a $\text{ZnO}/\text{Zn}_{0.89}\text{Mg}_{0.11}\text{O}$ QW.

- [1] A. Bakinet al., Journal of Crystal Growth 287, 7 (2006)
- [2] Y. Chen et al., Appl. Phys. Lett. **80**, 1358 (2002)
- [3] B. K. Meyer et al., phys. stat. sol. (b) 241, 231–260 (2004)

AlN growth on (100) and (111) diamond by plasma-assisted molecular beam epitaxy

Olaf Weidemann¹, Martin Stutzmann, and Martin Eickhoff²

AlN and diamond both feature the advantages of wide band gap materials for high power and optoelectronic devices. In addition, diamond has a superior thermal conductivity which can handle high power densities, which are present in modern devices. However, the lack of efficient p-type doping of AlN and n-type doping of diamond so far does not allow the fabrication of efficient bipolar devices from either material. This drawback can be overcome by combining n-AlN and p-diamond in a heterostructure device, which in turn requires an in depth understanding of the structural and electrical properties of the diamond/AlN interface. To this end, a systematic structural analysis was carried out on AlN layers grown by plasma assisted molecular beam epitaxy (PAMBE) on single crystalline Ib diamond substrates with (100) and (111) orientations supplied by Element Six Ltd..

The AlN layers were grown under Al-rich conditions on both substrates with layer thicknesses ranging from 2 - 600 nm. For both orientations, the AlN layers show columnar growth with hexagonal domains, leading to an rms roughness of typically 5 nm for the 600 nm thick layers. The initial nucleation (first 1-3 nm) forms more homogeneous islands with a higher density on the (111) oriented diamond substrates. During growth, the initially isolated islands partly coalesce, forming domains with lateral sizes up to 1 μm for the thick layers. Convergent beam electron diffraction (CBED) measurements reveal that these layers exhibit single polarity - presumably with Al-face orientation.

The two different crystal orientations of the diamond substrates exhibit a four-fold symmetry for the (100) and a three-fold symmetry for the (111) surface. Compared with the hexagonal wurtzite lattice of AlN, this leads to the possible formation of two different AlN domain types on the (100) surface, which are rotated by 30° with respect to each other, as derived from high resolution X-ray diffraction (HRXRD) measurements (Fig. 1). The integrated intensities for the two domain orientations are similar as the formation energies of the respective phases are the same.

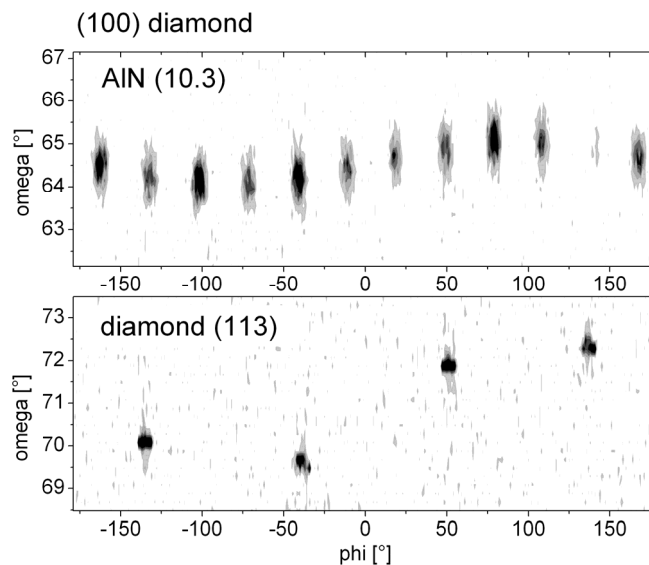


Fig. 1: HRXRD pole figures of the AlN (10.3) and the diamond (113) reflex, showing the four-fold symmetry of the diamond (100) surface and the 12 peaks of the double domain structure of the hexagonal AlN.

¹ phone: +49-89-289-12889, fax: +49-89-289-12737, email: weidemann@wsi.tum.de

² current address: I. Physikalisches Institut, Justus-Liebig-Universität Giessen, e-mail: eickhoff@exp1.physik.uni-giessen.de

In contrast, the evolution of two domain orientations with the same formation energy is not possible on (111) diamond surfaces. Consequently, also only a single domain type is observed on diamond (111) surfaces.

Reciprocal space map analysis of the AlN layers allows extraction of the a- and c-lattice parameters and, thus, the evaluation of the strain state of the epitaxial AlN layer. While the layers on (100)-oriented diamond are fully relaxed, the AlN films on (111) diamond are under a tensile strain of 6%, as indicated in the reciprocal spacemap analysis displayed in Fig. 2.

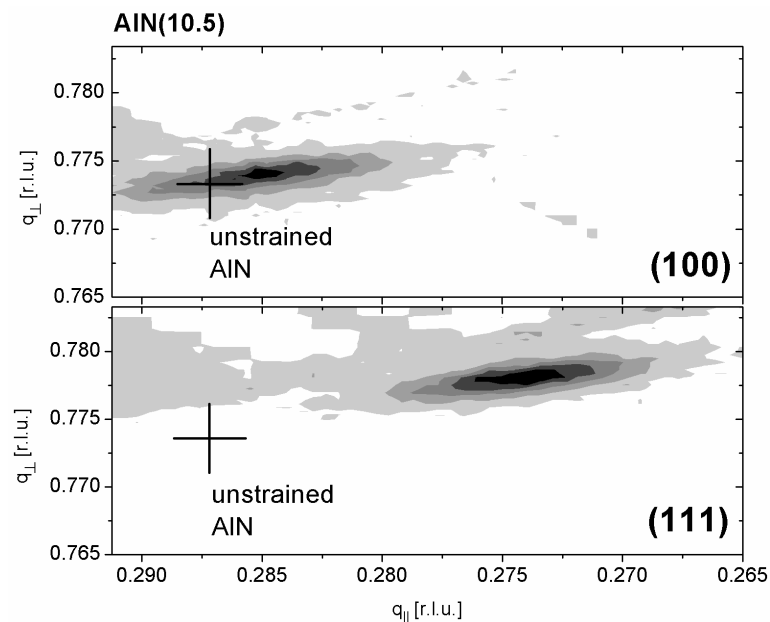


Fig. 2: HRXRD reciprocal space map of the AlN (10.5) reflex: on (100) oriented diamond the AlN layer is almost completely relaxed, while on (111) diamond it is under strong tensile strain.

One way to overcome the formation of multiple domains on (100) substrates might be the use of miscut samples. That reduction of the surface symmetry can suppress the growth of multiple domain orientations was already shown for AlN on (001)-Si [1]. By comparison of AlN layers grown on diamond substrates with different miscut angles however, we have not found any suppression of the double domain structure up to miscut angles of 2.7° for (100) diamond surfaces. Furthermore, the c-axis of the AlN film is not oriented perpendicular to the (100) lattice planes of those substrates, but rather grows perpendicular to the misoriented substrate surface. In contrast, on (111) samples the AlN c-axis is oriented perpendicular to the crystallographic (111) plane. The rigid epitaxial relation between the AlN film and the (111) diamond surface is further evidenced by the higher density of dislocations at the diamond/AlN interface due to the accumulation of tensile strain. The relaxed growth mode on the (100) surfaces, on the contrary, is reflected by a lower dislocation density.

- [1] V. Lebedev, J. Jinschek, J. Kräußlich, U. Kaiser, B. Schröter and W. Richter, *Journal of Crystal Growth*, **230**, 426 - 431 (2001)

GaN/AlN and GaN/AlGa_xN nanowire heterostructures grown by PAMBE

Florian Furtmayr¹, Christoph Stark, Jordi Arbiol², Sònia Conesa-Boj², Francesca Peiró², Joan Ramon Morante², Martin Stutzmann, and Martin Eickhoff^{1,3}

We report on the optical and morphological properties of AlN/GaN and AlGa_xN/GaN nanowire (NW) heterostructures with embedded GaN nanodisks (NDs) grown by plasma-assisted molecular beam epitaxy (PAMBE). GaN NWs are strain free single crystals that can be grown on different substrates, such as Si(111), Si(100), or sapphire, avoiding the formation of structural defects due to the lattice mismatch, as they are present heteroepitaxial thin films. Here, low resistivity n-type Si(111) substrates were exposed to a nitrogen plasma at the growth temperature of 780°C for 15 min directly before GaN growth. The growth parameters were selected to form self-assembled nanowires that grow perpendicular to the substrate surface along the wurtzite c-axis. Details on the growth can be found in Ref. [1].

For the formation of nanodisks, as a first step GaN nanowires with a length of 400 nm were grown, directly followed by a quantum well structure. In the investigated samples, a 9-fold multi quantum well was formed by barriers of 7 nm AlN or Al_xGa_{1-x}N with different Al-compositions and wells of pure GaN with different thicknesses (1.5 nm – 4 nm). The resulting optical properties were studied by photoluminescence spectroscopy (PL). Low temperature PL spectra of different Al_xGa_{1-x}N / GaN ND samples with varied Al-content are shown in Fig. 1.

The emission band at 3.4 eV - 3.5 eV originates from the GaN base region of the NWs. For the sample with the lowest Al-content one can resolve individual peaks at 3.41 eV, 3.45 eV, and the strongest contribution at 3.47 eV which originates of the recombination of free and donor-bound excitons [2]. The emission energy from the NDs depends on the Al-content in the barrier and increases from 3.53 eV to 3.73 eV by varying the BEP_{Al} from 1.5×10^{-8} mbar to 8.5×10^{-8} mbar. Its intensity clearly exceeds the GaN base emission, and the full width at half maximum (FWHM) is found as low as 21 meV for

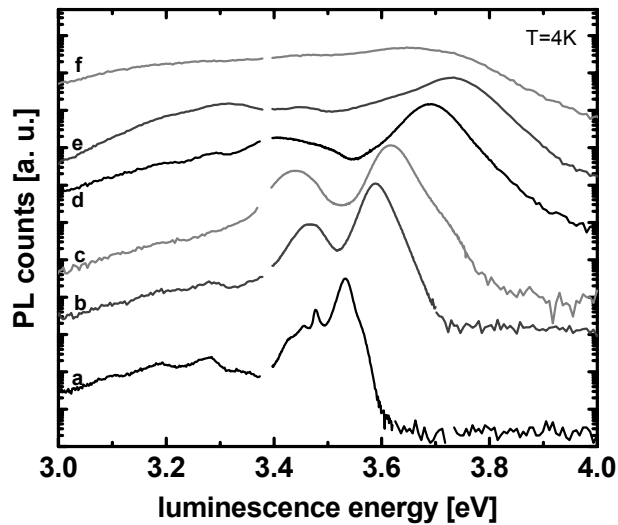


Fig. 1: PL spectra of GaN nanodisks embedded in Al_xGa_{1-x}N barriers. Al-concentration is rising from sample a to f (growth at $BEP_{Al} = 1.5 \times 10^{-8}$ mbar to $BEP_{Al} = 1.2 \times 10^{-7}$ mbar)

¹ phone: +49-89-289-12775, email: furtmayr@wsi.tum.de

² EME/XaRMAE/IN2UB, Dept. d'Electrònica, Universitat de Barcelona, 08028 Barcelona, Spain

³ I. Physikalisches Institut, Justus-Liebig-Universität, Heinrich-Buff-Ring 16, 35392 Gießen

the sample with the lowest Al-concentration (sample a in Fig. 1), increasing up to 115 meV with increasing Al-concentration (sample e). This broadening can be induced by inhomogeneous strain within the NDs. For the sample with the highest BEP_{Al} (sample f in Fig. 1), a decrease of the emission energy to 3.66 eV accompanied by an increase of the FWHM to 270 meV is found. Samples with different well thicknesses show a red shift with increasing thickness, due to the quantum confined Stark effect.

To analyze the shape of the NDs, high resolution TEM was performed on selected AlN/GaN structures. TEM images of the upper part of one particular NW are shown in Fig. 2. The GaN nanowire base region and nine GaN NDs embedded in AlN can be seen in Fig. 2a. Whereas the lateral growth rate of GaN is almost zero, we find a radial growth for AlN with a rate of 11% of the axial growth rate, leading to an increase of the GaN ND diameter from the first to the topmost well. However, the well thickness is constant. Figs. 2 b and c show detailed images of the well region, which is sharply defined and consists of four monoatomic layers. The intermediate AlN barriers are 14 monolayers thick. The sidewalls of the ND are rounded as seen in c.

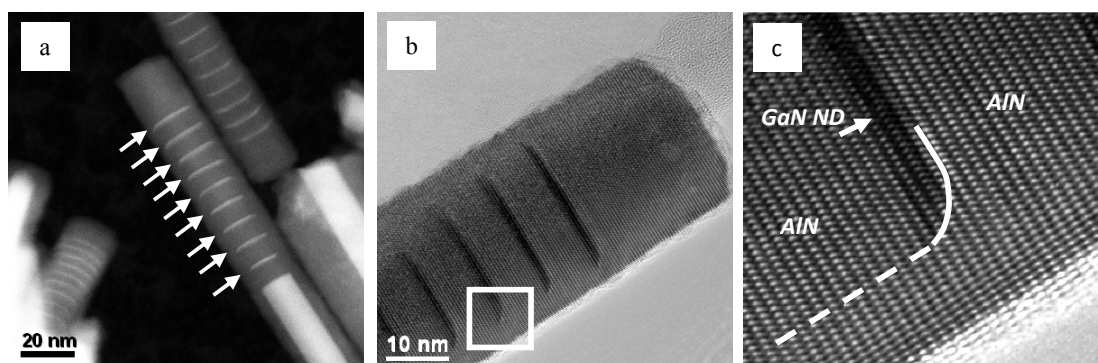


Figure 2: TEM images of an AlN/GaN nanodisk sample:

- a) Recorded under dark-field conditions (Z-contrast). The GaN areas are bright, AlN areas are dark. The nine GaN nanodisks are marked with arrows.
- b) TEM image of the top part in bright field mode.
- c) Detail image of square in b)

- [1] Florian Furtmayr, Martin Vielemeyer, Martin Stutzmann, Jordi Arbiol, Sònia Estradé, Francesca Peirò, Joan Ramon Morante, and Martin Eickhoff, *Journal of Applied Physics* **104**, 034309 (2008).
- [2] Florian Furtmayr, Martin Vielemeyer, Martin Stutzmann, Andreas Laufer, Bruno K. Meyer, and Martin Eickhoff, *Journal of Applied Physics* **104**, 074309 (2008).

We gratefully acknowledge financial support by the Deutsche Forschungsgemeinschaft via NAWACS (Ei 518 2-1) and by the German Excellence Initiative via the Nanosystems Initiative Munich (NIM).

Application of catalytic nanoparticles to Gallium nitride surfaces

Susanne Schaefer¹, Sonja Wyrzgol², Yizhen Wang, and Martin Stutzmann

Wide bandgap semiconductors like GaN have been utilized for a wide range of applications. For those related to surface properties, like bio-functionalization or catalytical activity, it is interesting to understand the charge transfer mechanism over the semiconductor surface onto biomolecules or metal particles (Fig. 1). In this project, platinum nanoparticles are applied to GaN surfaces with a defined distribution to create a catalytically active support. This is a prerequisite for the electrical or optical manipulation of the platinum catalyst via the semiconductor and hence the precondition for switchable catalytic processes.

The targeted charge transfer mechanism is depicted in Fig. 1 for platinum nanoparticles on the p-doped GaN surface of a p/n diode. Upon illumination, carrier separation takes place at the pn-junction and positive charges are available at the metal-semiconductor interface. By partially compensating the electrons of the platinum, the particles can be partially depleted and a change in catalytic reactivity can be expected. In a first approach, thin platinum layers were deposited on clean MOCVD-GaN surfaces with nominal thicknesses of 0.5-15 nm. By subsequent annealing under hydrogen flux for 30 minutes at 500°C, diffusion was enhanced and the platinum atoms coalesced to particles

(Fig. 2 (a)-(f)). This process is clearly influenced by the surface properties of GaN and strongly depends on the annealing temperature. A clear transition from a continuous layer to a non-continuous layer and finally to distinct particles was observed with atomic force microscopy. For very low nominal platinum thicknesses, the necessary diffusivity was reached by an increased annealing temperature of 650°C (Fig. 2 (g)) and 750°C (Fig. 2 (h)), respectively.

The samples prepared by this method showed high reproducibility, as well as stability un-

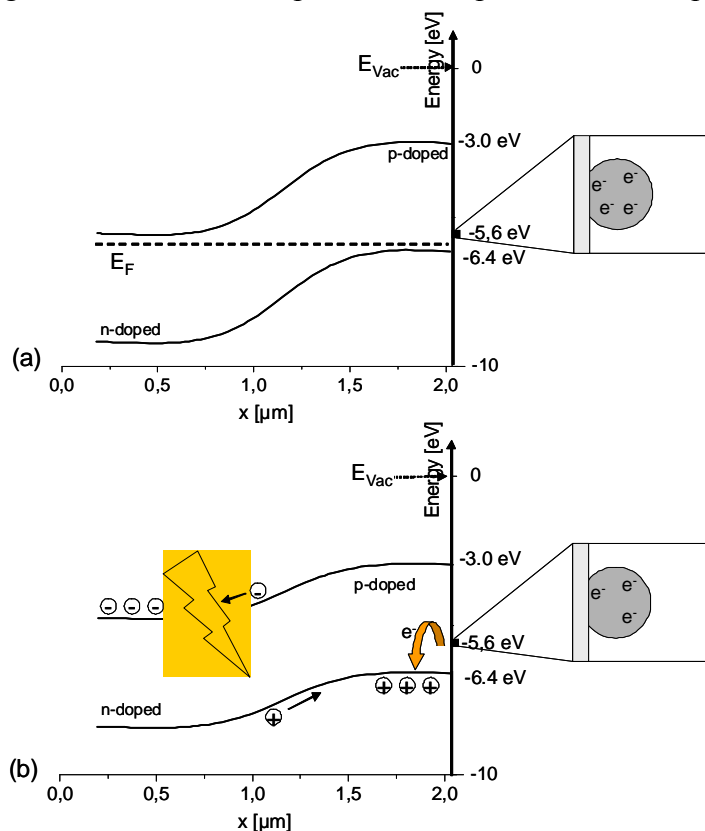


Fig. 1: Schematic of charge transfer between GaN and a platinum nanoparticle upon illumination.

¹phone: +49-89-289-12769, fax: +49-89-2891 2737, email: schaefer@wsi.tum.de

²Lehrstuhl für Technische Chemie, TU München, email : sonja.wyrzgol@ch.tum.de

der nitrogen flux at room temperature. However, all samples exhibit a fairly high surface coverage with Pt. This is not desirable regarding the precise control of catalysis kinetics as well as noble metal consumption. Therefore, platinum nanoparticles were also prepared by an alternative method, namely from chloroplatinic acid hexahydrate ($\text{H}_2\text{PtCl}_6 \cdot 6\text{H}_2\text{O}$). To avoid agglomeration, Poly(N-vinyl-2-pyrrolidone) (PVP) was used as a spacer molecule. The PVP-protected nanoparticles were solved in ethanol and applied to GaN surfaces via spin coating. For sufficiently high rotation time and speed, a homogeneous distribution of platinum nanoparticles was achieved (Fig. 2 (i), (j)). This approach resulted in samples

with a very low surface coverage. Particle sizes were determined to approximately 1.3nm, which is consistent with previous TEM measurements. For both preparation techniques, the total amount of platinum on the surface was quantified by energy dispersive X-ray spectroscopy (EDX). For the relative peak intensities of Pt- $M_{\alpha 1}$ and Ga- $L_{\alpha 1}$ a linear correlation with the layer thickness was found (Fig.3). However, EDX is limited for very low amounts of platinum and does therefore not apply to estimate the total amount of platinum for spin coated samples.

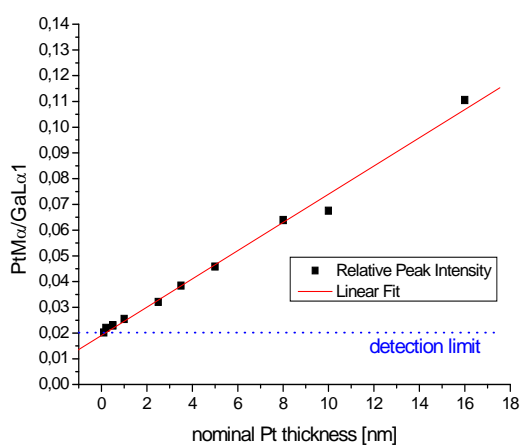


Fig. 3: Relative peak intensities of Pt $M_{\alpha 1}$ and Ga $L_{\alpha 1}$ determined by energy dispersive X-ray spectroscopy.

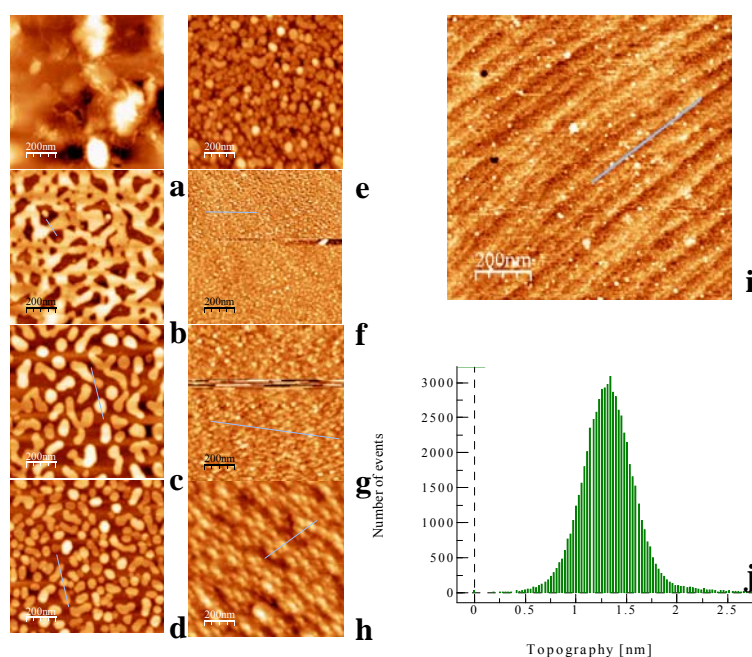


Fig. 2: (a) Atomic force images of physical vapour deposited Platinum films with nominal thickness of 15 nm (a), 5 nm (b), 3.5 nm (c), 2.5 nm (d), 1nm (e), 0.5 nm (f) and 0.2 nm (g and h), spin coated Pt nanoparticles (i) and the resulting height distribution (j).

These first results in sample preparation will be followed by a detailed testing of the catalytic activity via well-known test reactions like hydrogenation of ethylene to ethane. The final task will then be the increase of efficiency and precision of catalytic reactions by optical or electrical excitation of the semiconductor substrates.

Low temperature polycrystalline silicon prepared by aluminum-induced layer exchange for transistor applications

Christian Jaeger¹, Tobias Antesberger, and Martin Stutzmann

Polycrystalline silicon (poly-Si) is of considerable importance for current large area electronics. One reason is the higher field effect mobility obtained with poly-Si in comparison to amorphous silicon devices. High field effect mobilities are especially important for a successful integration of row and column drive circuits for active matrix displays.

In the last years, many alternative preparation techniques for poly-Si besides the widely-used plasma-assisted CVD have been under investigation, in order to achieve a low thermal budget and compatibility with low cost substrates. A possible crystallization method in this context is the aluminum-induced layer exchange (ALILE) process. Here, the catalytic effect of aluminum is exploited to crystallize amorphous silicon or germanium films. For example, an Al/amorphous Si layer stack, which is separated by a thin oxide film, is annealed at temperatures up to 577° C, the eutectic temperature of the Al/Si system. This thermal activation leads to diffusion of silicon atoms into the Al layer, which finally start to form crystallites. After a certain period of time, the Al is totally displaced by silicon grains and the initial layers have exchanged their respective positions. After the process is finished, the Al on top of the crystallized poly-Si film can be removed by wet chemical etching. [1]

In addition, the trend seen in crystalline silicon MOSFET technology of using high-k dielectrics like ZrO₂, Ta₂O₅ and HfO₂ to replace the formally used SiO₂ also begins to have an impact on poly-Si TFT research. Due to the higher dielectric constants the high k-insulating layers can provide the same capacitance for considerably larger film thicknesses, therefore reducing leakage current problems.

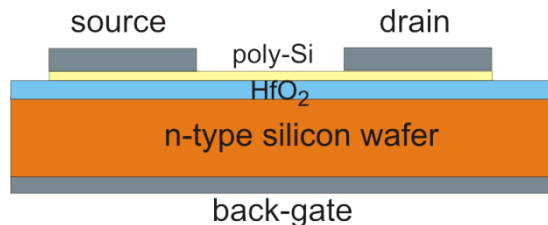


Fig. 1: Schematic sketch of the used back-gate configuration.

To investigate the compatibility of ALILE layers with high-k dielectrics we have grown poly-Si films on a n-type Si wafer/HfO₂ substrate. The highly doped silicon wafer ($\rho=0.003-0.008 \Omega\text{cm}$) is metalized at the bottom side acting as the back gate (see Fig. 1). The poly-Si channel (20 μm width) was defined by pre-structuring of the ALILE precursor layers with photolithography. Finally, Al

was evaporated as source and drain contacts.

Hall effect measurements of such recrystallized films have revealed high hole carrier concentrations in the poly-Si layers up to 10^{19}cm^{-3} due to the solution of Al in the recrystallized silicon. Such high carrier concentrations are not desirable for most electronic applications. Hydrogen plasma treatment can be used to passivate the aluminum acceptors in the polycrystalline silicon layers, which leads to a pronounced increase of the resistivity. The transistor structures shown here were all hydrogenated at 170°C for one hour using a glow discharge plasma.

¹phone: +49-89-289-12768, fax: +49-89-28912737, email: jaeger@wsi.tum.de

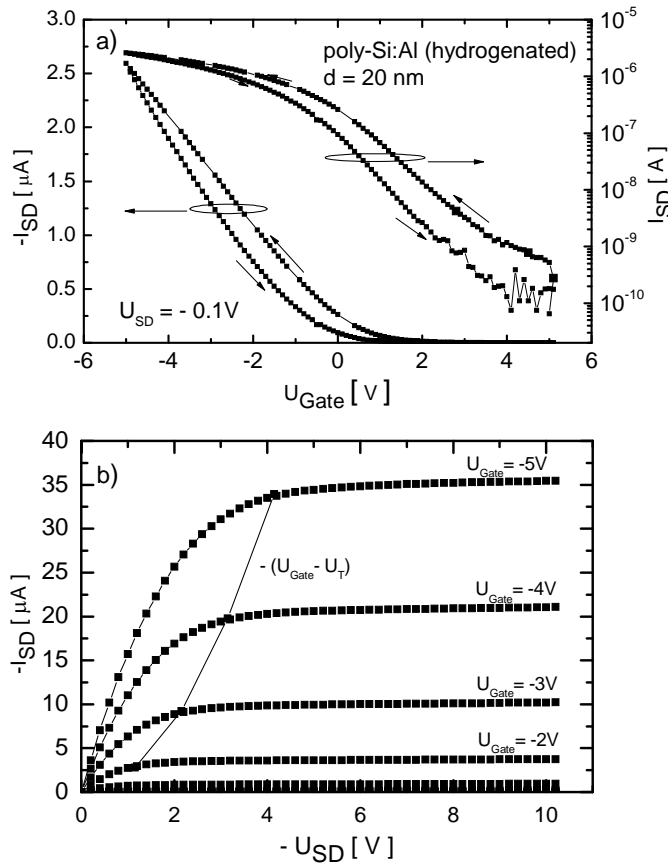


Fig. 2: (a) Source-drain current I_{SD} versus gate voltage on a linear and logarithmic scale. A slight hysteresis can be observed between the forward and backward sweep direction. (b) Output characteristics for different U_{Gate}

the device for different U_{Gate} are plotted in Fig. 2 b). A linear regime at low U_{SD} as well as the saturation of the source-drain current at high U_{SD} are characteristic for the transistor performance of the device. The source-drain voltage $-U_{SD} = -(U_{Gate} - U_T)$ expected for the pinch-off point is also shown for each value of U_{Gate} , and is in good agreement with the observed onset of source-drain current saturation.

In conclusion, transistor performance of devices fabricated with poly-Si films prepared by ALILE on HfO_2 high-k dielectric substrates has been obtained. The considerable amount of charge trapped in the oxide and possibly at the semiconductor/oxide interface might have crucial influence in some applications. Improvements could be obtained by adding a thin SiO_2 layer on top of the HfO_2 as it is done in crystalline silicon technology to improve the quality of the oxide/semiconductor interface.

Reference: [1] O. Nast and S. R. Wenham, J. Appl. Phys., **88**, 124 (2000)

Figure 2.a) shows the source-drain current I_{SD} of a 20 nm thick device on a logarithmic and a linear scale as a function of the gate voltage U_{Gate} . A slight hysteresis is observed between the forward and backward sweep direction, indicating the trapping of charge carriers in the oxide. The threshold voltage shift between the two sweep directions can be used to estimate the trapped charge per unit area to $N_T = \Delta U_T C_{ox}/e = 1.4 \times 10^{12} \text{ cm}^{-2}$, where C_{ox} denotes the oxide capacitance, e the elementary charge and ΔU_T the threshold voltage shift.

From the linear increase of source-drain current I_{SD} at low source-drain voltages U_{SD} , the field-effect mobility μ_{FE} for the holes in the channel has been deduced. A value of $25 \pm 2 \text{ cm}^2/\text{Vs}$ was found for this device.

The output characteristics of

Planar Nanogap Electrodes by Direct Nanotransfer Printing

Sebastian Strobel¹, Stefan Harrer², Guillermo Penso-Blanco², Giuseppe Scarpa², Gerhard Abstreiter, Paolo Lugli², and Marc Tornow³

The ongoing miniaturization of electronic devices in integrated circuits has led to a growing activity towards novel electronic units which eventually may replace or complement current silicon microelectronics in the future. For the integration of molecular electronics with existing silicon technology, nanometer scale metallic contacts have to be reliably manufactured on planar (silicon) substrates to act as contacts to organic molecules.

We have fabricated such planar nanogap electrodes on a silicon substrate, using direct high-resolution metal nanotransfer printing (nTP) (Figure 1) [1]. The mold used is fabricated from a molecular beam epitaxy (MBE) grown GaAs/AlGaAs heterostructure, featuring a nanoscale groove on a cleaved plane. By coating this mold surface with a thin PdAu/Ti film and pressing it against a SiO₂/Si substrate the sectioned metallic thin film is directly transferred onto this substrate, thereby forming the planar nanogap electrodes structure. Here, the choice of PdAu/Ti combines the weak adhesion of PdAu to the GaAs mold with the strong adhesion of Ti to the Si/SiO₂ substrate upon contact and release. This hard-to-hard, one-step transfer printing process is simple and fast, and preserves the mold for manifold transfer. It does neither require any flexible buffer layer, nor any organic adhesion promoters or additional chemical post-processing. The nanogap size is largely predetermined by the chosen architecture of the mold. We carried out successful transfer experiments using different multi-line molds with varying aspect ratios down to below 10 nm gap separation. Based on these investigations we fabricated a pair of transferred homogeneous, large area metal electrodes separated by a gap of about 12 nm (Figure 2). We used FIB milling to section a particular pair of these nanogap

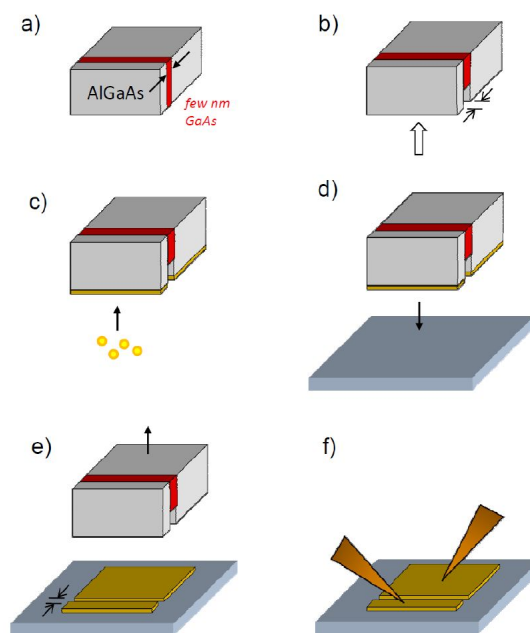


Fig. 1: Schematic of nanogap electrode fabrication by direct nTP. a) MBE-grown-mold comprising a few nm thick GaAs layer embedded in AlGaAs. b) Selective recess-etching of GaAs. c) Deposition of transfer metal thin-film on structured mold. d) Aligning coated mold coplanar to the SiO₂/Si substrate, contacting and pressing it against the same. e) Release of mold: the metal thin film is transferred, leaving a nanogap between two planar metal layers. f) Electrical characterization using sub- μm probe needles.

¹ Phone: +49-89-289-13876, fax: +49-89-320 6620, email: strobel@wsi.tum.de

² Lehrstuhl für Nanoelektronik, TU München

³ Institut für Halbleitertechnik, TU Braunschweig

electrodes into μm width devices and determined their electrical characteristics by using sub- μm probe contact needles. Our nTP nanogap electrodes feature excellent electrical properties in terms of less than $\text{k}\Omega$ lead resistance and gap isolation in the $\text{G}\Omega$ range, measured up to 3V. We expect our novel method to be of large potential for future applications such as molecular nanoelectronics, where the reliable and fast fabrication of nano-scale contacts on planar substrates such as silicon will be required.

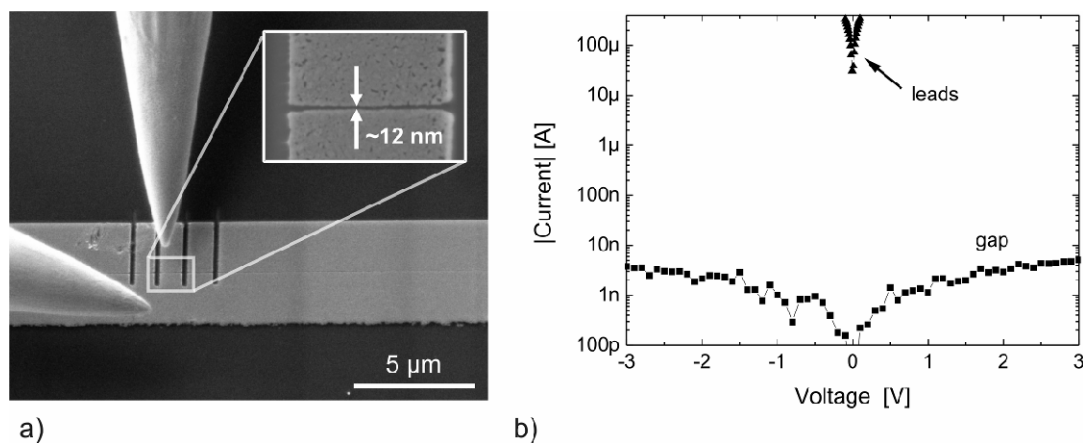


Fig. 2: a) SEM image of a nanogap electrode pair obtained by direct nTP of a 9 nm thick Ti/PdAu film, and contacted by sub- μm probe needles. For electrical testing, the width has been restricted perpendicular to the gap using FIB milling. Here, four vertical broad lines section the metal films into three individual, μm -width electrode pairs. Inset: Close-up of the central electrode pair featuring a smallest gap separation of ~ 12 nm. The granularity of the metal and the apparent gap widening close to its left and right end can be assigned to slight unintentional ion milling (not present in the originally transferred structure). b) Current-voltage (I-V) characteristic of a similar device as shown in a), same smallest gap separation, together with I-V characteristic of the transferred metal film leads, obtained by placing the probe needles on the same elec-

- [1] S. Strobel, S. Harrer, G. Penso-Blanco, G. Scarpa, G. Abstreiter, P. Lugli, and M. Tornow, *Small* (in press, 2009)

Morphological and optoelectronic properties of pentacene thin films on hydrogen- and oxygen-terminated diamond substrates

W. Gajewski¹, F. Buth, M. Huth², B. Nickel², M. Stutzmann, and J.A. Garrido

In the past years pentacene (Pc) has been intensively studied for applications in electronic devices such as organic thin film transistors or solar cells. One of the key parameters governing the electronic properties of all organic semiconductors is morphology and its dependence on the substrate-semiconductor interaction. For Pc thin films, two different types of morphology have been reported *i*) the thin film phase observed on inert substrates, and *ii*) planar chemisorbed Pc monolayer observed on metals. In this work we use diamond as a platform to explore the dependence of the Pc thin films morphology and electronic properties on the surface termination of the substrate.

Due to the different dipole moments of C-O and C-H bonds, the energetic positions of the diamond conduction and valence bands are significantly different for O- versus H-termination. For instance, the hydrogen-terminated diamond has a negative electron affinity. Furthermore, contact angle experiments reveal a lower surface free energy of hydrogenated diamond surfaces as compared to O-terminated substrates. This difference in surface energetics directly influences the Pc thin film morphology, as can be seen in Figure 1, which shows a typical atomic force microscopy (AFM) image of Pc deposited via molecular beam deposition on a O/H patterned (100) single crystalline diamond (SCD) surface.

The Pc texture on oxidized diamond is very similar to the one observed on inert substrates such as SiO₂ [R. Ruiz *et al.*, Chem. Mater. 16, 4497 (2004)], revealing the formation of large Pc islands with a diameter of 0.7-1 μm. Furthermore, the AFM study shows step heights corresponding to the $d_{(001)}$ distance of the thin film phase of pentacene. This is supported by X-ray reflectivity (XRD) experiments performed on polycrystalline diamond films, which revealed Bragg peak separation corresponding to layer spacing of $d_{(001)} = 1.55 \pm 0.15$ nm, typical for the thin film phase.

On the hydrogen-terminated part of the surface, high needle-like islands with an average height of about 150 nm and 0.4-0.5 μm length are observed. Furthermore, two preferential perpendicular orientations of the needle-like structures are distinguishable with an angle of 90° relative to each other. The main crystallographic directions parallel to the surface of a (100) SCD film are (011) and (01-1), which correspond to the directions of the π-bonded C-H dimer chains typical for the diamond (2x1) reconstruction. Additionally, XRD-measurements suggest that the needle-like structures consist of Pc molecules oriented with their long axis parallel to the substrate surface - a morphology

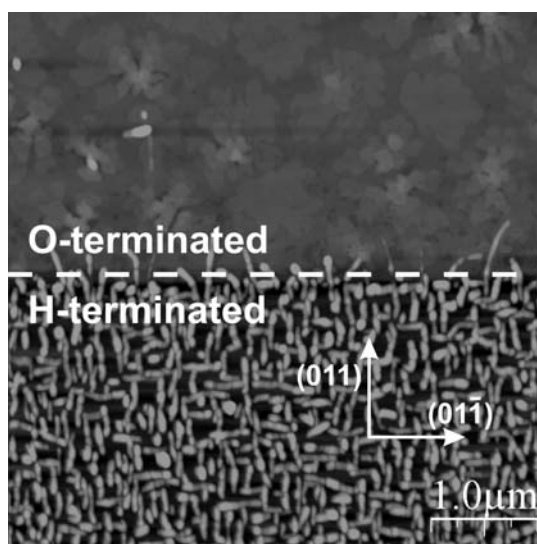


Fig. 1: AFM image of a Pc thin film deposited on an oxygen/ hydrogen patterned single crystalline diamond substrate

¹phone: +49-89-289-12774, email: gajewski@wsi.tum.de

²Soft Condensed Matter Group, Physics Department, LMU, Munich

comparable to previous reports on the morphology of Pc films on metals like gold [D. Käfer *et al.*, Physical Review B 75, 085309 (2007)].

The differences in morphology and Pc molecule orientation are strongly reflected in the optical properties of pentacene thin films (see Fig. 2). For Pc films on oxidized single crystalline diamond (SCD:O), the Pc Davydov-split singlet exciton absorption (S_1) at 1.84 eV and 1.96 eV and the charge transfer exciton (2.11, 2.27 eV) are observed, in good agreement with the data reported previously for inert surfaces. In the case of Pc films on hydrogen terminated single crystalline diamond

(SCD:H), the Davydov splitting is suppressed, and the intensity of the S_1 -state at 1.96 eV has increased. Additional peaks have been observed at 4.0, 4.5, and at 5.4 eV, which correspond to higher lying molecular states of the Pc molecule [M. Pope and C. Swenberg, *Electronic Processes in Organic Crystals and Polymers*, Oxford Science Publications, 1999]. The Davydov splitting of the S_1 exciton peak is related to the presence of two non-equivalent Pc molecules in the crystal unit cell. As observed in anthracene, the S_1 absorption is strongly dependent on the polarization of the incident light, with the highest absorption obtained for the electric field of the light parallel to the crystal a or b axes. The presence of the Davydov S_1 doublet observed for Pc on oxidized diamond suggests that the Pc crystal a - b plane is parallel to the diamond surface. In contrast, for H-terminated diamond the crystal a - b plane is expected to be parallel to light propagation thus reducing the absorption for one of the Davydov doublet peaks. The data presented in Fig. 2 reveal a strong reduction of the 1.96 eV peak intensity, which suggest an almost perpendicular arrangement of the b axis and the E vector of the incoming light. Thus the observed difference in the S_1 absorption supports the Pc arrangement model based on the XRD data. Our observations are in good agreement with the ellipsometry data reported by Dressel *et al.* whose dielectric functions along the crystallographic axes revealed strong electronic excitations at 1.85 eV along a axis and at 1.97 eV for b axis [M. Dressel *et al.*, Optics Express, 16, 19770 (2008)].

Our results show that diamond can be an ideal substrate to investigate the fundamental physical properties of organic thin films. The possibility of controlled manipulation of the diamond surface electronic properties can be further used to tune the morphology and thus the optoelectronic properties of organic thin films.

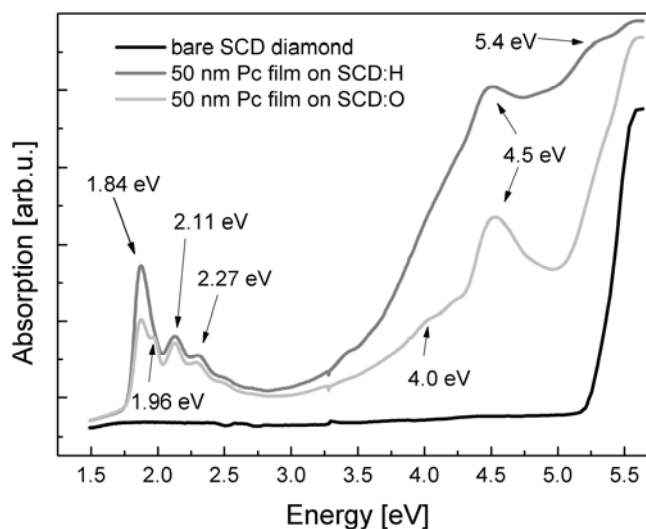


Fig. 2: Optical absorption of 50 nm thick Pc films on oxygen- and hydrogen-terminated diamond and of a bare SCD substrate for comparison.

Light-Induced Charge Transfer in Hybrid Composites of Organic Semiconductors and Silicon Nanocrystals

Roland Dietmueller,¹ Andre R. Stegner, Robert Lechner, Sabrina Niesar, Rui N. Pereira, Martin S. Brandt, André Ebberts,² Martin Trocha,² Hartmut Wiggers,³ and Martin Stutzmann

Charge transfer between Silicon nanocrystals (Si-nc) and organic semiconductors has been investigated via light-induced electron spin resonance (LESR). Composites of Si-nc with the hole conductor poly(3-hexylthiophene) (P3HT) and with the electron acceptor [6,6]-phenyl-C₆₁-butyric acid methyl ester (PCBM) have been investigated. The LESR measurements allow one to quantify light-induced charge transfer between Si-nc and P3HT, which results in positive P3HT polarons. PCBM, in contrast, acts as an electron acceptor in composites with Si-nc, and after illumination, negative PCBM radicals are created. These results are discussed in terms of light-induced generation and separation of charge carriers in the hybrid composites.

In this work, we study the charge transfer between Si-nc and P3HT or PCBM via LESR measurements. Both, for Si-nc/P3HT and Si-nc/PCBM composites, we demonstrate light-induced charge transfer between the organic and the inorganic components of the bulk heterojunction. The intrinsic Si-nc were produced in a 2.45 GHz microwave reactor system at a reaction pressure of 100 mbar and a microwave power of 1800 W from the decomposition of the precursor gas SiH₄ and have a mean diameter of about 33 nm. We have performed ESR and LESR measurements on composites of Si-nc with P3HT or PCBM, which are shown in Fig. 1. In the spectra of the Si-nc/P3HT sample, in the upper part of Fig. 1, two signals of the Si-db with $g=2.0063$ and a width $\Delta H_{pp}=8.0$ G and of the P⁺ with $g=2.0024$ and $\Delta H_{pp}=3.0$ G can be observed. The P⁺ signal, which is already visible in the dark spectrum, increases strongly upon illumination, while the Si-db signal decreases from $1.5 \times 10^{18} \text{ g}^{-1}$ to $1.0 \times 10^{18} \text{ g}^{-1}$, as was already observed in a separate Si-nc sample. A light-induced charge extraction, followed by a charge separation between

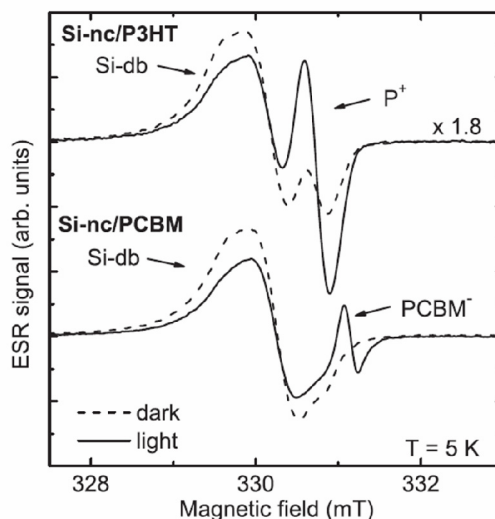


Fig. 1: ESR (dashed line) and LESR (solid line) spectra of Si-nc/P3HT and Si-nc/PCBM composites measured at 5 K. The spectra of the Si-nc/P3HT sample were scaled up by a factor of 1.8.

¹phone: +49-89-289-12783, fax: +49-89-289-12733, email: dietmueller@wsi.tum.de

²Evonik Degussa GmbH, Paul-Baumann-Str. 1, 45772 Marl, Germany

³Institut für Verbrennung und Gasdynamik and CeNIDE, Center for NanoIntegration Duisburg-Essen, Universität Duisburg-Essen, Lotharstr. 1, 47048 Duisburg, Germany

the P3HT and the Si-nc resulting in P^+ can explain the observed LESR spectrum. In the lower part of Fig. 1 the ESR and the LESR spectra of the corresponding Si-nc/PCBM composite sample are shown. In the ESR spectrum only the Si-db signal with $g=2.0064$ and $\Delta H_{pp}=8.1$ G is observed, while in the LESR spectrum a second signal with $g=2.0001$ and $\Delta H_{pp}=1.6$ G appears, which is attributed to photo-induced $PCBM^-$. Again, the Si-db density is reduced to about 60% of the dark Si-db density upon illumination, in this case from $2.8 \times 10^{18} \text{ g}^{-1}$ to $1.6 \times 10^{18} \text{ g}^{-1}$. The appearance of the $PCBM^-$ signal in the LESR spectrum can again be understood by light-induced electron transfer from the Si-nc to the PCBM.

In Fig. 2 (a) the relative energy positions of the conduction band (CB) and valence band (VB) of Si as well as the lowest unoccupied molecular orbital (LUMO) and the highest occupied molecular orbital (HOMO) of P3HT are displayed based on literature values. The LUMO of P3HT lies clearly above the CB of Si, enabling dissociation of excitons followed by electron transfer to the Si CB. However, taking into account the different literature values of the HOMO of P3HT (4.7-5.2 eV) and possible influences on the band alignment, such as Fermi level pinning or interface dipoles, it is a priori not clear if a hole transfer from the Si VB to the P3HT HOMO can take place. For the photo-generation of the P^+ in the Si-nc/P3HT system, one can consider different scenarios: After the light-induced generation of excitons in P3HT, the excitons dissociate by electron transfer to Si, while the holes remain in the P3HT. Alternatively, an energy transfer might occur, whereby excitons are transferred from P3HT to the Si-nc, followed by a back transfer of the holes. A third possibility is that, after light absorption in the Si, the holes are transferred from the Si-nc to the P3HT. In any case, for all processes it is required that the HOMO of P3HT lies energetically above the Si VB. As we indeed do detect light-induced P^+ in the P3HT, we can conclude that this requirement is fulfilled, which is a prerequisite for solar cells based on P3HT and Si-nc. The analogous argument holds for the alignment of the LUMO (3.7-3.8 eV) of PCBM and the CB of Si [Fig. 2 (b)], where we detect $PCBM^-$ anions in the Si-nc/PCBM composite during illumination. Thus the LUMO of PCBM must be energetically lower than the Si CB.

In summary, we have presented LESR measurements on hybrid organic-inorganic Si-nc/P3HT and Si-nc/PCBM composites. Photo-generation of positive P3HT polarons and negative PCBM radicals, respectively, has been detected in these composites via LESR.

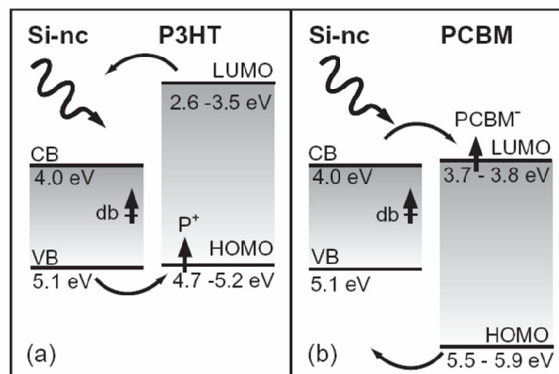


Fig. 2: Schematic view of the energy levels of Si-nc and P3HT (a) and of Si-nc and PCBM (b). The curved arrows indicate the transfer direction of electrons and holes; the vertical arrows illustrate detected paramagnetic states.

This work is part of a cooperation with Evonik Degussa GmbH within the framework of the Science-to-Business Center Nanotronics in Marl which is funded by the state of North Rhine-Westphalia and co-financed by the European Union. Work at the Universität Duisburg-Essen has additionally been supported by the Deutsche Forschungsgemeinschaft (DFG, Graduiertenkolleg 1240).

Characterization of boron-doped nanocrystalline diamond electrodes for electrochemical applications

Tobias Antesberger¹, Jose A. Garrido, and Martin Stutzmann

The purpose of our work is to study the structural, electronic and the electrochemical properties of nanocrystalline diamond to assess its suitability as an electrode for water splitting. For such electrochemical applications, semiconductor electrodes have to provide excellent mechanical, chemical, electronic and optical properties and stability at low cost. Boron-doped nanocrystalline diamond (NCD) electrodes can fulfill all these requirements. Especially in applications like waste water treatment and electrolysis, boron-doped NCD is expected to offer a superior performance.

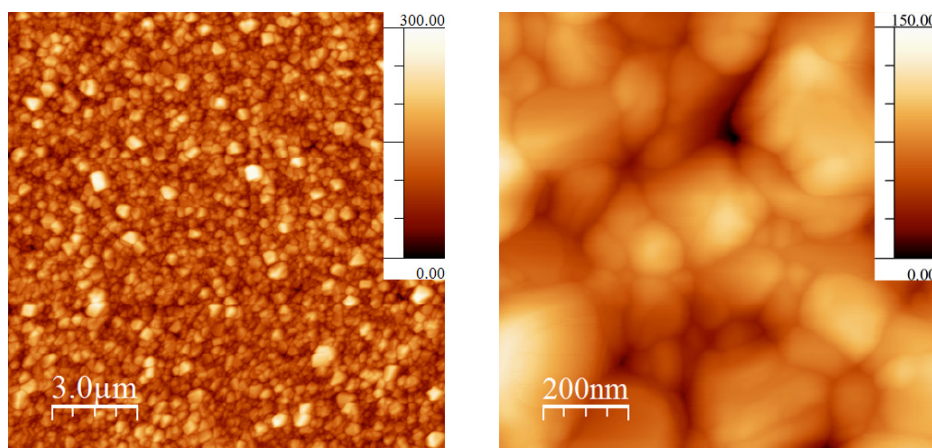


Fig. 1: Atomic force micrographs of boron-doped nanocrystalline diamond grown on a silicon wafer, revealing grain sizes between 50 nm and 200 nm.

We investigate boron-doped nanocrystalline diamond grown on silicon substrates by chemical vapor deposition². The ncd layers are about 1 μm in thickness and consist of grains with a diameter between 50 nm and 200 nm. Figure 1 show atomic force micrographs (AFM) of the studied ncd layers, revealing a homogeneous grain size distribution over the whole area without any pinholes. The root mean square roughness of these films is of the order of 40 nm, so that the effective surface of the ncd layers is increased by about 15 %. This increase of the effective electrode area results in a higher efficiency of the electrolysis.

Furthermore, the electronic properties of the boron-doped nanocrystalline diamond are important to ensure a good electron transfer from the silicon substrate to the diamond/electrolyte interface. The electronic properties of boron-doped ncd are determined by the large band gap of diamond of 5.45 eV and the incorporated boron impurities acting as an acceptor with an ionization energy of 370 meV. For very high boron concentrations, the boron acceptors induce the formation of an impurity band, leading to a good carrier conductivity throughout the ncd layer even at room temperature. We have investigated samples with boron concentrations from 400 ppm to 9000 ppm (boron concentration during the growth) in order to check the influence of doping on the electrochemical stability.

¹phone: +49-89-289-12769, fax: +49-89-289 12737, email: antesberger@wsi.tum.de

²Oliver Williams, Fraunhofer-Institut für Angewandte Festkörperphysik – IAF, Tullastraße 72, 79108 Freiburg i. Br.

For the higher doping levels, the carrier concentrations are typically higher than 10^{21} cm^{-3} and the conductivity reaches values up to $100 \text{ } \Omega^{-1} \text{ cm}^{-1}$. Furthermore, differently doped silicon substrates are used to investigate the electronic properties of the silicon/diamond interface.

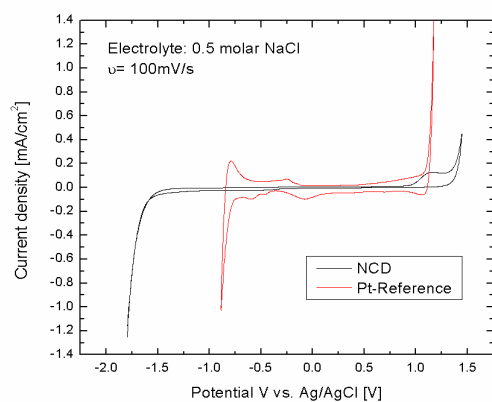


Fig. 2: Potential window of a boron-doped nanocrystalline diamond layer on silicon and a standard Pt electrode, indicating an larger PW and a lower background current for the NCD.

trode electrochemical cell configuration with a Ag/AgCl-reference electrode and a Pt counter electrode was used. The potential window of the ncd ranges from +1.5 V in the anodic region down to -1.8 V in the cathodic direction with a background current density of less than 30 nA/cm^2 . In comparison to the NCD, the potential window of the Pt-electrode is much smaller, ranging from -0.9 V up to 1.2 V, while the background current density is strongly increased to 500 nA/cm^2 .

Figure 3 shows the modulus and the phase of the complex impedance of a NCD layer measured in 0.5 molar NaCl-electrolyte. The frequency response indicates an almost ideal capacitive behavior of the ncd, suggesting that no reaction takes place at the NCD/electrolyte interface.

The chemical stability and therefore the applicability as an electrode can be investigated measuring the electrochemical potential window, which is defined as the potential range where no chemical reaction takes place at the electrode. This is indicated by a low background current across the electrode/electrolyte interface without any characteristic peaks in cyclic voltammetry. The limit of the potential window is defined by the onset of some chemical reactions on the surface indicated by an increase of the current density. Figure 2 compares the potential window of a NCD layer and a Pt electrode measured with a scan rate $\nu = 100 \text{ mV/s}$ in a 0.5 molar NaCl-electrolyte. A three elec-

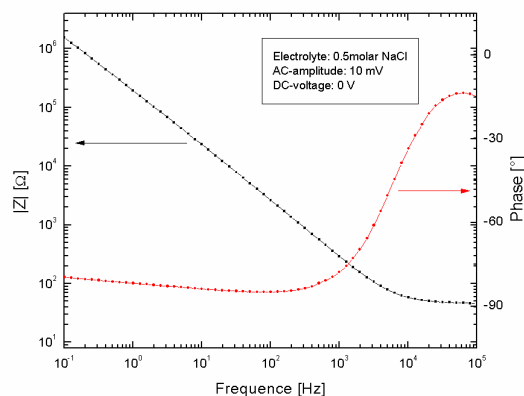


Fig. 3: Impedance spectroscopy of ncd in 0.5 molar NaCl. Modulus as well as the phase show an almost capacitive behavior of the sample.

Optoelectronic Sensitization of Carbon Nanotubes by CdTe Nanocrystals

B. Zebli¹, A. Hartschuh², I. Carmeli², H.A. Vieyra¹, J.P. Kotthaus¹ and A.W. Holleitner

Recently, we have demonstrated how to build hybrid nanoscale devices, which are made out of carbon nanotubes, photosynthetic reaction centers [1], and submicron graphite beads [2]. In addition,

we bound CdTe nanocrystals to single-walled carbon nanotubes via molecular recognition of the linker molecules biotin and streptavidin [Fig. 1(a)]. We investigated the photoconducance properties of such a carbon nanotube-nanocrystal-

hybrid, and we found that the photoconducance of the hybrid material can be adjusted by the absorption characteristics of the nanocrystals. The photoconducance of the hybrid systems shows contributions of different relaxation processes. Our observations are consistent both with a bolometrically induced current increase in the nanotubes caused by photon absorption in the nanocrystals and with a Förster resonance energy transfer from the nanocrystals to the nanotube [3].

- [1] I. Carmeli, M. Mangold, B. Zebli, L. Frolov, C. Carmeli, S. Richter, A.W. Holleitner *Advanced Materials* 19, 3901 (2007).
- [2] L. Song, A. W. Holleitner, H. Qian, A. Hartschuh, M. Döblinger, E. M. Weig, J. P. Kotthaus, *J. of Phys. Chem. B* 112, 9644 (2008).
- [3] B. Zebli, H.A. Vieyra, I. Carmeli, A. Hartschuh, J.P. Kotthaus, A.W. Holleitner, arxiv 0807.2111.

¹Lehrstuhl für Festkörperphysik Prof. Dr. Jörg. P. Kotthaus, Ludwig-Maximilians-Universität München, Geschwister-Scholl Platz 1, 80539 München.

²Department für Chemie, Physikalische Chemie, Ludwig-Maximilians-Universität München, Butenandtstr. 5-13 E, 81377 Munich, Germany.

³Department of Chemistry and Biochemistry, Tel-Aviv University, Tel-Aviv 69978, Israel.

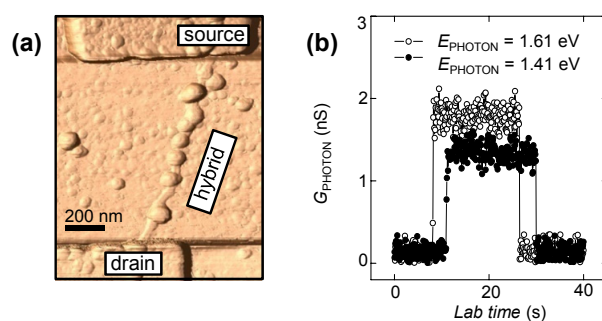


Fig. 1. (a) Atomic force microscope (AFM) image of an individual nanotube-nanocrystal-hybrid contacted by source and drain electrodes made out of Pd. The carbon nanotubes build the backbone of the hybrid structure, while the spherical particles in the AFM image are the CdTe nanocrystals. (b) Typical photoconducance measurement of an ensemble sample made of nanotube-nanocrystal-hybrids as a function of the laboratory time at $E_{\text{PHOTON}} = 1.61 \text{ eV}$ (open circles) and $E_{\text{PHOTON}} = 1.41 \text{ eV}$ (black circles). B. Zebli et al. found an enhanced photoconducance at photon energies larger than the recombination energy of the CdTe nanocrystals at $\sim 1.59 \text{ eV}$ [1].

Device Physics

Towards an Electro-Optically Driven Single Photon Device

Roland Enzmann, Christian Jendrysik, Christian Seidel, Andreas Heindl, Daniela Baierl, Gerhard Böhm, Ralf Meyer, Jonathan Finley and Markus-Christian Amann

As a prototype towards a single photon source we present a quantum-dot-based device, which is fully electrically operated. Both the electrical pumping process and the manipulation of the emission wavelength of the quantum dots are independently achieved in this three-terminal device.

Single photon applications such as quantum key distribution require efficient single photon sources. Single quantum dot diodes [1,2] are a promising approach to realize an electrically driven single photon source even at telecommunication wavelengths [3]. They exhibit true single photon emission but still lack of high extraction efficiencies due to the high refractive index difference of the semiconductor-air interface. Several light collection strategies raising the efficiency have been demonstrated to date. Examples include micro-cavities and photonic crystal structures. Every system which deals with quantum dots and micro cavities needs a tuning mechanism, to adjust the quantum dot wavelength and the cavity mode. For a practical device it is highly demanded that the tuning of the emission wavelength as well as the excitation of the quantum dots should be implemented electrically.

An electric field at the location of the quantum dots will lead to a red shift of its emission wavelength due to the quantum confined Stark effect. Since this tuning method needs no current flow, the electric field can be generated by a reverse-biased Schottky contact. On the other hand a simultaneous carrier injection by current is not possible in this configuration. This approach will therefore make a direct carrier injection, as presented for single quantum dot LEDs impossible.

Our approach to realize an electrically driven device which allows simultaneous electrical tuning of the quantum dots and the implementation of a high quality photonic crystal structure, for high efficiency, is to inject the carriers into the dots via a light pulse generated by a monolithically integrated light emitting diode (LED). The schematic structure is shown in Fig. 1, consisting of two

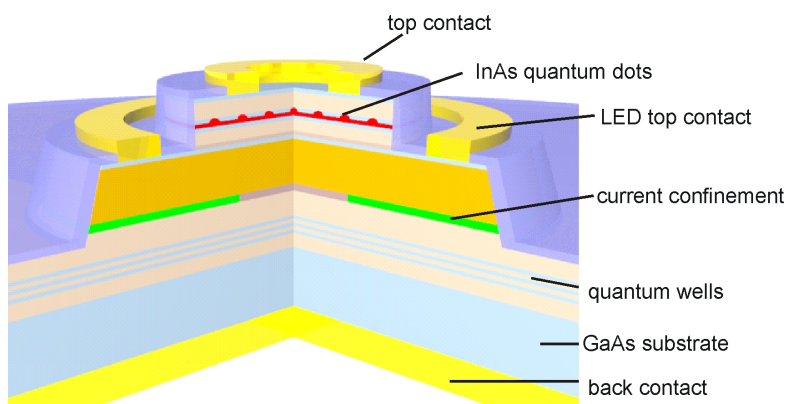


Fig. 1 Schematic figure of the device: In the upper mesa structure a layer of quantum dots is embedded. The LED structure underneath the quantum dots is used to pump the quantum dots in the upper mesa optically.

¹phone: +49-89-289-12759, fax: +49-89-320 6620, email: enzmann@wsi.tum.de

mesa structures. In the upper mesa the quantum dots are embedded, which serve as a single photon emitter. The lower mesa is necessary to fabricate the LED structure. The device is based on GaAs substrate. A process for a first device with implemented photonic crystal was established, as shown in Fig. 2. The photonic crystal was fabricated on the sample structure shown in Fig. 1 before the fabrication of the pumping LED.

Measurements on the resonant excitation of the quantum dot region using the LED as pumping source were performed. The emission of the LED was around 870 nm and was designed to generate light that is reabsorbed in the quantum dots and the wetting layer. We measured a sharp emission line at 948 nm from a quantum dot increasing in intensity with increasing current of the LED (in the range of 5-10 kA/cm²).

For tuning of the emission of the quantum dots, an electrical field at the location of the quantum dots is used, while a reverse bias between the *n*-top-contact and the *p*-LED-top-contact is applied. A Stark shift of about 0.8 nm was achieved.

In summary, these first measurements prove the feasibility of our concept to realize an electrically driven, high efficient single photon emitter. Due to the third contact, a separate pumping of the quantum dots by the two lower contacts and tuning of the emission wavelength of the quantum dots by the upper contacts is possible. Fig. 2 shows, that the fabrication process is compatible with a photonic crystal, and the device has therefore the potential to act as an efficient fully electrically driven single photon source.

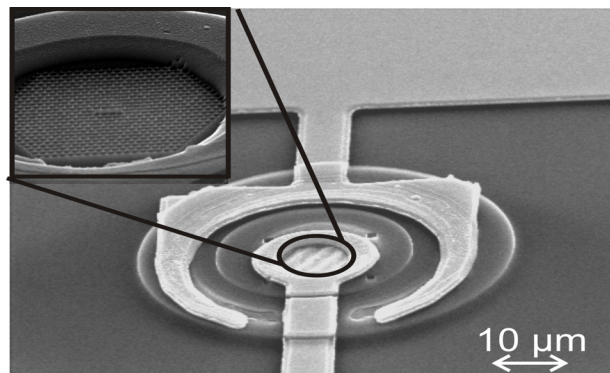


Fig.2. First device with photonic crystal inside the upper mesa

References:

- [1] Z. Yuan, B. E. Kardynal, R. M. Stevenson, A. J. Shields, C. J. Lobo, K. Cooper, N. S. Beattie, D. A. Ritchie, M. Pepper “*Electrically Driven Single-Photon Source*”, *Science* 295, pp. 102 – 105, January 2002
- [2] M. Scholz, S. Büttner and O. Benson, A. I. Toropov, A. K. Bakarov, and A. K. Kalagin, A. Lochmann, E. Stock, O. Schulz, F. Hopfer, V. A. Haisler, and D. Bimberg, “*Non-classical light emission from a single electrically driven quantum dot*” *Opt. Express* 13, 9107, April 2007
- [3] A.J. Bennett, D.C. Unitt, P. See, and A. J. Shields, P. Atkinson, K. Cooper and D.A. Ritchie, “*Microcavity single-photon-emitting diode*”, *Appl. Phys. Lett.* 86, 181102, April 2005

1.55 μm VCSEL with Enhanced Bandwidth and Temperature Range

Werner Hofmann¹, Michael Müller, and M.-C. Amann

Vertical-cavity surface-emitting lasers (VCSELs) with internal bandwidths exceeding 20 GHz have been presented recently emitting in the near infrared spectrum around 850 nm [1]. However, this waveband can only be used for short distances, therefore, there has been vast effort in developing long-wavelength, high-speed VCSELs with steady improvement. Especially long-wavelength VCSELs with buried tunnel junction (BTJ) have shown promising results and record-high modulation bandwidths [2]. With 100G Ethernet standards in discussion, parallel approaches of 8x12.5Gb/s, 6x17Gb/s and 4x25Gb/s are suggested, favoring higher serial bandwidth due to cost issues. 7-8 GHz modulation bandwidth is well sufficient for data transmission at 10 Gb/s, therefore 10 GHz, 13 GHz, and 19 GHz laser bandwidth are to be accomplished for the projected higher data-rates This should be achieved with a cost-effective device at long wavelengths and high temperatures up to 85°C for uncooled operation.

The lasers under investigation were grown in our institute by molecular beam epitaxy on InP substrate. The high-speed 1.55 μm VCSEL structure is an improved version of the high-speed device as described in [2], with optimized active region, detuning, mirror-reflectivities and doping levels. The schematic layout of the laser chip is shown in Fig. 1. BCB is used as low-dielectric constant passivation to enable high-speed operation. The epitaxial output mirror consists of 32 pairs of InGaAlAs and InAlAs with no fundamental absorption. To achieve high-speed operation and sufficient gain at elevated temperatures, the active region consists of 7 compressively strained quantum wells. The strain was tailored to be 2.5% of compressive strain (pseudomorphic) going near borderline of critical layer thickness. This should both enhance gain and differential gain and therefore enable low threshold currents and high relaxation oscillation frequencies. The mode-gain offset is optimized for high-temperature behavior. So, negative T_0 values can be obtained, i.e., the threshold current is lowest at 60°C heat-sink temperature for this device. This effect is caused by the different red-shift of gain and cavity-mode over temperature. Due to the BTJ, which allows the elimination of nearly all p -

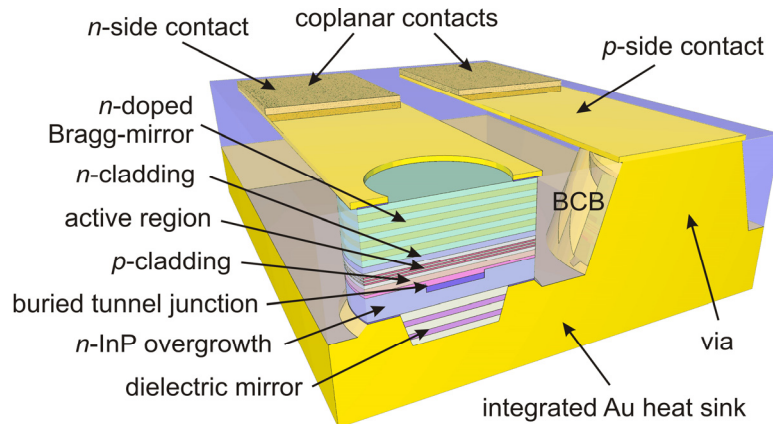


Fig. 1: Schematic cross-section of a high-speed 1.55 μm InP-based BTJ VCSEL. The device is mounted epi-down on a electroplated gold pseudo-substrate. The InP substrate is removed while manufacturing. Both n- and p-contact can be accessed on top. Contact-pad capacitances are minimized.

Due to the BTJ, which allows the elimination of nearly all p -

¹phone: +49-89-289-12786, fax: +49-89-320 6620, email: hofmann@wsi.tum.de

conducting material with higher electrical resistances and optical losses, a differential series resistance of $40\text{-}50\ \Omega$ has been achieved, well suited for high-speed devices.

Even though our devices in reference design [2] showed excellent high-speed behavior for chip diameters of $28\ \mu\text{m}$, the parasitic pole of the reference design was at $4.5\ \text{GHz}$ for a $40\ \mu\text{m}$ device limiting the bandwidth to $6.7\ \text{GHz}$, as presented in Fig. 2. In the improved design, this parasitic capacitance was significantly lowered, with a parasitic-roll off frequency

and modulation bandwidth of around $7\ \text{GHz}$ and $9\ \text{GHz}$, respectively, as depicted in Fig. 2. This is achieved by reducing the doping levels of the blocking diode next to the BTJ from 5 to $1\cdot 10^{17}\ \text{cm}^{-3}$ causing wider space-charge regions and smaller parasitic capacitances. Low parasitics are especially important for VCSELs, as the internal modulation behavior shows higher damping, due to very high carrier and photon densities in the optical resonator. Therefore, VCSELs are characterized by a smaller relaxation oscillation overshoot which could compensate a parasitic roll-off. In Fig. 2, a superior modulation performance can be identified over a wide temperature range. The VCSEL under investigation is not designed for peak-performance at a certain fixed temperature, but optimized for uncooled operation with superior and constant performance. With the reference design, $8\ \text{GHz}$ modulation bandwidth seemed to be the limit at 85°C . As can be seen in Fig. 2, the 3-dB bandwidth is now as high as $10\ \text{GHz}$ at 85°C .

Moreover, for classical distributed feed-back lasers, the output-power at a certain bias current is strongly dependent on the heat-sink temperature, requiring a monitoring and closed-loop control of the laser power, raising the cost of the laser package. As demonstrated in Fig. 5, the VCSEL peak-power P_{max} scales linearly down with temperature, but remains practically constant for a given driving current, e.g. $5\ \text{mA}$ in this case, keeping the laser power P_{opt} around $1\ \text{mW}$. Furthermore, the modulation bandwidth f_{3dB} at $5\ \text{mA}$ is well sufficient for 10-Gb/s over a temperature-range from $0\text{-}85^\circ\text{C}$. This was achieved by an optimized mode-gain offset resulting in a minimum threshold current I_{th} at 60°C .

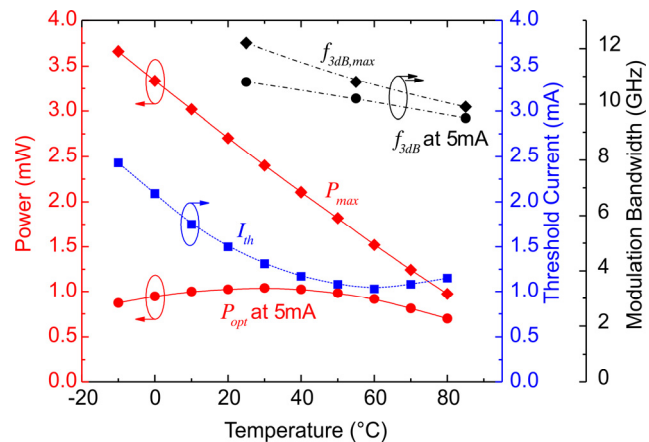


Fig. 2: Temperature behavior of VCSEL output-power, threshold current and modulation bandwidth. Single-mode power and bandwidth are practically constant at $5\ \text{mA}$ driving current, redundanzizing monitor diodes.

- [1] P. Westbergh, J. Gustavsson, Å. Haglund, H. Sunnerud, and A. Larsson, *Electron. Lett.* **44**, 907-908, (2008)
- [2] M.-C. Amann, and W. Hofmann, "InP-based long-wavelength VCSELs and VCSEL arrays", *IEEE J. Sel. Topics Quantum Electron.*, to be published in 2009

Low-threshold and high-performance injectorless quantum cascade lasers using four different material alloys

S. Katz¹, A. Vizbaras, G. Boehm, M.-C. Amann

Up to now, most quantum cascade laser designs only used AlInAs and GaInAs layers, strain balanced on InP. The best threshold performance up to 2007, was reached by the injectorless design with 0.73 kA/cm^2 [1], while the output power was as low as 70 mW at room temperature.

Recent work on injector-less quantum cascade lasers focused on the implementation of multiple material alloys within the active region. Besides the already used AlInAs and GaInAs alloys, the implementation of small AlAs layers, for a controlled increase of the barrier height, showed improved temperature performance, regarding the characteristic and the maximum operation temperature [2]. Additionally very thin InAs layers, in the range of two monolayers, are able to increase the dipole matrix element and the life times, especially of the upper laser level, due to their reduced effective mass. As starting point the reference design [1] was improved, by the implementation of AlAs and InAs, and optimized with a sophisticated simulation algorithm. The theoretical results showed a gain coefficient improvement of 30 %, while keeping the emission wavelength and the period length the same. Figure 1 shows the original injectorless and the improved design.

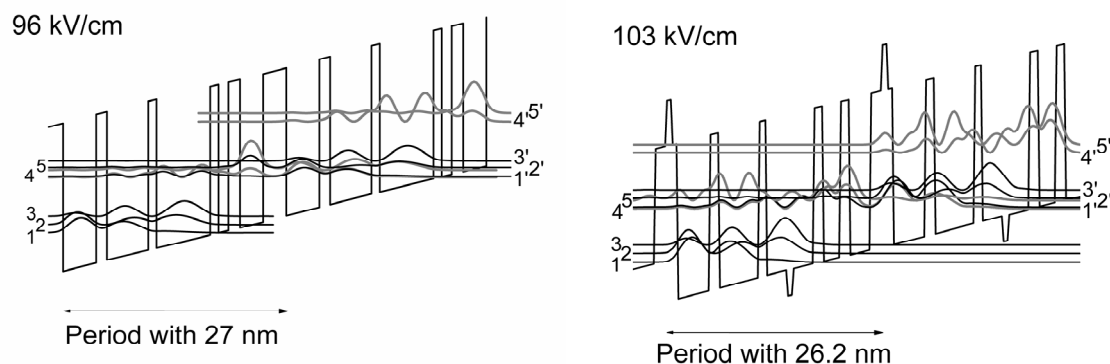


Fig. 1: Active region designs of a classical injectorless quantum cascade laser (left) and an AlAs-InAs improved design (right), both structures require similar fields at equal emission wavelengths and period lengths

The samples were grown on a solid source molecular beam epitaxy, using the same waveguide design for both. The lasers were processed, using wet etching, silicon-dioxide passivation and regular Ti/Pt/Au contacts for bonding to form ridge guide mesas of $26 \mu\text{m}$ width.

While the reference laser showed a threshold current density of 0.73 kA/cm^2 , the improved design reached 0.57 kA/cm^2 for an uncoated device, with a doping sheet density of

¹WSI. Corresponding author: UR, phone: +49-89-289-12785, email: katz@wsi.tum.de

$2.5 \times 10^{10} \text{cm}^{-2}$. This equals an improvement of 28 %, close to the theoretical predictions. When covering the back facet with a high reflectivity coating, a record low threshold performance of 450 A/cm^2 was reached. Additionally to improving the threshold performance, the characteristic temperature had also been improved from 90 K to 140 K for the low doped samples and from 110 K to 160 K for samples using a higher doping sheet density (Figure 2) [3].

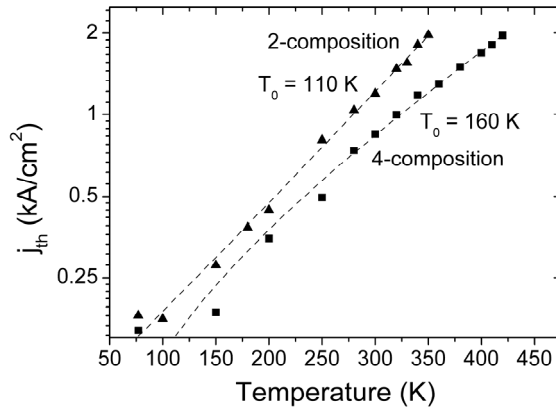


Fig. 2: Threshold current density over temperature for the reference and the new design, doping sheet density of $5 \times 10^{10} \text{cm}^{-2}$

power conversion performance, has been increased from 0.5 % to 1.3 %.

In conclusion, we have demonstrated the possible performance increase by using more than two material alloys. The additional degree of freedom allows optimized designs for quantum cascade lasers. Further development steps could be the implementation of multiple InAs peaks and even quaternary material alloys for stepped quantum wells. Comparing injector-less devices with the best performing injector-based quantum cascade lasers shows the need of moving to shorter wavelengths.

[1] A. Friedrich, C. Huber, G. Boehm and M.-C. Amann, *Electron. Lett.*, **42**, (2006)

[2] A. Friedrich, et al, *Semicond. Sci. Technol.*, **22**, 218-221, (2007)

[3] S. Katz, G. Boehm, and M.-C. Amann, *Electron. Lett.*, **44**, pp. 580-581, (2008)

[4] G. Boehm, S. Katz, and M.-C. Amann, *J. Crystal Growth*, (2008)

When comparing the maximum temperatures of 320 K and 360 K for the two alloy and the four alloy design, the effect of AIAs increased barriers becomes visible. Figure 3 shows the output power vs. the current for devices of $26 \mu\text{m}$ in width and 4 mm in length [4]. The improvements between the original design, yielding a maximum output power of 70 mW and a slope efficiency of 380 mW/A, and the new design, reaching 240 mW and a slope efficiency of 630 mW/A, are clearly visible. Additionally, the output power and slope efficiency of the coated device is presented. The wall-plug efficiency, indicating the overall

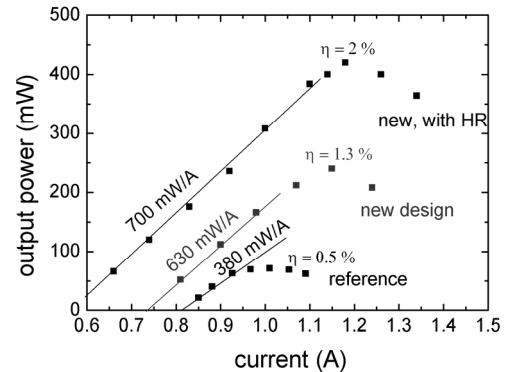


Fig. 3: Output power vs. current for the reference and the new design, with and without HR-coating

Active regions for GaSb-based laser diodes in the mid infrared wavelength range

Kaveh Kashani-Shirazi¹, Alexander Bachmann, Shamsul Arafin, Kristijonas Vizbaras, and M.-C. Amann

GaSb-based lasers are ideal light sources for tunable diode laser absorption spectroscopy (TDLAS) [1], as they can access the mid-infrared wavelength range (2 – 4 μm), where a lot of industrially important gases show strong absorption lines [2]. Recently, electrically pumped VCSELs emitting at 2.3 μm could be realized [3] and open the technology for low cost applications. The challenge gets harder with rising wavelength as absorption losses and Auger recombination increase. We investigated active regions consisting of GaInAsSb-quantum wells in AlGaAsSb or GaSb barriers. We present an enhanced simulation of the current flow in the active region under operation conditions. The calculation includes carrier transport by drift, diffusion and tunnelling. Active regions with various barrier materials were incorporated into edge emitter samples to evaluate their performance. We introduce an improved waveguide design and MBE growth at low temperatures yielding ultra-low threshold current densities of 50 A/cm² ($L \rightarrow \infty$) in cw operation at room temperature.

The edge emitters were grown on an n -type GaSb substrate. The growth starts with a 2 μm thick cladding layer of $\text{Al}_{0.50}\text{Ga}_{0.50}\text{As}_{0.04}\text{Sb}_{0.96}$ with a Te doping of $2 \times 10^{18} \text{ cm}^{-3}$ followed by a 400 nm undoped $\text{Al}_{0.10}\text{Ga}_{0.90}\text{As}_{0.01}\text{Sb}_{0.99}$ waveguide layer. Next, one 15 nm wide $\text{Ga}_{0.57}\text{In}_{0.43}\text{As}_{0.14}\text{Sb}_{0.86}$ quantum well (QWs) is sandwiched between 8 nm GaSb barriers. The p -side is equivalent to the n -side but with a Si doping of $5 \times 10^{17} \text{ cm}^{-3}$ in the cladding and is followed by a highly p -doped GaSb contact layer. The simulated band diagram of the structure under laser operation is shown in Fig 1. The electrical design of the laser structures was optimized by using the in house simulation tool nextnano+ [4]. Further details on the simulation and design work is given in [5]. All samples were grown in a Varian Gen-II-MBE system with solid sources and valved cracker cells for Arsenic and Antimony. The growth temperature of the active region was set to 430°C for an optimum material quality in the quantum well. The layers on the top were grown at 430°C to avoid thermal degradation of the active region.

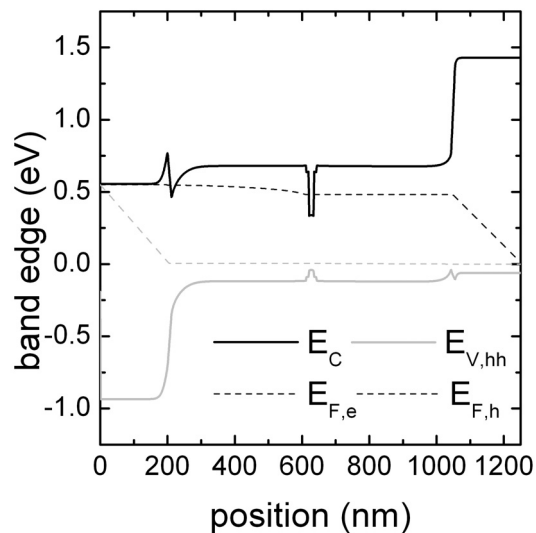


Fig. 1: Band diagram and Fermi level calculation of the edge emitters under lasing conditions

¹phone: +49-89-289-12788, fax: +49-89-320 6620, email: kashani@wsi.tum.de

After epitaxy, ridge waveguide edge emitters with stripe widths ranging from 15 to 200 μm were processed, cleaved and mounted epi-side up. No facet coating was applied. The measurements were made on a temperature controlled heat sink. The devices show multi-mode cw laser emission at 2.65 μm at temperatures up to 55°C. Fig. 2 a) shows the measured threshold current densities including a measured lateral carrier broadening of 3.1 μm on each side due to current spreading and diffusion. The lowest measured value was about 74 A/cm² for a 5.0 mm long device. These are the lowest values reached so far for lasers at this wavelength and can be compared even with the well known GaAs and InP material systems at much shorter wavelengths. The device shows a low internal loss of about 3 cm⁻¹ and a characteristic temperature of $T_0 = 62$ K. The good temperature behavior indicates that carrier leakage out of the QW is not a major loss component. The optical output power versus current and voltage versus current characteristics of a 1.6 mm long and 60 μm wide device are shown in fig 2 b). The measured maximum cw output power is 20 mW for both facets, limited by the current source. The superior device performance derives from the improved design and excellent material quality of the low temperature MBE growth.

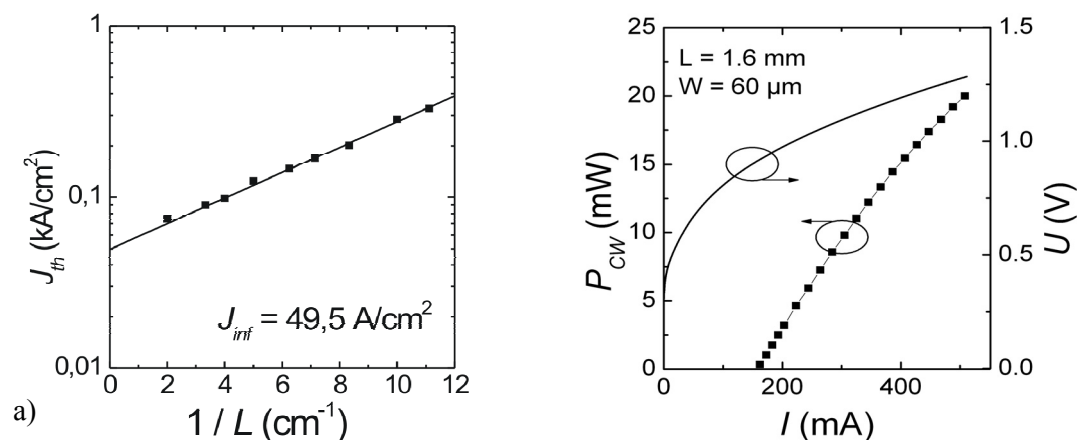


Fig. 2: a) Threshold current densities versus the inverse length. b) Power versus current and voltage versus current characteristics of the 2.65 μm laser.

- [1] A. Vicet, D.A. Yarekha, A. Pérona, Y. Rouillard, S. Gaillard and A.N. Baranov, "Trace gas detection with antimonide-based quantum-well diode lasers", *Spectrochimica Acta Part A* 58, 2405-2412 (2002).
- [2] L. Rothman, "The HITRAN 2004 molecular spectroscopic database," *Journal of Quantitative spectroscopy & Radiative Transfer* 96, 139–204 (2005).
- [3] A. Bachmann, T. Lim, K. Kashani-Shirazi, O. Dier, C. Lauer, M.-C. Amann, "Continuous-wave operation of electrically pumped GaSb-based vertical cavity surface emitting laser at 2.3 μm ", *Electron. Lett.* 44(3), 202 - 203 (2008).
- [4] see <http://www.wsi.tum.de/nextnano> for obtaining the nextnano executables and related publications
- [5] K. Kashani, A. Bachmann, G. Boehm, S. Ziegler, M.-C. Amann, "MBE Growth of active regions for electrically-pumped, cw-operating GaSb-based VCSELs", *J. Crys. Growth* (2008), doi:10.1016/j.jcrysgro.2008.09.208.

Low-resistive ohmic contacts to n -InAs_{0.91}Sb_{0.09} for GaSb-based VCSELs in the mid-infrared range

S. Arafin¹, A. Bachmann, K. Kashani-Shirazi, S. Priyabadini and M.-C. Amann

GaSb-based vertical-cavity surface-emitting lasers (VCSEL) are one of the most promising candidates for realizing trace-gas sensing systems using tunable diode laser absorption spectroscopy (TDLAS) in the mid-infrared wavelength regime [1]. Single mode, continuous-wave electrically pumped GaSb-based VCSELs operating at $\sim 2.3 \mu\text{m}$ up to 50°C [2] and CO and CH₄ sensing systems utilizing these lasers [3] have been demonstrated recently. For these lasers, good quality ohmic contacts play a very important role in obtaining high performance and good reliability. Otherwise, high resistivities appear in the devices which heat up them during the operation and ultimately their performances get deteriorated.

In this article we present low resistive and thermally stable ohmic contacts to lattice-matched MBE grown Te doped n -type InAs_{0.91}Sb_{0.09} layers which are suitable for GaSb-based VCSELs. The reason for using InAsSb as the contact layer is that this material can be doped up to as high as $1 \times 10^{20} \text{ cm}^{-3}$, which overcomes the problem of the doping limit for Te dopant in n -type GaSb (maximum $3 \times 10^{18} \text{ cm}^{-3}$) [4]. Besides, the main challenge of getting very good ohmic contacts on GaSb-based material system is to avoid the native oxides which form very quickly on the surface of these materials compared to the GaAs-based material system [5]. Consequently, special surface treatment in addition to the conventional acid dipping becomes necessary to minimize the surface oxides prior to metallization. Lauer et al. [6] demonstrated a procedure of removing the native oxides by Ar-plasma based dry etching and subsequently depositing the Ti/Pt/Au metals. Furthermore, low resistance unannealed ohmic contact on n -type InAs_{0.66}Sb_{0.34} has been developed by Champlain et al. [7] which is highly strained to GaSb.

The test samples used in this study consist of $500 \mu\text{m}$ Te doped n^+ -GaSb-substrate with resistivity and doping concentration $0.0024 \Omega \text{ cm}$ and $1 \times 10^{18} \text{ cm}^{-3}$ respectively followed by a 500 nm thick Te doped ($3 \times 10^{18} \text{ cm}^{-3}$) n -GaSb buffer layer and finally a 50 nm thick n^+ -InAsSb contact layer. After the growth, we defined the circular mesa using wet chemical etching where the contact layer and a few nm of the GaSb buffer layer are removed. Then we covered the mesa with 150 nm of sputtered SiO₂ as a passivation layer and removed this layer from the top of the mesas by a lift-off process to form circular contact openings. Afterwards, a wet chemical etching step e.g. HCl dipping was involved to remove the surface oxides and then, for preventing the further formation of the oxides, the samples were rinsed with 2.8% (NH₄)₂S (with pH = 9.5) for 40 s and promptly loaded into the metallization chamber afterwards for evaporating the metals Ti/Pt/Au sequentially at the top and backside contacts. However, the fabricated contact test structure is displayed in Fig. 1.

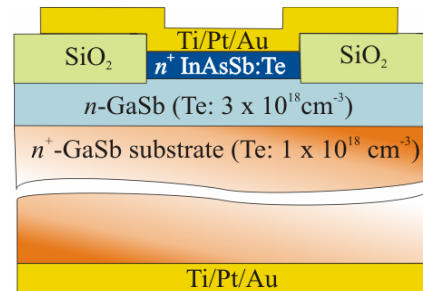


Fig. 1: The contact test structure after all the processing steps

¹phone: +49-89-289-12788, fax: +49-89-320 6620, email: arafin@wsi.tum.de

It is expected that by the sulfide passivation process, the dangling bonds at the contact surface are terminated in the form of S-In, S-As and S-Sb, which also leads to a reduced ohmic contact since it allows the intimate contact between the metal and semiconductor whereas the sample processed by HCl dip only shows a little bit higher resistance due to the discontinuous oxide layer at the metal/semiconductor interface [8]. It should be noted that we have not found any noticeable etching of the contact layer while dipping in $(\text{NH}_4)_2\text{S}$ solution though it is observed that $(\text{NH}_4)_2\text{S}$ -based solution etch *n*- and *p*-GaSb at a steady rate [9].

Thus, we achieved the linear *I-V* characteristics with a contact resistivity as low as $5.1 \times 10^{-6} \Omega \text{ cm}^2$ without any annealing and over a very high current density range like $\pm 70 \text{ kA/cm}^2$ as shown in Fig.2, which is far beyond adequate value for the operation of GaSb-based VCSELs above the threshold current. In addition, a reduction of the contact

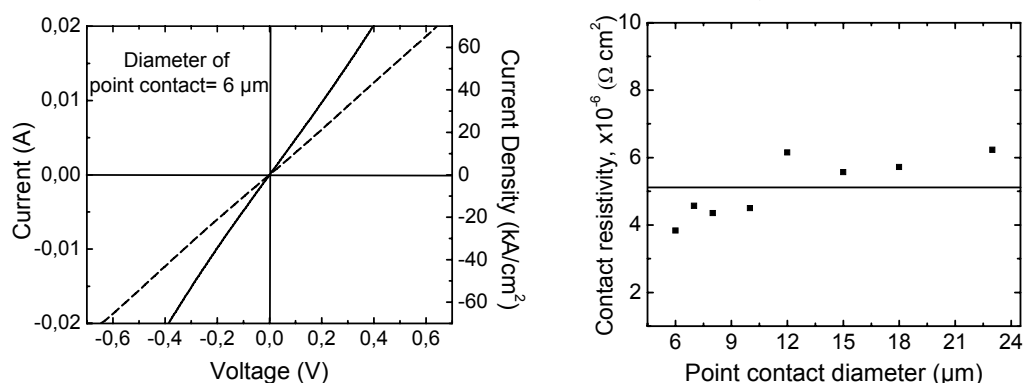


Fig. 2: Current versus voltage (*I-V*) characteristics without annealing for the test structures with contact diameter $6 \mu\text{m}$ (left) where the solid and dashed lines represents the samples processed by HCl dip and sulfide treated both and only HCl dip respectively. The deduced contact resistivity by using the method in ref [10] for different point contact diameters (right).

resistivity is also observed after annealing at 350°C for 90 s which causes no problem for the active region of GaSb-based VCSEL [11].

- [1] C. Lauer et al., IEEE Trans. Instrum. Meas. Vol. 54, pp.1214-1218 (2005).
- [2] A. Bachmann et al., Conference Digest, Proc. of 21st ISLC, pp. 39-40 (2008).
- [3] J. Chen et al. , ESLW, Eindhoven, Netherlands (2008).
- [4] T. Chiu et al., Appl. Phys. Lett., Vol. 56, pp. 1688-1690 (1990).
- [5] Y. Mizokawa, O. Komoda and S. Miyase, Thin Solid Films, Vol. 156, pp. 127-143 (1987).
- [6] C. Lauer, O. Dier and M. C. Amann, Semiconductor Science and Technology, Vol. 21, pp. 1274-1277 (2006).
- [7] J.G. Champlain, R. Magno and J.B. Boos, Electronics Letters, Vol. 43, pp.1315-1317 (2007)
- [8] J.A. Robinson and S.E. Mohny, J. Appl. Phys. Vol. 96, pp. 2684-2688 (2004).
- [9] E. Papis et al., Vacuum Vol. 57 pp.171-178 (2000)
- [10] G. Franz and M. C. Amann, J. Electrochem. Soc., Vol. 140, pp. 847-850 (1993).
- [11] O. Dier et al., Appl. Phys. Lett., Vol. 86, pp.151120 (1-3) (2005).

Single-mode (electro-)thermally tunable GaSb-based VCSEL with Buried Tunnel Junction

Alexander Bachmann¹, Kaveh Kashani-Shirazi, Shamsul Arafin and M.-C. Amann

For gas sensing applications, the mid-infrared wavelength range between 2 and 4 μm is of great interest, as many technologically and environmentally important gases (e.g. CO, CO₂ and NH₃) show strong absorption lines within this spectral region. Recently, tunable diode laser absorption spectroscopy (TDLAS) has been attracting increasing attention due to rapid response times and its contactless measurement, making it superior to conventionally used gas sensors. For the implementation of these systems the development of tunable, single-mode and low-cost laser light sources is a key issue. These requirements are offered by electrically pumped VCSELs. Because of material limitations, the very successful InP-based devices will probably not reach more than 2.3 μm [1]. In contrast, GaSb-based lasers allow the coverage of a large wavelength range well beyond 2 μm .

The schematic device design of the GaSb-based VCSEL is shown in Fig. 1. In a first MBE growth run a 24 pair Te-doped AlAsSb / GaSb distributed Bragg reflector (DBR) is grown on an n -doped (100)-GaSb substrate, yielding a reflectivity of 99.8% at 2.33 μm , followed by the active region made of five 11 nm thick Ga_{0.63}In_{0.37}As_{0.03}Sb_{0.97} quantum wells with 8 nm thick Al_{0.33}Ga_{0.67}As_{0.03}Sb_{0.97} barriers. The following buried tunnel junction (BTJ) permits the substitution of p -type material with its low carrier mobility and its high intra-valence band absorption by better conducting and lower absorbing n -type one. Moreover, by lateral structuring it

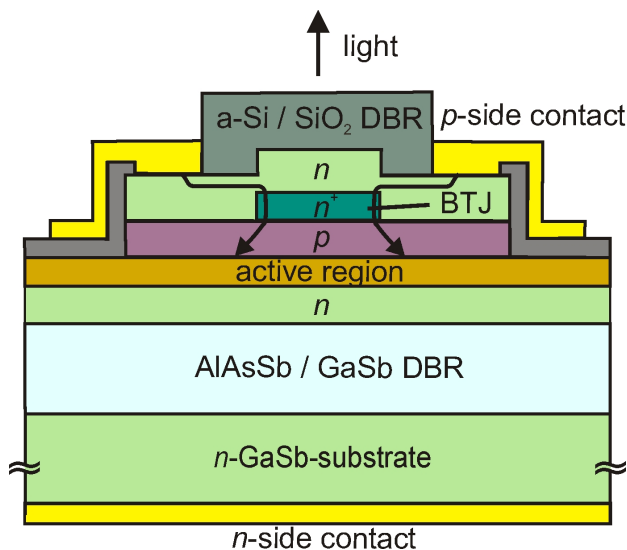


Fig. 1: Schematic structure of GaSb-based BTJ-VCSEL.

serves as efficient current aperture as a highly blocking p^+n -junction is formed on the etched outer surfaces and a low-resistive tunnel-junction remains in the inside. On GaSb-substrate, p^+ -GaSb / n^+ -InAsSb, both doped with Si features a broken band gap alignment making high doping levels unnecessary [2]. Therefore, optical losses by free-carrier absorption can be reduced. After the structuring and an atomic hydrogen cleaning step, the BTJ is overgrown with n -doped GaSb. Mesas are then formed by dry-chemical etching. A low-resistive metal-semiconductor contact without annealing is realized by an n^+ -InAsSb layer and sputtered Ti/Pt/Au [3]. Finally, a dielectric DBR, consisting of 4 pairs of amorphous Si / SiO₂, with a peak reflectivity of 99.7%, is evaporated on top of the structure.

¹phone: +49-89-289-12788, fax: +49-89-320 6620, email: bachmann@wsi.tum.de

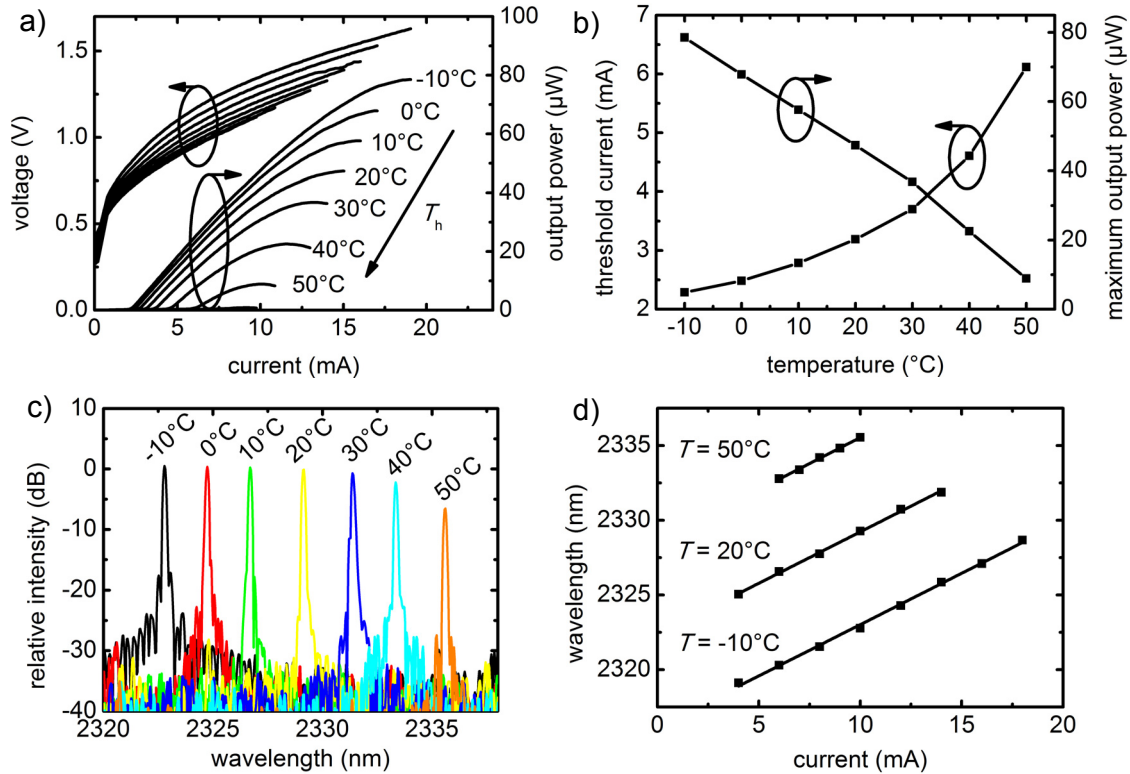


Fig. 2: (a) Temperature dependent P - I characteristics of a GaSb-based BTJ-VCSEL. (b) Threshold current and maximum output power as a function of the heat-sink temperature. (c) Temperature dependent spectra at a constant current of 10 mA. (d) (Electro-)thermal tunability of the emission wavelength.

Fig. 2a shows temperature-dependent P - I curves of a device with an elliptic BTJ area ($3.1 \mu\text{m}$ semi-minor and $5.2 \mu\text{m}$ semi-major axis) in a temperature range from -10°C to 50°C . As can be seen in Fig. 2b the threshold current of this device increases from 2.3 mA to 6.1 mA, corresponding to an effective threshold current density of 2.0 kA cm^{-2} and 5.3 kA cm^{-2} , respectively, assuming a diffusion length of $2 \mu\text{m}$. The minimum threshold current occurs at a temperature below -10°C , indicating significant potential for further improvement with an optimized mode-gain offset. In the temperature range of -10°C to 50°C , the output power decreases from $79 \mu\text{W}$ to $9 \mu\text{W}$. The low differential quantum efficiency of approx. 1.3 % is subject of current investigations. A suboptimal active region design and the gain maximum mismatch are possible explanations.

The spectra of the device are shown in Fig. 2c, yielding single-mode emission. By current-induced self-heating, the VCSELs are continuously tunable in a range of 10 nm at -10°C , yielding a current tunability of 0.69 nm/mA (see Fig. 2d). By changing the heat-sink temperature, a rate of 0.21 nm/K is achieved.

- [1] M. Ortsiefer, G. Boehm, M. Grau, K. Windhorn, E. Roenneberg, J. Roskopf, R. Shau, O. Dier and M.-C. Amann, *Electron. Lett.*, **42**(11), pp. 640-641 (2006).
- [2] O. Dier, C. Lauer and M.-C. Amann, *Electron. Lett.*, **42**(7), pp. 419-420 (2006).
- [3] C. Lauer, O. Dier and M.-C. Amann, *Semicond. Sci. Technol.*, **21**, pp. 1274-1277 (2006).

Calibration-free Carbon Monoxide Sensor without Separate Reference Cell Using 2.3 μm VCSEL

Jia Chen^{1,2,*}, Andreas Hangauer^{1,2}, Rainer Strzoda¹, Markus-Christian Amann²

Due to its toxicity CO affects human health whenever present in ambient air. CO escaping from home burners is the most frequent cause for unintentional death at home with a death toll of annually 500 persons in the USA [1]. Moreover, it is the most prominent gas to be detected for gas sensor based fire detection. The requirements for such sensors are compactness, long term stability, high sensitivity (ppm range) and selectivity. We report on a light-weight and small CO sensor concept with system-inherent wavelength calibration using a reference gas in the measurement optical path. It is based on tunable diode laser absorption spectroscopy (TDLAS) utilizing the unique wide wavelength tuning range via current (> 3 nm) of vertical-cavity surface-emitting lasers (VCSELs). To measure trace gas concentrations with TDLAS, exact knowledge of the scanned absolute spectral wavelength scale is needed. Conventionally, line-locking is used to lock the wavelength position of the laser to the absorption line of interest, using a laser beam splitter and a separate reference cell which contains the target gas in a high concentration [2]. We follow a different approach by including methane (CH_4) in the photodetector housing, i.e. in the optical path of the measurement absorption cell.

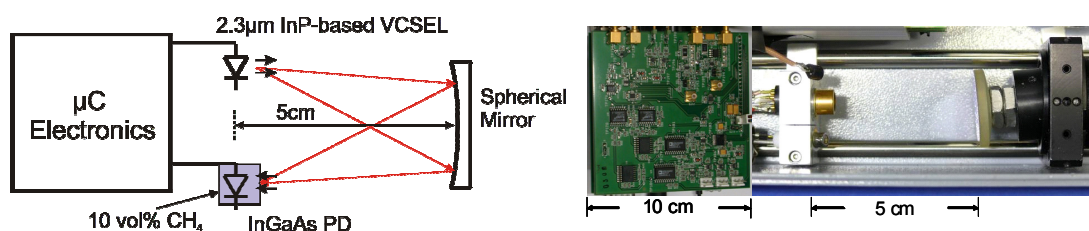


Fig. 1: Design of the CO sensor: A compact absorption cell with 2×5 cm optical path length was used in combination with microprocessor controlled electronics.

In Fig. 1 the compact design of the CO sensor is shown. To accomplish a defined methane absorption of 2.5×10^{-3} , 10 vol% CH_4 is included in the cap of the photodetector forming an optical path of about 0.6 mm. Recently developed 2.3 μm InP-based VCSELs [3,4] with a current tuning coefficient of around 1.2 nm/mA were used in this sensor. A small microcontroller based electronics (10 cm \times 10 cm) serves for the signal processing, control and data evaluation. Only the current of the laser device is tuned. Wavelength modulation spectroscopy (second harmonic detection) [5] is applied to measure the gas absorptions. A wide spectrum scan (Fig. 2 (a)) of about 3 nm every few seconds is used to identify the wavelength scale, while a more frequent narrow scan of 0.7 nm in 0.1 s intervals (Fig. 2 (b)) is performed to determine the CO concentration. In the wide scan, at least three gas absorption lines (either CH_4 and/or CO) are used to determine the linear and quadratic current to wavelength tuning behaviour. In the narrow scan a non-iterative linear least squares curve fit is applied with analytically computed reference spectra of CO and CH_4

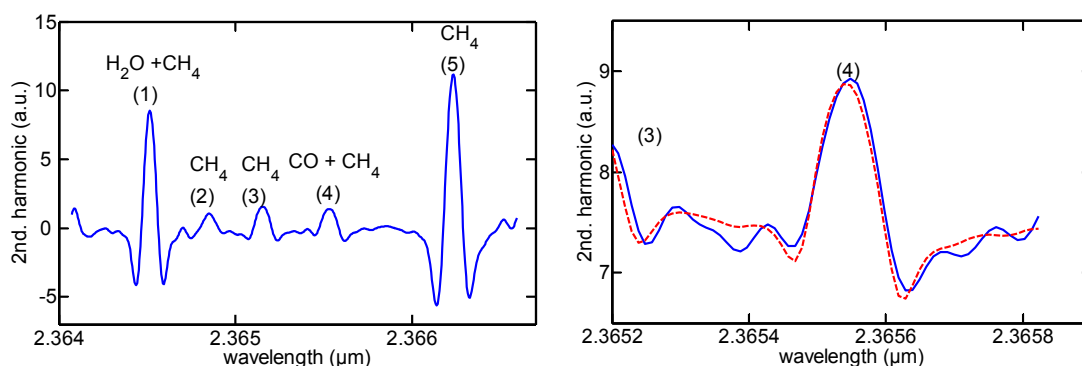
* phone: +49-89-636-40708, email: jia.chen@wsi.tum.de

¹ Corporate Technology, Siemens AG

² Lehrstuhl für Halbleitertechnologie (E26), TU München

absorption lines by using the Lorentz line shape model [6] and the line parameters from the HITRAN database.

The standard deviation of the CO concentration measured with 1 s time resolution is 3.1 ppm. This corresponds to an absorption of 1.1×10^{-5} . Neither background or reference spectra measurements nor further calibration factors except for the line parameters from the HITRAN database and the gain of the second harmonic signal path of the sensor electronics are required. With this method a lifetime stable calibration is within reach. It requires sufficiently wide current-tunable lasers like VCSELs ($\Delta\lambda > 3$ nm). Such performance cannot be achieved by conventional 2.3 μm edge-emitting DFB lasers, because their wavelength tuning range via current is smaller than 2.1 nm. CH₄ can also be detected well in the wide scan with ppm resolution by calibrating the exact absorption of the reference gas in the photodetector. The wide/narrow scan concept is universal and can also be used for sensing of other trace gases like NO, CO₂ using VCSELs at e.g. 1.8 μm or 2.0 μm , respectively.



a) *Wide Scan (Duration: 640 ms, 512 sample points): The wavelength scale is determined by the known wavelength positions of the strong methane lines (1), (5) and the larger line of (3) and (4).*

b) *Narrow Scan (Duration: 100 ms, 64 sample points): current spectrum scan (solid curve) and the analytically computed and fitted reference curve (dashed curve). The CO absorption corresponds to 10 ppm m (100 ppm @ 10 cm).*

Fig. 2: Wavelength scale identification and concentration determination: wide / narrow scan.

-
- [1] Center for Disease Control and Prevention “Carbon Monoxide Poisoning: Fact sheet”, <http://www.cdc.gov/co/pdfs/faqs.htm>
 - [2] M. W. Sigrist et al., “Trace gas monitoring with infrared laser-based detection schemes”, *Appl. Phys. B* 90, 289 (2008)
 - [3] M. Ortsiefer et al., “Electrically pumped room temperature CW VCSELs with 2.3 μm emission wavelength”, *Electron. Lett.*, 42, 640 (2006)
 - [4] A. Hangauer et al. , “Wavelength modulation spectroscopy with a widely tunable InP-based 2.3 μm vertical-cavity surface-emitting laser”, *Optic Lett.*, 33, 1566 (2008)
 - [5] J. Reid and D. Labrie “Second-Harmonic Detection with Tunable Diode Lasers - Comparison of Experiment and Theory”, *Appl. Phys. B* 26, 203 (1981)
 - [6] R. Arndt, “Analytical line shapes for Lorentzian signals broadened by modulation”, *J. Appl. Phys.* 36, 2522 (1965).
-

supported by the Federal Ministry of Education and Research of Germany (Project 'NOSE', No. 13N877) and by the European Union (Project 'NEMIS', No. 031845).

Principles of widely tunable MEMS VCSEL devices based on InP

Tobias Gruendl¹, Christian Grasse, Gerhard Boehm, Ralf Meyer, M.-C. Amann

Nowadays semiconductor laser diodes are more sought-after than ever before. The possibility of realizing many different emission wavelengths, combined with their long term stability and low power consumption offers them broad and worldwide access in many different industrial branches just like data storage, telecommunication and modern lighting concepts. However the big disadvantage of most devices is their strong limitation to only one emission wavelength. A clear breakthrough to this restriction can be achieved by tunable laser diodes offering a device specific tuning range of emission wavelength. This tuning property additionally opens new fields of application just like “Wavelength Division Multiplexing” (WDM) and “Tunable Diode Laser Absorption Spectroscopy” (TDLAS), respectively whereas the last one describes more simply spoken gas sensing efforts. The tuning-mechanism of the VCSEL presented here will be done by an electro-thermal actuation of a membrane on top of the device.

Standard InP VCSEL

The state of the art vertical-cavity surface-emitting Laser (VCSEL) based on InP substrate consists of a *p-i-n*-structure with two highly reflecting mirrors (an epitaxial one on the top and a dielectric one at the bottom) with a mean reflectivity of $> 99\%$ (Fig. 1).

The most important component of the device is the “buried tunnel junction” (BTJ) consisting of a highly doped p^+ and n^+ layer. The BTJ converts electrons into holes before being sent into the active region and serves as current aperture. This aperture is realized by a dry etching process. Its most important parameters are the diameter D and the resulting step height h whereas both have an influence on the multimode behaviour of the VCSEL. As the step is nearly identically represented within the dielectric mirror the BTJ also offers some additional waveguiding effect. By contrast to the further discussed MEMS VCSEL structures the standard InP VCSELs can only be tuned in the range of 10 nm by heating up the active region. This limitation is a clear consequence of the fixed mirrors (epitaxial and dielectric one) on both sides of the device.

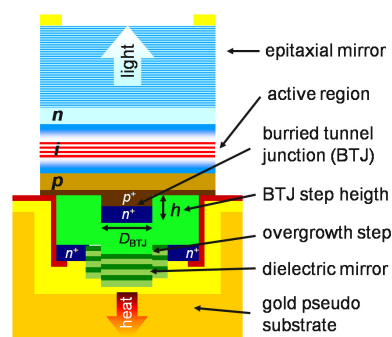


Fig. 1: Basic components of a standard VCSEL based on InP with two fixed mirrors on the top and at the bottom.

Widely Tunable InP MEMS VCSEL

The basic concept of a widely tunable micro-electro-mechanical-system (MEMS) VCSEL is the implementation of a moveable mirror on the top of the laser which is substituting the epitaxial mirror of the standard VCSEL design. The remaining part of the VCSEL is called “half VCSEL” (Fig. 2).

¹phone: +49-89-289-12789, fax: +49-89-3206620, email: gruendl@wsi.tum.de

As both components (top mirror and half VCSEL) are separately produced the material system of the top mirror does not have to be lattice matched to InP. It is mainly grown on GaAs substrates because of thermal aspects and already established process technology. By thermally induced actuation of the external mirror the laser cavity length and as a result the laser wavelength can be changed. Compared to conventional VCSELs with plane mirrors the beam shaping effect by the curved membrane (Fig. 2) offers the opportunity to increase the diameter D_{BTJ} of the BTJ to values of about

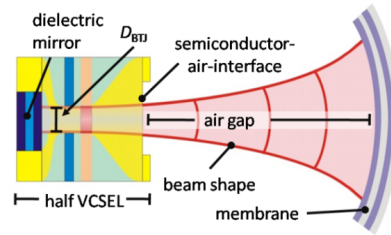


Fig. 2: Basic concept of a tunable VCSEL. The top mirror of the VCSEL is removed and replaced by a moveable membrane (shown here) or cantilever.

20 μm , whereas single mode operation is maintained. Thus the optical output power can be increased. Furthermore the radius of curvature of the membrane and the geometrical dimension of the air gap have a big influence on the modal selection of the MEMS VCSEL. The most fundamental disadvantage of this concept is the unavoidably generated semiconductor-air interface at the top of the half VCSEL (Fig. 2) which is changing the whole device into a 3-mirror device. Because of the non negligible reflectivity at that interface the optical confinement within the semiconductor is very high. This heavily reduces the tuning efficiency and equivalently the free spectral range. While in the formerly developed “extended cavity” (EC) design the decoupling of air gap and half VCSEL has been accomplished by an additional antireflection coating on top of the half VCSEL the new “adapted” design is predominantly based on a detuning of the nodes and antinodes of the optical field with respect to this interface. Based on theoretical calculations and simulations this design offers a tuning range larger than 90 nm, a strongly linear tuning behaviour depending on the optical length of the air gap and a symmetrically shaped gain curve, by contrast to the former design (Fig. 3).

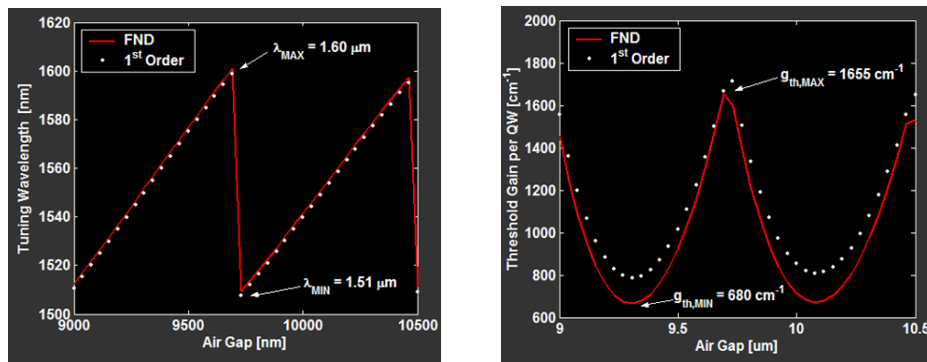


Fig. 3: Simulation results for tuning wavelength (left) and threshold gain (right) of a MEMS VCSEL structure dependent on the air gap length in the new adapted design. Strongly linear tuning behavior (left) and a symmetric gain shape (right) including a strong modal selection are promising theoretical results and a clear improvement of the former EC design.

Planarization of overgrown tunnel junctions for InP-based VCSEL by MOVPE

Christian Grasse¹, M. Müller, G. Böhm, T. Gründl, R. Enzmann, Yan Xu², M. Görblich², R. Meyer, M. Ortsiefer² and M.-C. Amann

InP-based longwavelength vertical cavity surface emitting laser (VCSEL) have emerged to cost effective light sources for telecom applications like wavelength-division-multiplexing, which is mainly due to the benefits of on-wafer testing capability, simple array integration and high fiber coupling efficiency. One important technological challenge of this device was the development of an efficient current aperture, which is needed to reduce the active pumped volume and thereby the threshold current. The implementation of the so called buried tunnel junction (BTJ) solved this problem, but also resulted into a strong index guiding of the whole device, which decreases the device properties. In contrast to the MBE-based deposition technology used so far an MOVPE process offers the opportunity to overcome this drawback by planarizing the BTJ.

In our approach the InP-based VCSEL consists of an MBE grown VCSEL basic structure, which includes an AlGaInAs/AlInAs top DBR, the AlGaInAs-based active region and the tunnel junction. To create a current aperture, mesa structures with a height of around 15 nm and 5 μm in diameter are fabricated using a dry etching process. After a cleaning procedure the patterned sample is then overgrown with silicon doped InP and a thin GaInAs:Si contact layer, which provides a good thermal and electrical conductivity to the gold heatsink shown in Figure 1.

A certain drawback of this concept is the strong index guiding of the optical wave, which is caused by the step profile of the refraction index in the dielectric bottom mirror. This step-like structure has its origin in the surface profil remaining after MBE overgrowth of the BTJ. Due to the higher accessible growth temperatures compared to MBE and therefore higher migration lengths of the atoms at the surface, the MOVPE offers the op-

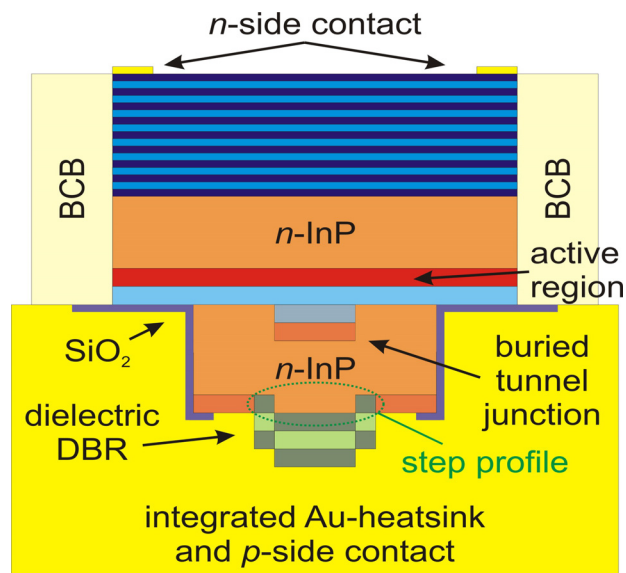


Fig. 1: Illustration of the InP-based VCSEL structure. The top AlGaInAs/AlInAs DBR mirror, active region and tunnel junction are shown. The dotted circle highlights the remaining step profile in the bottom DBR after MBE overgrowth.

¹phone: +49-89-289-12789, fax: +49-89-320 6620, email: grasse@wsi.tum.de

²Vertilas GmbH, c/o Gate Garching, 85748 Garching, Germany

portunity to planarize the step profile during the overgrowth, which decreases the strong index guiding. From this decrease the laser device gains higher side-mode suppression, which enhances the single mode operation, leading in the end to a higher output power. Another advantage of an MOVPE re-growth is the in-situ cleaning of the growth surface due to hydrogen radicals, which are generated during the decomposition of the gaseous precursors. This in-situ cleaning removes remaining oxides and therefore enhances the blocking ratio between the inner and outer part of the BTJ by avoiding trapped induced tunneling.

The InP overgrowth has been carried out with an AIX 200/4 MOVPE system at a temperature of 500°C and 600°C respectively and at a pressure of 150 mbar (H₂ ambient). As precursors TMGa, TMIIn, Phosphine, Arsine and Silan have been used. In-situ thickness control has been performed by using a Laytec EpiTT reflexion measurement setup. Morphology characterization has been carried out with nomarski microscope images, whereas the height profile of the overgrown structures was measured by atomic force microscopy (AFM). Additionally the electrical properties of the overgrown tunnel junctions were studied.

As indicated by figure 2 an almost complete planarization of etched structures after 1.2µm InP overgrowth could be achieved at a growth temperature of 600°C. Although AFM measurements revealed, that the height shape not completely vanishes and also an asymmetric overgrowth kinetic exist, a maximum angle of only 0.2° was detected signifying a good planarization. The measured tunnel junction blocking ratio of around 500 indicates also a superior electrical quality, since MBE overgrown tunnel junctions usually have a blocking ratio around 100. This new technique is therefore a very promising tool for the fabrication of high performance InP-based VCSEL.



Fig. 2: The microscope images illustrate the planarization of the etched structures at 600°C, whereas at 500°C only an elongation in (01-1) direction could be observed

High-Speed Tuning in Vertical-Cavity Surface-Emitting Lasers

Andreas Hangauer¹, Jia Chen, Rainer Strzoda, Markus-Christian Amann²

Compared to edge-emitting lasers VCSELs have a higher FM modulation cut-off frequency in the range of several 10 kHz [1, 4] as well as a higher current tuning coefficient. Furthermore, a slope of approximately $-1/2$ in double logarithmic scale of the FM amplitude response was observed up to 1 MHz [1]. To explain the unique frequency response of the laser FM tuning, physically motivated models exist for DFB lasers as well as VCSELs [2, 3]. The VCSEL model yields an asymptotic slope of $-1/2$ for high frequencies as a result of the model assumption of an infinitely thin active region, which is in agreement with the aforementioned measurement data. Although VCSELs have rather thin structures, a deviation from this “square root” behaviour is expected at high modulation frequencies, which is investigated here. Also at a certain frequency the (weak) free carrier tuning effect should become dominant over the thermal tuning since it has a much higher cutoff frequency.

The FM amplitude measurements were carried out with a Michelson interferometer. The difference in length of both arms was 1 m, which corresponds to an optical frequency resolution of approximately 300 MHz. The FM phase shift was measured utilizing gas absorption lines in ambient air. The position of absorption peaks in one period of the photodetector signal allow for determination of the FM phase shift [4]. Since the gas absorption always occurs at the same wavelength, the position of the absorption peaks in the rising and falling slope of the sine wave can be used to determine the time delay between current excitation and wavelength response. The maximum or minimum of the sinusoidal wavelength variation is exactly in the center between the two absorption peaks. When the position of the maximum or minimum of the current excitation is known, e.g. by simultaneous sampling of laser current and the photodetector signal with an oscilloscope the time delay can be determined. The time delay multiplied with the angular modulation frequency then gives the FM phase shift.

In Fig. 1 it can be seen that the slope of the FM amplitude response for a GaAs-based VCSEL laser gradually changes from $-1/2$ to -1 around $f = 1$ MHz. For the InP-based VCSELs the slope changes from $-1/2$ to slope 0 at $f = 3$ MHz. Furthermore, a significantly higher FM phase shift is observed than it would be expected from minimum phase behaviour determined by the FM amplitude response. In such a minimum phase system asymptotic slopes of 0, $-1/2$ and -1 correspond to phase shifts of 0° , -45° , -90° , respectively.

To understand this behaviour, recall that the overall FM response consists of thermal tuning and free carrier tuning (i.e. the plasma effect). Thermal tuning is dominant at low frequencies but has a lower cut-off frequency. At a certain frequency, the inversely acting plasma effect will become dominant. It is described by the second order system of the laser rate equations, and can be assumed to be constant for $f \ll 100$ MHz. When the plasma effect dominates, a constant FM amplitude with FM phase shift of -180° is expected. Assuming a plasma effect of 7-9 GHz/mA the InP based VCSEL behaviour can be explained. This is in agreement with the chirp observed in high speed InP-VCSEL

¹ phone: +49-89-636-40708, email: andreas.hangauer@wsi.tum.de

² Lehrstuhl für Halbleitertechnologie (E26), TU München, email : mcamann@wsi.tum.de

communications [6]. The GaAs-based laser has an absolutely higher tuning coefficient which may be the reason that no constant tuning coefficient is observed for $f \leq 10$ MHz. However, the plasma effect is indirectly present in the phase shift because it significantly exceeds -90° .

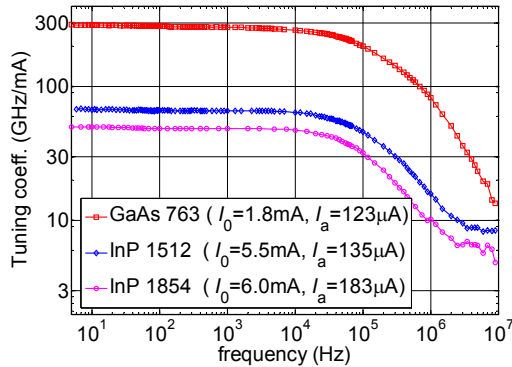


Fig. 1a: Measured FM amplitude response of VCSELs with different emission wavelengths and internal structure (763 nm, GaAs-based, oxide confined [5]; 1512 nm and 1854 nm, InP-based, with buried tunnel junction). I_0 and I_a denote the bias and sinusoidal modulation amplitude, respectively.

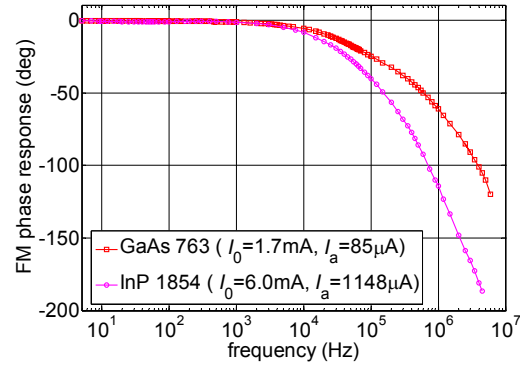


Fig. 1b: FM phase shift measurement. No data for the 1512 nm laser exists because of the lack of a strong gas absorption in ambient air. The phase shift at $f > 1$ MHz is significantly higher than the expected shift of the minimum phase system derived from Fig. 1a.

In summary, our measurements clearly show that the plasma effect in VCSELs has a significant impact on the FM tuning (amplitude and/or phase) starting at frequencies around 1 MHz. The second important result is that the laser FM tuning behaviour can not be modelled as a minimum phase system, i.e. the FM phase response or time step response can not be computed via Hilbert transform methods from only the FM amplitude response.

- [1] J. Chen, A. Hangauer, R. Strzoda, M.-C. Amann, "Experimental characterization of the frequency modulation behavior of vertical cavity surface emitting lasers" Appl. Phys. Lett. **91**, 141105 (2008).
- [2] M.-C. Amann, J. Buus, *Tunable Laser Diodes*, Artech House, Norwood, 1998, Vol. 1, pp. 94-99
- [3] J. Chen, A. Hangauer, M.-C. Amann, "Simplified Model of the Dynamic Thermal Tuning Behavior of VCSELs", Photon. Technol. Lett., **20**, 1082 (2008)
- [4] A. Lytkine, W. Jaeger, J. Tulip, "Long-wavelength VCSELs for applications in absorption spectroscopy: tuning rates and modulation performances", Proc. SPIE, **5737**, 157 (2005)
- [5] M. Grabherr, D. Wiedenmann, R. Jaeger, R. King, "Fabrication and performance of tuneable single-mode VCSELs emitting in the 750- to 1000-nm range", Proc. SPIE, **5737**, 120 (2005)
- [6] W. Hofmann, E. Wong, G. Böhm, M. Ortsiefer, N. H. Zhu, M.-C. Amann, "1.55- μ m VCSEL Arrays for High-Bandwidth WDM-PONs", Photon. Technol. Lett., **20**, 291 (2008)

Quantum transport theory in terahertz quantum cascade lasers

Tillmann Kubis¹, Peter Vogl

The terahertz (THz) spectral region offers a wide range of scientific and commercial applications that require high power and coherent sources within a narrow band. THz quantum cascade lasers (QCL) have proven to be the most promising source to fulfill these requirements. A thorough understanding of the fundamental transport processes is essential to improve the performance of THz-QCLs.

We have developed a parameter-free and quantitative quantum theory of stationary carrier transport and linear optical response in THz-QCLs. Our model is based on a fully self-consistent implementation of the non-equilibrium Green's function (NEGF) theory. Our method takes into account the momentum and energy dependence, and the spatial non-locality of all relevant incoherent scattering mechanisms, i.e. acoustic, polar-optical phonon scattering, charged impurity, Hartree electron-electron, and interface roughness scattering. This guarantees realistic scattering rates as well as accurate state energies, lifetimes, and state occupations.

A typical THz-QCL consists of several hundreds of periodically repeated semiconductor layers. Therefore, it is common to calculate transport in a small number of QCL periods with periodic boundary conditions applied. This method is numerically efficient. However, an unambiguously applied bias per period requires for sufficient energy dissipation and completely coherent transport cannot be described in this way. Instead, we consider charge transport as a scattering problem from source to drain with the QCL as the active device. We assume the two semi-infinite leads to consist of field-free QCL periods that remain in thermal equilibrium. The difference in the chemical potentials of the leads defines the applied bias voltage in the device – irrespective of the nature of transport in the device. The electrons enter the device in propagating eigenstates of the respective infinitely extended

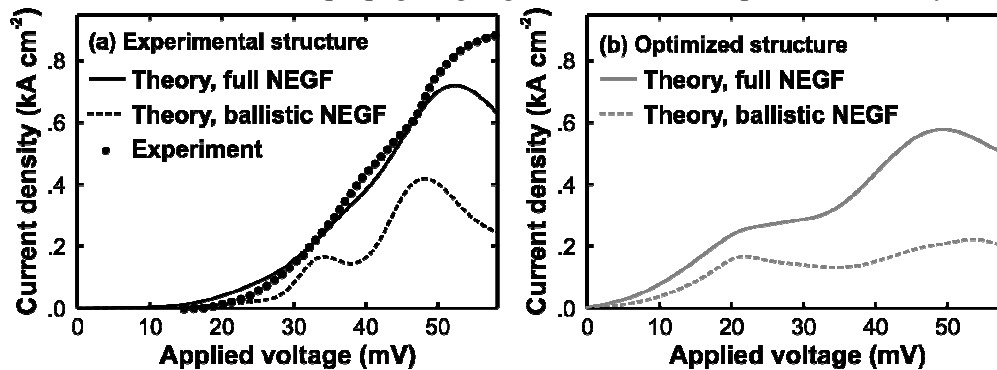


Fig. 1: (a) Experimental (dots) and theoretically predicted (lines) I - V characteristics of the QCL of Ref. [1]. Calculations that include all incoherent scattering mechanisms (solid) agree well with experiment. In contrast, purely coherent transport (dashed) can only partly reproduce the experiment. (b) Predicted I - V characteristics of the optimized QCL described in the text. In contrast to the result in (a), the ballistic current density (dashed) close to threshold at 46 mV is suppressed.

¹phone: +49-89-289-12762, fax: +49-89-289-12737, email: Kubis@wsi.tum.de

lead Hamiltonians. Then, the active device can be restricted to a few QCL periods while the electronic and optical properties are still faithfully mimicked.

We have systematically studied a GaAs/Al_{0.15}Ga_{0.85}As based THz-QCL that has been fabricated recently [1]. The geometry of this structure can be symbolically denoted by (30) 92 (55) 80 (27) 66 (41) 155. All quantities are given in Å, the values in parentheses indicate Al_{0.15}Ga_{0.85}As barrier widths, and the underlined collector well indicates the doped regions of the device. Our results for the I-V-characteristics show excellent agreement with experiment. This is exemplified in Figure 1 (a) that shows the I-V curve of the GaAs/Al_{0.15}Ga_{0.85}As QCL at 40K and compares the present NEGF calculations (solid line) with a strictly ballistic calculation that ignores scattering altogether (dashed) and with experiment (dots, [1]), respectively. A major portion of the total current stems from coherent transport, as can be deduced from the ballistic calculation. In fact, the ballistic current amounts to approximately 60% of the experimental current near the threshold voltage at approximately 46 mV bias per period. We have identified a small overlap of the upper laser level with a resonance of the collector well

to cause the large coherent leakage current. This is illustrated in Fig. 2. It depicts the energy and spatially resolved spectral function $A(z,E)$ of the QCL in Fig. 1 (a) close to threshold for vanishing lateral momentum. The maxima of the spectral function represent resonant states. The dotted line in Fig. 2 shows the spectral function in the center of the QCL at $z = 36$ nm. The two peaks mark the lower ($E = -4$ meV) and the upper ($E = 9$ meV) laser level, respectively. The spectral function in the collector well ($z = 47$ nm) is depicted by the solid line. It shows a resonance at the energy of the lower laser level. In addition, this collector state also overlaps with the upper laser level as can be deduced from the small peak that is marked by the arrow. In spite of being small, this overlap leads to a coherent leakage and reduces the occupation inversion. The simplest way to suppress this leakage is to broaden the collector well since this automatically misaligns the collector well states with the laser levels. The dashed line in Fig. 2 shows the spectral function of the QCL for a collector well width of 173 Å (instead of 155 Å). This modification suppresses the coherent leakage of the upper laser level and reduces the coherent contribution to the threshold current, as can be seen from the small ballistic current density in Fig. 1 (b).

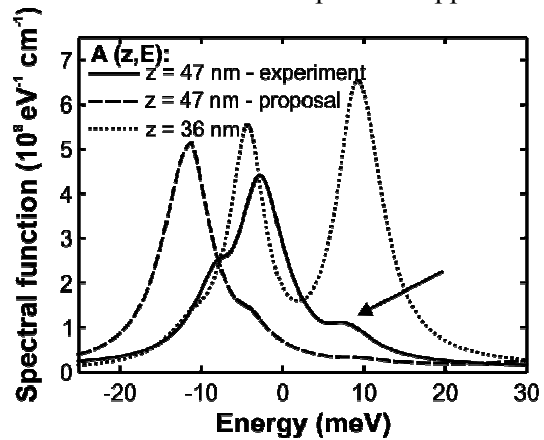


Fig. 2: Spectral function of the QCLs in Fig. 1 as a function of energy E at different device positions. A resonance of the collector well of the experimental QCL (solid) of Fig. 1 (a) overlaps with the upper laser level (dotted, at $E = 10$ meV) in the center of the QCL period (marked by the arrow). In the optimized structure of Fig.1 (b) (dashed), the collector well is broadened to 173 Å and the overlap is suppressed.

- [1] Benz, A., Fasching, G., Andrews, A.M., Martl, M., Unterrainer, K., Roch, T., Schrenk, W., Golka, S., and Strasser, G., Appl. Phys. Lett. **90**, 101107 (2007)

Bioelectronics

Diamond transistors for the recording of cell action potentials

Markus Dankerl¹, Moritz Hauf, Boris Hofmann², Stefan Eick², Sven Ingebrandt², Andreas Offenhäusser², Martin Stutzmann, and Jose A. Garrido

The fundamental understanding of neuronal networks and cell communication as well as medical applications in neuronal prosthesis require the interfacing of living cells with electronic materials. With a transistor array based on diamond, a material with unique advantages for operation in physiological media, we demonstrate the potential of a new material platform for the transduction of cell signals.

To gain insight into neuronal networks, cell semiconductor interfaces have been realized a number of times. However, most of those have been based on conventional silicon technology, which is not especially suited for the operation in electrolytes due to drift and long-term degradation. Diamond, in contrast, has both superior chemically and electrochemically stability and is biocompatible. We made use of these properties to record cell action potentials with a diamond transistor array. The transistor design is based on the p-type surface conductivity exhibited by hydrogen-terminated diamond. The conductivity of a two-dimensional hole gas, which forms spontaneously at the surface of H-terminated diamond, can be controlled by applying a potential versus a reference electrode via the electrolyte. This has been used to fabricate 4x4 arrays of solution-gate field-effect transistors (SGFETs) on undoped, hydrogen-terminated single crystalline diamond (see Fig. 1 a).

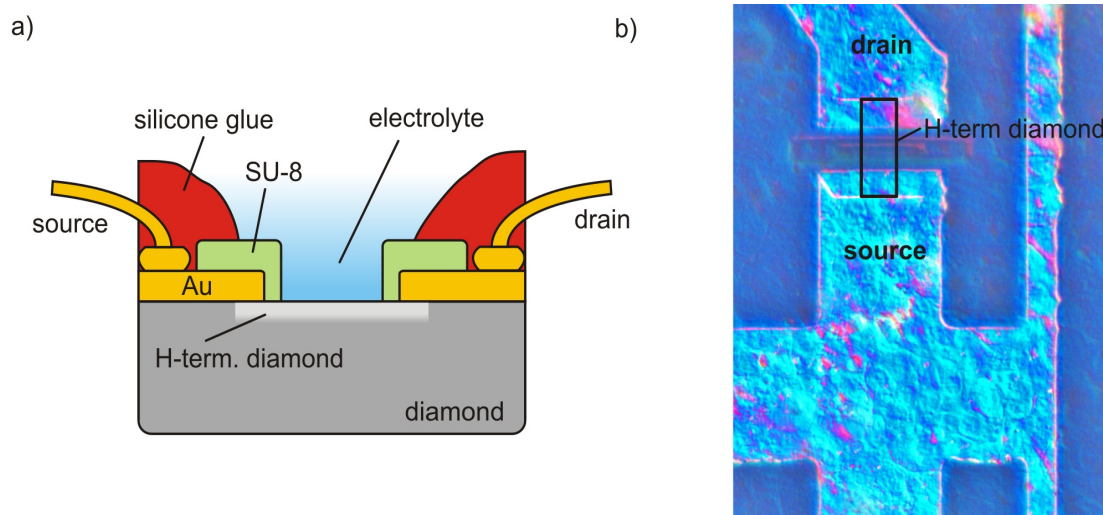


Fig. 1: a) Schematic view of the transistor design, showing the surface conductive H-terminated diamond with the electrolyte as the gate contact, together with the drain and source contacts, as well as the contact passivation (SU-8 and silicone glue). b) Differential interference contrast image of one transistor of the 4x4 array after three days in cell culture. The entire visible area including the transistor gate ($10 \times 20 \mu\text{m}^2$) is covered with a dense layer of HL-1 cardiomyocytes (individual cells cannot be resolved).

¹phone: +49-89-289-12768, email: dankerl@wsi.tum.de

²Institute of Bio- and Nanosystems (IBN-2), Forschungszentrum Jülich GmbH, 52425 Jülich, Germany

The electrical characterization shows that the conductivity can be varied with the gate potential by five orders of magnitude and the devices show sensitivities (dI_{DS}/dU_{GS}) to gate potential changes of around $200 \mu\text{S}$ (at $U_{DS}=0.2\text{V}$ and $U_{GS}=0.22\text{V}$). Furthermore, the SGFETs proved to be stable in electrolyte solution for at least eight days under frequent operation with almost no variation in the conductivity. The noise of the devices with 100 to $400 \mu\text{V}$ (peak to peak) is sufficiently low to detect cell action potentials and the time resolution is adequate (around 3 kHz cut off frequency for 3 dB attenuation) to resolve details of cell signals.

HL-1 cardiomyocytes derived from AT-1 mouse cells (cardiomyocyte tumour) were cultured on these devices for three days. By that time the cells had multiplied enough to form a densely packed layer covering the active areas of the transistors as well as the SU-8 passivated space in between. The growth of the cells demonstrates the good biocompatibility of the surface (see Fig. 1 b). After reaching confluency, the HL-1 cells show spontaneous electrical activity (action potentials). These action potentials could then be detected with the diamond transistors by recording gate potential changes (see Fig. 2). The cells do not directly touch the transistor gate, but are separated from it by a cleft filled with electrolyte. The potential in this cleft, the transductive extracellular potential, constitutes the effective gate potential recorded by the transistor. According to the point-contact model, the transductive extracellular potential, at the point located above the gate, is dependent on the conductance of the current paths. During an action potential the conductance across the membrane changes, as ion channels

open and close, thus making the membrane permeable to sodium and potassium ions. This change in membrane conductance then drives the change in the transductive extracellular potential which is detected by the transistor. The shape of the signal changes depending on the dominance of capacitive and ionic currents across the membrane.

These results confirm the potential of diamond as a suitable platform for bioelectronics.

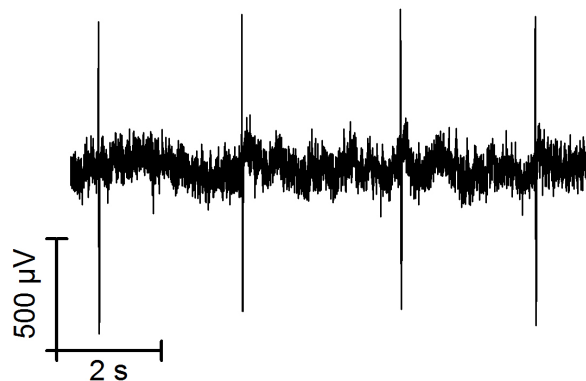


Fig. 2: Recording of the transductive extracellular potential of HL-1 cardiomyocyte cells with a SGFET after three days in cell culture. The spontaneously generated action potentials are clearly visible as spikes in the recorded potential.

PNA Functionalization of Silicon Nanowires for Label-Free DNA Detection and PNA-PEG Modified Silicon Platforms for Applications in DNA Microarrays

Anna Cattani-Scholz*, Daniel Pedone, Florian Blobner, Stefan Neppel, Peter Feulner, Bert Nickel, Luisa Andruzzi, Manish Dubey, Jeffrey Schwartz, Gerhard Abstreiter, Marc Torow

We investigated hydroxyalkylphosphonate self-assembled monolayers as interface systems for the PNA-functionalization of silicon nanowire sensor devices for label-free biosensing applications (Figure 1). AFM and ellipsometric analysis on planar silicon surfaces indicated the presence of an almost complete, dense monolayer on the native oxide with thickness ca. 1 nm. This monolayer comprises alkylphosphonate molecules that are, on average, tilted by about 54° from the surface normal. This finding was further confirmed by X-ray reflection measurements done in aqueous media, which revealed a dense hydrophobic region of about 8 Å thickness (corresponding to a tilt angle 52°) that was separated from an additional layer of enhanced density suggesting coadsorption of ions on top of the SAM. The monolayer effectively passivates the Si surface against electrochemical leakage current into the electrolyte solution through the interface, with maximum currents of the order of 10 pA measured at 200 mV. Functionalization of the phosphonate monolayer with a heterobifunctional maleimido compound was mainly verified by N1s XPS, which indicated a yield of about 35%. The subsequent functionalization with PNA oligonucleotides was verified by XPS, contact angle measurements, and fluorescence spectroscopy following hybridization with dye-labeled DNA. This protocol was translated to 100 nm wide p-doped Si nanowire field effect devices fabricated from SOI (Figure 2), thereby constituting the first successful example of

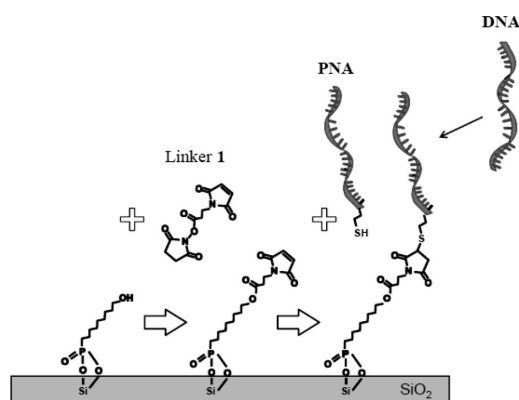


Fig. 1: Schematic illustration of the stepwise functionalization of the SiO₂-terminated Si surface.

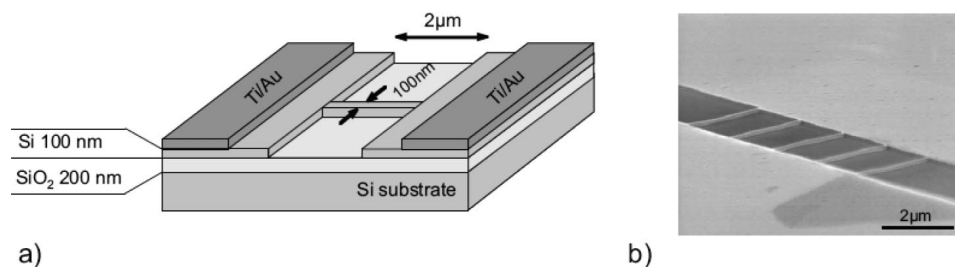


Fig. 2: (a) Schematic of a single silicon nanowire (SiNW) sensing device. (b) SEM micrograph showing a set of five 2 μm long, 100 nm wide (and high), parallel SiNWs.

*phone: +49-89-289-12756, fax: +49-89-320 6620, email: cattani@wsi.tum.de

phosphonate monolayer synthesis and derivatization on a silicon-based, nanoelectronic device. The PNA-functionalized nanowire devices allowed for label-free detection of DNA hybridization. A decrease in wire resistance equivalent to a surface potential change of 1.5 mV was measured upon injection of 1 μ M DNA electrolyte buffer solution¹. This result is in agreement with the expectation for hybridization that results in the surface adsorbing negative charges from the DNA. It should be mentioned, however, that in some experimental runs a signal of nearly comparable magnitude was observed for mismatched DNA. Thus, in contrast to fluorescence measurements, this finding suggests that nonspecific adsorption of DNA onto the organophosphonate monolayer may be significant in label-free sensing experiments. In this context we investigated modification of the organic interfacial layer to effectively reduce these nonspecific interactions. Alkylphosphonate monolayers and carboxyalkylsiloxane films functionalized with dense layers of poly(ethylene glycol) (PEG) and peptide nucleic acid (PNA) probes were prepared and evaluated as biofunctional interfaces with potential applications in DNA microdevices, such as microarrays and

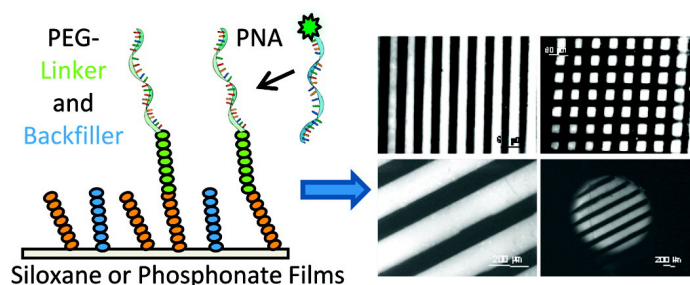


Fig. 3: Left: Schematic of PEG-PNA surface functionalization. Right: Fluorescence image of an array obtained by exposing a PEG-PNA pattern to solution of complementary Cy3-DNA.

biosensors. PEG and PNA were covalently attached to the surfaces of the phosphonate monolayers and the siloxane films via standard *N*-hydroxysuccinimidyl and maleimido reagent-based conjugation chemistries. XPS analysis near the C 1s and N 1s ionization edges confirmed binding of PEG and PNA to these surfaces. Fluorescence hybridization experiments carried out in the presence of complementary and non-complementary DNA showed that PNA-PEG functionalized surfaces were effective for hybridization of cDNA and minimized nonspecific adsorption of the analyte². Spatial patterns prepared by PDMS micromolding showed selective hybridization of fluorescently labeled DNA at PNA-PEG functionalized regions with a dramatic reduction in adsorption to probeless PEG-functionalized regions (Figure 3).

- [1] A. Cattani-Scholz, D. Pedone, M. Dubey, S. Neppl, B. Nickel, P. Feulner, J. Schwartz, G. Abstreiter, M. Tornow, Organophosphonate based PNA-functionalization of silicon nanowires for label-free DNA detection, *ACS Nano* 2, 1653–1660 (2008); *Winner of a 2008 CeNS Publication Award, Center of Nanoscience (CeNS), LMU, Munich; Highlighted “In Nano” (ACS Nano* 2, 1507 (2008));
- [2] A. Cattani-Scholz, D. Pedone, F. Blobner, G. Abstreiter, J. Schwartz, M. Tornow, L. Andruzzi, Novel PNA-PEG Modified Silicon Platforms as Functional Bio-Interfaces for Applications in DNA Microarrays and Biosensors, *Biomacromolecules*, 10 (2009) in press.

Theoretical model for the detection of charged proteins with a silicon-on-insulator sensor

Stefan Birner¹, Peter Vogl

For a bio-sensor device based on a silicon-on-insulator structure, we calculated the sensitivity to specific charge distributions in the electrolyte solution that arise from protein binding to the semiconductor surface [1]. This surface is bio-functionalized with a lipid layer so that proteins can specifically bind to the headgroups of the lipids on the surface. We consider charged, artificial proteins that consist of a variable number of aspartic acids. We calculate self-consistently the spatial charge and electrostatic potential distributions for different ion concentrations in the electrolyte.

We determine the potential change at the binding sites as a function of protein charge and ionic strength. Screening effects in the electrolyte are taken into account using the Poisson-Boltzmann equation which is superior compared to the simplified Debye-Hückel approximation. The quantum mechanical charge densities in the semiconductor are calculated self-consistently by solving the Schrödinger equation in the silicon channel. The Schrödinger and Poisson equations are coupled via the electrostatic potential and the charge densities. Fig. 1(b) shows the calculated conduction band edge and the electron density in the silicon channel for a backgate voltage of $U_{BG} = 25$ V. Indicated is also the position of the Fermi level E_F and the electrostatic potential. Specifying a value for the potential U_G of the reference electrode in the electrolyte is equivalent to a Dirichlet boundary condition for the electrostatic potential of the Poisson-Boltzmann equation. An increase of U_G leads to higher electron densities in the right channel. Therefore, the variation of U_G and the backgate voltage U_{BG} allows one to increase the sensitivity of the sensor by adjusting the ratio of the densities of the two channels. Our calculations

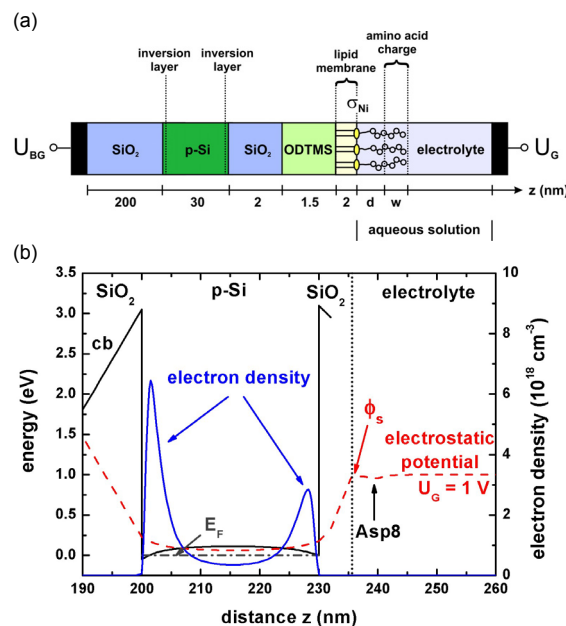


Fig. 1: (a) Schematic layout of the SOI structure. There is a negative interface charge density σ_{Ni} at the lipid/electrolyte interface. The amino acid charge is assumed to be distributed homogeneously over a width w . The electrolyte region includes the histidine-tagged amino acids as well as the neutral part of the tag of length d . (b) Calculated conduction band edge (black solid line) and electrostatic potential (dashed line) at a salt concentration of 50 mM KCl. The electron charge density (blue solid line) of the two inversion layers is shown. Upon binding to the lipid membrane, the charge of the aspartic acid (Asp8) modifies the surface potential ϕ_s . The interface between the lipid membrane and the electrolyte is indicated by the vertical dotted line.

¹phone: +49-89-289-12752, fax: +49-89-289-12737, email: stefan.birner@nextnano.de

yield channel densities of the order of a few 10^{12} cm^{-2} . They are modulated slightly by the actual configuration of the system in terms of ion concentrations and protein charges. Since a lower surface potential ϕ_s yields a lower electron density in the inverted silicon channel, the source-drain current is expected to decrease if negatively charged proteins bind to the functionalized sensor surface.

The artificial proteins that we consider consist of several aspartic acids. Figure 2(a) shows the calculated potential distributions for a varying number of aspartic acids, i.e. various protein charge distributions, at 50 mM KCl concentration in the electrolyte solution. The magnitude of the negative protein charge density increases with the number of aspartic acids. This results in a lower electrostatic potential in the protein region. Also, the surface potential ϕ_s decreases with increasing protein charge. Fig. 2(b) shows the calculated change of surface potential $\Delta\phi_s$ at the bio-functionalized semiconductor surface for a varying number of aspartic acids at salt concentrations of 50 and 140 mM KCl. Comparison with experiment is very good. One can clearly see that the sensitivity of the structure is enhanced at low ion concentrations. We demonstrated that our numerical approach - the self-consistent solution of the Schrödinger and Poisson-Boltzmann equation [3] - is well suited to model semiconductor based bio-sensors in a systematic manner, which is a requirement in order to both understand and optimize their sensitivity.

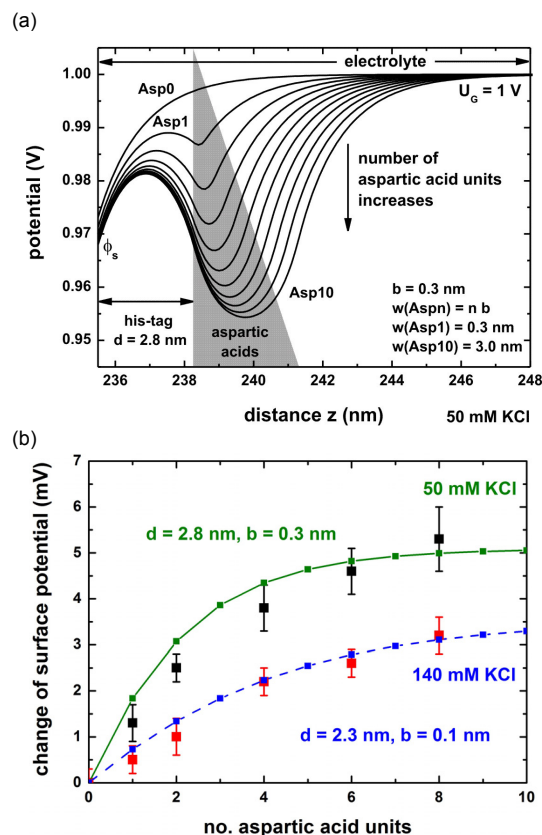


Fig. 2: (a) Calculated electrostatic potential distributions for varying protein charge at 50 mM KCl. The number of aspartic acids is $n = 0, 1, 2, \dots, 10$ and increases from top to bottom. The width $w = nb$ of the negative protein charge distribution is assumed to increase linearly with the number of acids (indicated schematically by the shaded triangle). (b) Calculated surface potential change $\Delta\phi_s$ at the lipid membrane as a function of the number of aspartic acids in the artificial protein for different salt concentrations (solid line: 50 mM KCl, dashed line: 140 mM KCl). The experimental data points are from Ref. [2].

- [1] S. Birner, C. Uhl, M. Bayer, P. Vogl, J. Phys.: Conf. Ser. **107**, 012002 (2008)
- [2] S.Q. Lud, M.G. Nikolaidis, I. Haase I, M. Fischer, A.R. Bausch, ChemPhysChem **7**, 379 (2006)
- [3] This algorithm has been implemented into the software package nextnano³ which can be obtained from www.nextnano.de.

A micron-sized nanoporous multifunction sensing device

L. Moreno i Codinachs¹, C. Birkenstock, T. Garma, R. Zierold, J. Bachmann, K. Nielsch², M. J. Schöning^{3,4}, and A. Fontcuberta i Morral

A capacitive sensor based on Anodic Aluminium Oxide (AAO) porous structures has been developed. In some cases, the pores have been also conformally coated with a high chemical pure SiO₂ by means of Atomic Layer Deposition (ALD). Temperature measurements have been done in DI water obtaining a response of 0.2 nF/°C. pH measurements have been performed and the responses obtained are between 0.2 and 1 nF/pH. The reproducibility of the sensors has been found to be high and a larger hysteresis effect has been observed in the samples with alumina pores rather than in the SiO₂ ones. The hysteresis seems to be related to the charging of the oxide upon application of a voltage.

The most common approach to develop sensors in the nanoscale is the use of ordered structures such as nanowires or carbon nanotubes [1]. Very often such regular arrays have been obtained by synthesizing the wires inside templates such as Anodic Aluminium Oxide (AAO) [2]. In this work vertically oriented AAO pores have been used [3] even there is the possibility to orientate them horizontally [4]. By means of Atomic Layer Deposition (ALD) technique, the alumina pores can be conformally coated with several materials, basically oxides [5]. Hence, small diameter pores with different materials can be obtained giving the chance to functionalize the surface to fabricate sensors sensitive to different biological or chemical species.

Temperature and pH measurements have been performed using capacitive sensors based on different AAO pore membrane structures coated in some cases with SiO₂ using the ALD technique. The sensing principle of the device is the measurement of the capacity of two metal plates (Al in one side and the solution and an Au electrode in the other) in which in between a porous dielectric layer (the aluminium oxide coated or not with the SiO₂) is located (Figure 1).

Capacitance measurements have been performed using two different devices: a RCL meter and a potentiostat in order to study and minimize the possible charging effects of the oxides and therefore to compare hysteresis and stability effects.

Temperature measurements have been performed in DI-water. The capacitance increases linearly with the temperature and a high reproducibility of the device is observed. The calculations indicate that the capacity of the sensor should decrease approximately by 15%, when the temperature is varied from 20 to 90 °C (neglecting an Electrical Double Layer (EDL) capacity). However, we obtain a linear increase from about 90%. Possible reasons for this increase are the changes on the alumina surface as well as that the EDL capacity may increase with temperature.

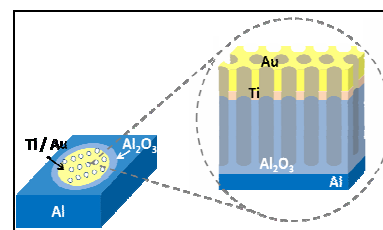


Fig. 1: Scheme of the fabricated samples (left top view, right cross section).

¹phone: +49-89-289-13884, fax: +49-89-320 6620, email: moreno@wsi.tum.de

²Institute of Applied Physics, University of Hamburg

³Aachen University of Applied Sciences, Jülich, Institute of Nano- and Biotechnologies (INB)

⁴Research Centre Jülich GmbH, Institute of Bio- and Nanosystems (IBN-2)

pH measurements have been realized with samples with either Al_2O_3 pores or Al_2O_3 pores coated with 20 nm SiO_2 , in order to check the stability in different pH environments of both materials as well as the capacity-pH response. The capacitance increases linearly with the pH value in both cases (0,2 and 0,6nF/pH for the RCL meter and the potentiostat respectively). We also observe an hysteresis effect (less than 2 nF). We attribute this to the porosity of the alumina, which may be more prone to store charges. The reproducibility of the device, from Fig. 2a, can be observed as quite high. The limit of detection (LOD) of the sensor varies a little (in case of the measurements done with the potentiostat (applied voltage= 0 V), the limit of detection is around pH 4–5, while in the other measurements with the RLC meter (applied voltage= 2 V), the device is able to respond at pH of around 3. Finally, the relative errors of the measurements (calculated using two replicates performed for each measurement) are 0.13% for the RCL meter and 0.19% for the potentiostat.

In order to reduce the hysteresis effect, we conformally coated the alumina with a high quality SiO_2 . In Fig. 2b, the results of the pH calibrations done with samples in which the alumina pores have been coated with 20 nm of SiO_2 are shown. In this case, there is also a linear C-pH response observed (0,3 and 0,9nF/pH for the RCL meter and the potentiostat respectively). The hysteresis decreases with time, probably due to the storage of the charges on the oxide after the application of the voltage (2 V). Interestingly, after three cycles, the hysteresis disappears. This can be explained due to the much lower porosity of the SiO_2 and the high chemical purity of this material. In this case, the LOD of the sensor is also around pH 3 and the relative error is considerably smaller in comparison with the porous alumina ones ($1.8 \times 10^{-3}\%$ and $3.4 \times 10^{-3}\%$ for the RCL meter and the potentiostat devices, respectively). This can be also attributed to the high stability of this material.

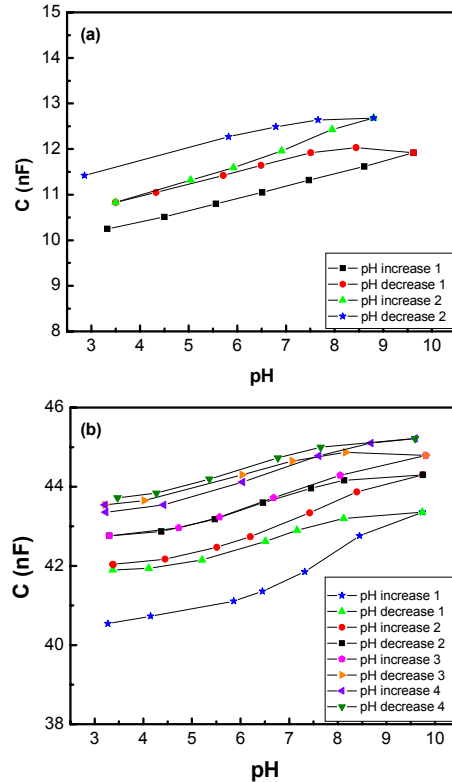


Fig. 2: C-pH curves obtained with a RCL meter for (a) an Al_2O_3 pore sample and (b) a sample of Al_2O_3 pore coated with 20 nm SiO_2 .

- [1] F. Patolsky, G. Zheng, and C. M. Lieber, *Anal. Chem.* **78**, 4260 (2006)
- [2] J. Sarkar, G. G. Khan, and A. Basumallick, *Bull. Mater. Sci.* **30**, 271 (2007)
- [3] Y. Xiang, W. Lee, K. Nielsch, G. Abstreiter, and A. Fontcuberta i Morral, *Phys. Status Solidi RRL* **2**, 59 (2008)
- [4] L. Moreno i Codinachs¹, C. Birkenstock, T. Garma, R. Zierold, J. Bachmann, K. Nielsch², M. J. Schöning^{3,4}, and A. Fontcuberta i Morral, *Phys. Status Solidi A*, 1-7 (2009)
- [5] M. Knez, K. Nielsch, and L. Niinisto, *Adv. Mater.* **19**, 3425 (2007)

Alkylation of Silicon Carbide

Marco Hoeb¹, Ian D. Sharp, Carlos A. Diaz Alvarez, Martin Stutzmann, and Martin S. Brandt

One basic requirement for semiconductor biosensors based on hybrid structures is the covalent attachment of functional organic layers to the semiconductor surface. Former studies have shown that etching of silicon carbide (SiC) in hydrofluoric acid (HF) leads to surface hydroxylation [1] and thereby provides an ideal surface termination for the reaction with silanes [2]. We also investigated the thermally activated attachment of alkenes to the SiC surface. In the case of silicon, a commonly known reaction route for direct attachment of alkanes is the so-called hydrosilylation. In principle, this functionalization proceeds via a radical chain reaction process leading to a chemically grafted alkyl monolayer, but starting from a hydrogen-terminated surface. Interestingly, we find that this process also works on hydroxylated SiC surfaces.

Here we describe the formation of octadecyl monolayers on Si- and C-face n-type 6H-SiC. For this study the samples were immersed in neat 1-octadecene at 200°C under Argon. Atomic force microscopy (AFM) measurements of alkylated SiC surfaces, such as

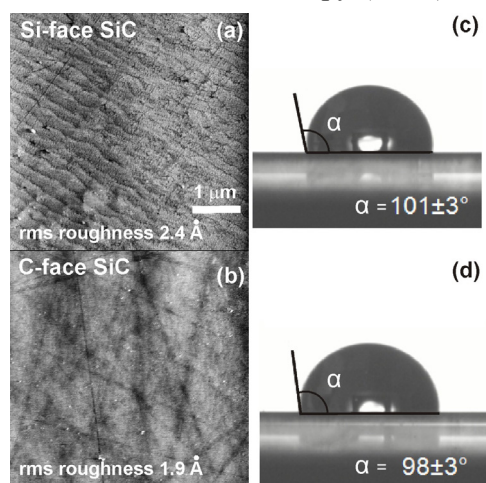


Fig. 1: (a) and (b) AFM images of alkylated SiC surfaces, shown for both polar surfaces. (c) and (d) show the corresponding contact angles with water.

those shown in Fig. 1 (a) and (b), reveal smooth and homogeneous surfaces with no evidence of clustering or pinholes. In Fig. 1(a) even steps of Si-C bilayers can be resolved after the alkylation. As typical for this surface, the C-face shows shallow residual scratches arising from the chemomechanical polishing, which slightly fade after reaction with 1-octadecene. Together with spectra from X-ray photoelectron spectroscopy (not shown), we conclude that an organic monolayer is formed. As shown in Fig. 1 (c) and (d), contact angle measurements on both faces of alkyl-functionalized 6H-SiC reveal the hydrophobic behavior char-

acteristic of densely packed monolayers containing the terminal CH₃ molecular endgroups of 1-octadecene, whose molecular structure is schematically depicted in the inset of Fig. 2. Thermal desorption spectroscopy (TDS) measurements (also not shown) performed after functionalization reveal monolayer stability up to 730 K, thus confirming chemisorption rather than physisorption of the molecules.

¹phone: +49-89-289-12755, fax: +49-89-289 12737, email: hoeb@wsi.tum.de

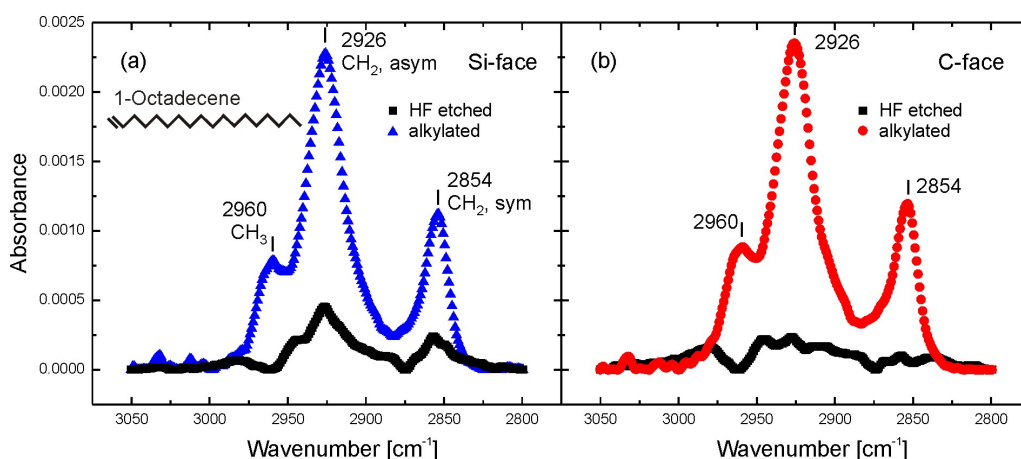


Fig. 2: ATR-FTIR spectrum of alkylated Si- and C-face SiC before and after monolayer formation. Clear CH_x vibrational modes after alkylation proof successful formation of the octadecyl monolayer on both polar surfaces. All spectra are corrected for the same contact with the ATR crystal.

Unpolarized attenuated total reflection Fourier transform infrared (ATR-FTIR) measurements give further insight into the surface chemistry of the organic layers. Figure 2 compares spectra obtained on the Si- and C-face of 6H-SiC before and after functionalization using the clean Germanium ATR crystal as the background reference. After HF etching the, spectral region of the CH_x vibrational modes shows some contamination with environmental hydrocarbons, especially on the Si-face. Following alkylation we observe a clear hydrocarbon signature on both surfaces with strong absorption lines at 2960 cm^{-1} , 2926 cm^{-1} , and 2854 cm^{-1} , corresponding to asymmetric CH_3 , asymmetric CH_2 , and symmetric CH_2 vibrational modes, respectively. These results corroborate the successful attachment of alkenes to the surface.

In conclusion, we have demonstrated wet-chemical functionalization of initially OH-terminated 6H-SiC surfaces via alkylation reactions. AFM and TDS prove that the functional layers are smooth and covalently bound to the substrate. XPS and ATR-FTIR measurements confirm that alkene molecules thermally react with terminal hydroxyl sites.

- [1] U. Starke, Ch. Bram, P.-R. Steiner, W. Hartner, L. Hammer, K. Heinz, and K. Müller, *Appl. Surf. Sci.* **89**, 175 (1995)
- [2] S.J. Schoell, M. Hoeb, I.D. Sharp, W. Steins, M. Eickhoff, M. Stutzmann, and M.S. Brandt, *Appl. Phys. Lett.* **92**, 153301 (2008)

Electrochemical scanning tunneling microscopy for nanoscale studies at the solid/liquid interface

Simon Q. Lud¹, Philipp S. Koch, Martin Stutzmann, and Jose A. Garrido

The study of electron transfer phenomena in molecules and biomolecules immobilized onto solid electrodes represents a challenging and important task since it is fundamental for all kinds of electronic transport between inorganic and biological systems. These so-called hybrid systems could serve as basic elements for research in different fields such as biosensors, bioorganic solar cells, and biomolecular electronics. We propose the study of metalloproteins immobilized onto functionalized ultrananocrystalline diamond solid supports as a model system. Scanning tunneling microscopy techniques operating under electrochemical control (EC-STM) enable to perform these investigations at the level of a single protein (see Fig. 1). A dedicated scanning probe microscope for nanoscale studies at the solid-liquid interface, specifically in biological electrolyte environments, has been setup at the Walter Schottky Institut. Using a bipotentiostat, the potential of the investigated sample versus the reference electrode and the potential of the tip versus the reference electrode can be independently controlled. The calibration of the X/Y/Z piezo scanner operated in electrolyte environment has been performed using highly oriented pyroelectric

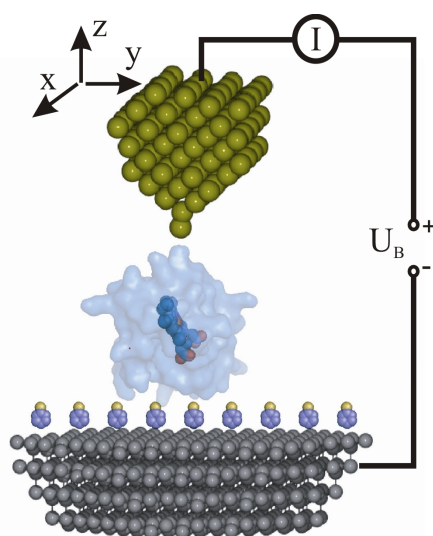


Fig. 1: Representation of the EC-STM system investigating an immobilized protein on a functionalized diamond surface.

graphite (HOPG). Figure 2 shows an electrochemical nanoscale image of HOPG recorded under potentiostatic control, revealing the expected hexagonally close-packed carbon atomic lattice. This result confirms the capability of the set-up to achieve atomic resolution in an electrolyte environment.

As a solid support for the biomolecules we use diamond thin films. Diamond is considered an excellent electrode material for electrochemistry, with very low background current and the largest electrochemical potential window of all solids. Especially, ultrananocrystalline diamond (UNCD) with its low production cost and scalability to large area deposition has received much attention for both biosensing applications and electron transfer investigations. However, the electronic properties of UNCD films are not fully understood yet. It has been proposed that the reported metallic transport in these films is induced by electron transport in the grain boundaries containing sp^2 . To address this issue, we have performed scanning tunneling spectroscopy in order to verify the presence of the dominant sp^2 phase. In these experiments, the tip is held at a fixed distance from the surface and the tunneling current is recorded while varying the bias potential. The local density of states of the surface is then proportional to the differential conductivity, dI/dU . Fig-

¹phone: +49-89-289-12768, fax: +49-89-320 6620, email: lud@wsi.tum.de

ure 3a shows the differential conductivity of an oxidized metal-like UNCD surface: no band gap is observed, as expected for diamond, but a characteristic V-shape of sp^2 materials.

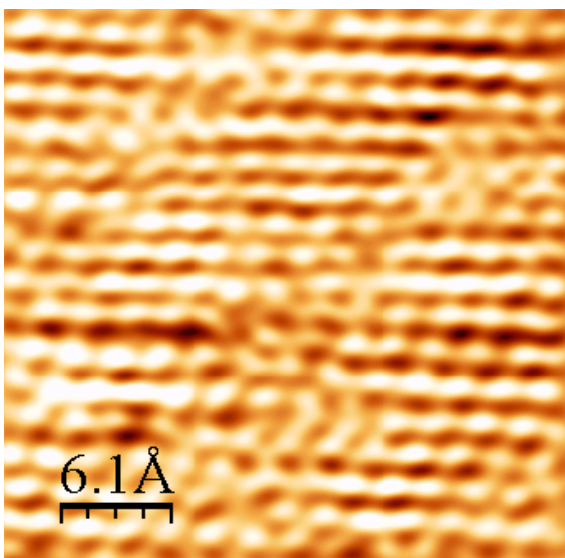


Fig. 2: Nanoscale image of HOPG recorded in electrolyte under potentiostatic control revealing atomic resolution.

Furthermore we aimed at the nanoscale imaging and structural characterization of the UNCD thin films under potentiostatic control in electrolyte. Figure 3b shows a nanoscale electrochemical image of a UNCD film. The image shows a very smooth surface with fine grained structures of the order of 3 nm, in good agreement with the expected grain size (≈ 5 nm).

These results confirm the suitability of UNCD thin films for the study of charge transfer between immobilized biomolecules and carbon-based solid supports. We expect this approach to yield high resolution STM images of immobilized metalloproteins.

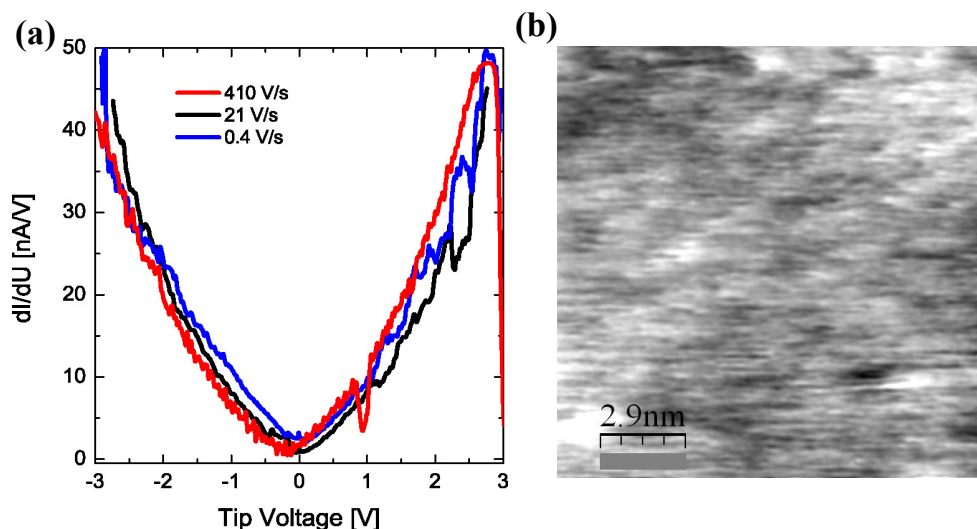


Fig. 3: (a) Scanning tunneling spectroscopy: differential conductivity dI/dU graph showing experiments performed with different scan rates. The absence of a clear band-gap and the V-shape of the curves confirm the dominant transport in an sp^2 phase. (b) EC-STM image of a hydrogenated UNCD surface recorded in electrolyte, revealing structural features of size corresponding to the grain dimensions of UNCD. The gray level scale in (b) corresponds to 2.5 \AA of vertical distance.

3. Research Funding and Collaborations

Many of our research projects have benefited from very fruitful collaborations with external groups either via joint projects, individual collaborations, exchange programs, or through direct interaction with visitors. The major external collaborations are based on joint projects which are financially supported by different organizations. The total amount of external funding exceeded 3 Mio € in 2008.

External Funding

1. Bundesministerium für Bildung und Forschung (BMBF)

- Kompetenzzentrum Nanop: „Anwendung von Nanostrukturen in der Optoelektronik“
- NOSE (Nanotechnologie für die optische Spektroskopie)
- nanoQuit: „Gekoppelte Quantenpunkttransistoren in präziser Kettenanordnung“, „AIAs Nanostrukturen als quantengekoppelte Systeme“, „Entwicklung von quantenpunktbasierenden Einzelphotonenquellen für Emissionswellenlängen um 1,55 μm “
- Verbundvorhaben: EPR-Solar – „Ortsaufgelöste elektrisch detektierte magnetische Resonanz“

Bundesministerium für Umwelt, Naturschutz und Reaktorsicherheit (BMU)

- Kristalline Silizium-Legierungen für Dünnschicht-Solarzellen

2. Deutsche Forschungsgemeinschaft (DFG)

- Sonderforschungsbereich “Festkörperbasierte Quanteninformationsverarbeitung” (SFB 631)
- Schwerpunktprogramm „Quanten-Hall-Systeme“
- Forschungsk Kooperation „FORMEDIAN“
- BR 1585/5-1: „Quantum properties of dopants for silicon nanospintronics“
- DFG GA 1432/1-1: „Functionalization of diamond surfaces for biosensor applications“
- EI 518/2-1: ERA NANOSCI: Nanowire arrays for multifunctional chemical sensors”
- GA 1432/1-1: “Functionalization of diamond surfaces for biosensors applications”
- GR 2618/1-1: „Bent quantum Hall effect“
- HO 3324//2-1 „Quantum transport at the molecular scale”
- HO 3324/2-2 “Molecular circuits for optoelectronics utilizing carbon nanotubes”
- HO 3324/4-1 „Optoelectronic detection of non-equilibrium spin transport in the mesoscopic regime in semiconductor nanostructures”
- VO 483/5-1: „Microscopic theory of spin-splittings and ballistic spin currents in semiconductor“

3. Excellence Initiative of Federal and State Governments

- Cluster of Excellence „Nanosystems Initiative Munich“ (NIM, 7 projects)
- TUM International Graduate School of Science and Engineering (IGSSE)
- TUM Institute for Advanced Study (IAS)
- TUM “Towards bionic solar cells”

4. **Bayerisch-Kalifornisches Hochschulzentrum - BaCaTeC**
 - “High-speed Data-Com-Lasers (VCSELs) for injection locking experiments”
5. **DAAD**
 - Partnerschaften mit Japan und Korea
6. **Elitenetzwerk Bayern**
 - Int. Graduate School “Materials Science of Complex Interfaces (CompInt)”
7. **European Union**
 - COLLECT (Collective electronic states in nanostructures)
 - DOTSENSE (Group III-nitride quantum dots as optical transducers for chemical sensor)
 - DREAMS (Diamond to Retina Artificial Micro-interface Structures)
 - DRIVE (Diamond Research on Interfaces for Versatile Electronics)
 - GANANO (New Generation of GaN-based sensor arrays for nano- and pico-fluidic systems for fast and reliable biomedical testing)
 - NEMIS (New Mid-Infrared Sensors)
 - PSY-NANO-Si: Nanosilicon-based photosynthesis for chemical and biomedical applications
 - Marie Curie Excellence Grant: SENFED (Semiconductor Nanowires and their Field Effect Devices) EXT-CT-2006-042721
 - SUBTUNE (Widely Tunable VCSEL using sub wavelength gratings)
8. **Industry**
 - Evonik Degussa AG Düsseldorf, Germany:
 - „Funktionsschichten aus Silizium-Nanopartikeln“
 - „Silizium-Nanopartikel für Hybride Solarzellen“
 - „Lumineszierende Silizium-Nanopartikel für Smart Label Anwendungen“
 - Fujitsu Laboratories of Europe Ltd., Hayes Park, UK:
 - “DNA on gold for biosensors”
 - “Nanogap Devices”
 - Rhode & Schwarz, München, Germany: „Zero-Bias Schottky-Diodes“
 - Siemens AG, München: „Defekte in CdTe“
 - Siemens AG, Erlangen: „Electrodes for thermionic converter“
 - Vertilas, Garching, Germany: „Langwellige VCSEL“
9. **FWF - Fonds zur Förderung der wissenschaftlichen Forschung, Wien, Austria**
 - SFB F025 „InfraRed optical nanostructures“

International collaborations

Partner	Institution	Subject
Jocelyn Achard	Centre National de la Recherche Scientifique, Paris, France	High purity single crystalline diamond substrates
Yasuhiko Arakawa	University of Tokyo, Japan	Optical spectroscopy of quantum dots
Günther Bauer	Universität Linz, Austria	Optical properties of quantum dot lattices X-ray analysis of quantum dots
Philippe Bergonzo, Milos Nesladek	Commissariat à l'Énergie Atomique, Saclay, France	Neurons on diamond surfaces
Tim Boykin	University of Utah, USA	Tight binding methods
Mark Brongersma	Stanford University, USA	Synthesis of germanium nanowires
Etienne Bustarret	Centre National de la Recherche Scientifique, Grenoble, France	Low temperature electronic transport in diamond, III-nitrides on diamond
Jens Buus	Gayton Photonics, Gayton, UK	Tunable lasers
Fernando Calle	Universidad Politécnica de Madrid, Madrid, Spain	AlGaIn/GaN electrolyte gate FETs, GaN MEMS and NEMS
Itai Carmeli	Dep. of Physical Chemistry and Center for Nanoscience Tel-Aviv University, Israel	Optoelectronics with photosynthetic reaction center (PSI)
Yves Chabal	Rutgers University, Piscataway, USA	FTIR studies of hydrogen-induced exfoliation of Ge
Connie Chang-Hasnain	University of California, Berkeley, USA	Subwavelength gratings, long-wavelength VCSELs
Lukas Chrostowski	University of British Columbia, Vancouver, Canada	High-speed injection-locking
Anthony G. Cullis	University of Sheffield, Sheffield, UK	TEM microscopy
Klaus Ensslin	ETH Zürich, Switzerland	Transport through quantum dots
Lars Frandsen / Jørn Hvam	DTU Copenhagen, Denmark	Fabrication of SOI photonic crystal nanostructures
Stephen Goodnick	Arizona State University, Phoenix, USA	Applications of novel density functional methods
Dieter M. Gruen	Argonne National Laboratory, USA	Ultrananocrystalline diamond thin films
Ken Haenen	Interuniversitair Micro-Electronica Centrum, Hasselt, Belgium	Nanocrystalline diamond growth
Eugene E. Haller	University of California, Berkeley, USA	Isotopical engineering of Si and Ge

Robert Hamers	University of Wisconsin, Wisconsin, USA	Diamond biosensors
Ulrich Höhenester	Universität Graz, Austria	Theory of exciton phonon interaction in single dot-nanocavities
Qing Hu	Massachusetts Institute of Technology, Boston, USA	Quantum cascade lasers
Eduard Hulicius	Institute of Physics, Czech Academy of Sciences, Prague, Czech Republic	Antimonide VCSELs
Kohei M. Itoh	Keio University, Yokohama, Japan	Isotopical engineering of Si and Ge
Richard Jackman	University of College London, London, UK	Diamond biosensors
Stacia Keller/ Umesh Mishra	University of California Santa Barbara, USA	III-nitride bioelectronics
Paul Koenraad	Technical University of Eindhoven, The Netherlands	Scanning tunnelling microscopy of coupled quantum dot nanostructures
Philomela Komninou	Aristotle University of Thessaloniki, Greece	DOTSENSE
Wolfgang Langbein	University of Cardiff, UK	Ultrafast FWM spectroscopy of nanostructures
Anders Larsson	Chalmers University, Gothenburg, Sweden	Modelling of VCSELs
Karin Larsson	University of Uppsala, Uppsala, Sweden	DFT calculations: water on diamond
Steve Laux	IBM, Yorktown Heights, USA	Quantum transport
Kwan H. Lee	University of Oxford, UK	Simulation of nitride based nanorods and quantum dots
Anita Lloyd Spetz	Linköping University, Linköping, Sweden	Wide bandgap semiconductor sensors
Peter Lodahl / Søren Stobbe	DTU Copenhagen, Denmark	Time resolved optics on single dots
Enrique López Cabarcos	Universidad Complutense de Madrid, Madrid, Spain	Diamond biosensors
Daniel Loss	University of Basel, Switzerland	Theory of carrier spin relaxation in QDs
Alison Mainwood	King's College London, London, UK	DFT calculations: organic molecules on diamond
Max Migliorato	University of Manchester, UK	Electronic structure calculations in strained nanostructures
Eva Monroy	Commissariat à l'Énergie Atomique, Grenoble, France	III-nitride quantum dots
Elias Munoz	Universidad Politécnica de Madrid, Madrid, Spain	Noise characterization of diamond transistors

Mark Newton	University of Warwick, Warwick, UK	Characterization of diamond films
David Norris	University of Minnesota, USA	Optical properties of colloidal QDs
Vittorio Pellegrini	University Pisa, Italy	Low energy excitations in quantum wires
Pierre Petroff	University of California, Santa Barbara, USA	Photonic crystal nanocavities
Serge Picaud	Institut National de la Santé et de la Recherche Médicale, Paris, France	Retina cells on diamond surfaces
Michael Povolotskyi, Aldo di Carlo	University of Rome „Tor Vergata“, Italy	Quantum transport, tight binding methods and nextnano ³ simulations
Joan Ramon Morante Jordi Arbiol	Universitat de Barcelona, Spain	III-nitride and metal-oxide nanostructures High resolution transmission electron microscopy of nanowires
Andrew Ramsay	University of Sheffield, Sheffield, UK	Ultrafast optics on quantum dots
Pere Roca i Cabarrocas	Ecole Polytechnique, Palaiseau, France	Synthesis of silicon nanowires
Lars Samuelson Anders Gustafson	Lund University, Sweden	Cathodoluminescence
Nobu Sawaki	Nagoya University, Japan	Electronic structure of quantum dots
Giorgio Sberveglieri	University of Brescia, Italy	Metal oxide chemical sensors
Paulo Sérgio Soares Guimarães	Federal University of Minas Gerais, Brazil	Theory of interband optical properties of quantum dots
Tadeusz Suski	Polish Academy of Sciences, Warsaw, Poland	III-nitride devices AlGaIn/GaN biosensors
Sasha Tartakovskii	University of Sheffield, Sheffield, UK	Nuclear spin phenomena in InGaAs-GaAs quantum dots
Eric Tournie	University of Montpellier 2, Montpellier, France	MBE for Antimonide-VCSELs
Sergio Ulloa	Ohio University, Ohio, USA	Spin polarization control via magnetic barriers and spin-orbit effects
Milan Vanecek	Fyzikalni ustav, Prague, Czech Republic	Optical characterization of diamond films
Naoki Yokoyama, Shozo Fujita	Fujitsu Laboratories Ltd, Atsugi, Japan	Protein sensors
Ning-Hua Zhu	Institute of Semiconductors, Chinese Academy of Sciences, Beijing	High-speed VCSELs, optical MIMOs

National collaborations

Partner	Institution	Subject
Andreas Bausch	Technische Universität München	Development of biosensors
Markus Betz	Technische Universität München	Time-resolved spectroscopy of quantum dots
Peter Feulner	Technische Universität München	Surface and interface analysis
Maximilian Fleischer	Siemens AG, München	Antibody immobilization on GaN VCSEL-based optical sensors
Alois Friedberger	EADS, München	DOTSENSE
Klaus Gaertner	WIAS Berlin	Numerische lineare Algebra-Methoden
Rüdiger Goldhahn	Technische Universität Ilmenau	Modulation spectroscopy of AlGaN/GaN heterostructures and ZnMgO layers
Achim Hartschuh	Ludwig-Maximilians-Universität München	Optoelectronics of hybrid carbon nanotube systems
Khaled Karrai	Attocube, Munich	Transmission experiments on quantum dots
Klaus von Klitzing, Jürgen Smet, Werner Dietsche	MPI für Festkörperforschung Stuttgart	Coupled 2d Systems, quantum Hall systems
Patrick Kölsch	Universität Heidelberg	SFG spectroscopy: diamond/water interfaces
Sigmund Kohler	Universität Augsburg	Ballistic photocurrents in mesoscopic structures
Erhard Kohn	Universität Ulm	Diamond biosensors
Jörg Peter Kotthaus	Ludwig-Maximilians-Universität München, CeNS, München	GaAs based hetero- and nanostructures, simulation of gated quantum dots
Alois Krost	Universität Magdeburg	AlGaN/GaN heterostructures
Ulrich Kunze	Universität Bochum	Coupled wires based on GaAs heterostructures
Armin Lambrecht	FhG IPM, Freiburg	Laser-based optical sensing
Song Li	Ludwig-Maximilians-Universität München	CVD-growth of carbon nanostructure
Paolo Lugli	Technische Universität München	Nano-imprint lithography of SOI photonic nanostructures
Peter Meissner	Technische Universität Darmstadt	Widely tunable MEMS-VCSEL
Bruno K. Meyer	Justus-Liebig-Universität Gießen	Spektroskopie von ZnMgO

Gerhard Müller	EADS Deutschland GmbH, München	Nano-optical chemical transducers
Roland Netz	Technische Universität München	Dynamic switching of DNA on gold
Bert Nickel	Ludwig-Maximilians- Universität München	Diamond/pentacene hetero- structures SAMs on GaN
Kornelius Nielsch	Universität Hamburg	Porous alumina templates and atomic layer deposition
Andreas Offenhaeusser	Forschungszentrum Jülich	Neurons on diamond ISFETs, cells on AlGaN/GaN FETs
Matthias Opel, Rudolf Gross, Sebastian Gönnerwein	Walther-Meissner-Institut, Garching	Magnetisation of GeMn, magnetic properties
Markus Ortsiefer	VERTILAS GmbH, Garching	InP-based VCSEL
Thomas Reichel	Rohde & Schwarz, München	Microwave monolithically integrated circuits (MMIC)
Jürgen Ristein	Universität Erlangen- Nürnberg	Diamond surface conductivity
Ulrich Schmid / Helmut Seidel	Universität des Saarlandes, Saarbrücken	GaN MEMS and NEMS
J. M. Schoening	Aachen University of Applied Sciences	Utilization of porous alumina for sensing
Matthias Schreck	Universität Augsburg	Heteroepitaxy of diamond
Marc Tornow	Universität Braunschweig	Biosensors, molecular electronics
Achim Trampert	Paul-Drude-Institut, Berlin	Transmission electron microscopy on GeMn
Klaus Wandelt	Universität Bonn	Electrochemical STM
Werner Wegscheider	Universität Regensburg	Molecular beam epitaxy, cleaved edge overgrowth quantum wires and dots
Carsten Werner	Max Bergmann Center of Biomaterials, Dresden	Electrokinetics at the diamond/water interface
Artur Zrenner	Universität Paderborn	Single quantum dot photo diodes

4. Members of the Institute, Postdocs, and Guest Scientists

Faculty Members and Scientific Staff

Gerhard Abstreiter
 Markus-Christian Amann
 Gerhard Böhm
 Dominique Bougeard
 Martin S. Brandt
 Martin Eickhoff
 Jonathan Finley
 Anna Fontcuberta i Morral

Jürgen Freyer
 José Antonio Garrido Ariza
 Alexander Holleitner
 Ralf Meyer
 Ulrich Rant
 Reinhard Scholz
 Martin Stutzmann
 Peter Vogl

Administrative and Technical Staff

Wolfgang Bendak
 Max Bichler
 Veronika Enter
 Michael Fischer
 Josef Grottenthaler
 Daniela Huber
 Bernhard Kratzer
 Liane Lindner
 Sonja Matich
 Regina Morinaga

Linda Mora
 Irmgard Neuner
 Claudia Paulus
 Hubert Riedl
 Edith Sckopke
 Friedrich Sedlmeir
 Elke Thiel
 Ralf Wasserrab
 Peter Weiser
 Adolf Ziegltrum

Postdocs

Anna Cattani-Scholz
 Joseph Dufouleur
 Svetoslav Koynov
 Lia Moreno Codinachs

Erika Pringsheim
 Rui Pereira
 Ian Sharp (Humboldt Fellow)

Visiting Scientists

Yasuhiko Arakawa, Univ. Tokyo, Japan
 Kenji Arinaga, Fujitsu Laboratories LTD, Kanagawa, Japan
 Simon Frederick (Humboldt Fellow)
 Jose M. Villas-Boas (Humboldt Fellow)

Doctorate Candidates (thesis completed*)

Philip Achatz
 Stefan Ahlers*
 Till Andlauer
 Tobias Antesberger
 Shamsul Arafin
 Alexander Bachmann

Wolfgang Kaiser
 Michael Kaniber
 Simone Kaniber
 Kaveh Kashani-Shirazi
 Simeon Katz
 Konrad Klein

Silvia Baldovino
 Barbara Baur
 Christoph Bihler
 Stefan Birner
 Jia Chen
 Emily Clark
 Carlo Colombo
 Markus Dankerl
 Shivaji Dasgupta*
 Oliver Dier*
 Roland Dietmüller
 Valentin Döring
 Dominic Dorfner
 Thomas Eißfeller
 Roland Enzmann
 Andrea Friedrich*
 Florian Furtmayr
 Wojciech Gajewski
 Tonko Garma
 Christian Grasse
 Peter Greck
 Tobias Gründl
 Andreas Härtl
 Andreas Hangauer
 Dominik Heiss
 Martin Heiß
 Martin Hermann
 Marco Hüb
 Felix Hofbauer
 Werner Hofmann
 John Howgate
 Nebile Isik
 Christian Jäger
 Vase Jovanov

Florian Klotz
 Jelena Knezevic
 Tillmann Kubis
 Arne Laucht
 Bernhard Laumer
 Robert Lechner
 Taek Lim
 Simon Lud
 Markus Mangold
 Michael Müller
 Sabrina Niesar
 Daniel Pedone
 Leonhard Prechtel
 Andreas Reitinger
 Johanna Rössler, geb. Simon
 Jürgen Sailer
 Susanne Schäfer
 Christoph Schindler
 Sebastian Schöll
 Michael Scholz
 Alexander Schwemer
 Narayan Sircar
 Dance Spirkoska
 Andre Stegner
 Georg Steinhoff*
 Lucia Steinke
 Sebastian Strobel
 Jörg Teubert
 Emanuele Uccelli*
 Thomas Wassner
 Olaf Weidemann
 Ying Xiang
 Ilaria Zardo
 Vera Zon

Diploma Students (thesis completed*)

Jakob Angele*
 Daniela Baierl*
 Mario Bareiß
 Matthias Bator
 Christian Böttner
 Gregor Bracher
 Matthias Brandstetter
 Jochen Bruckbauer*
 Felix Buth*
 Markus Cäsar*
 Carlo Diaz Alvarez
 Matthias Firnkes*
 Bastian Galler*

Hagen Langhuth
 Jinming Lu
 Michael Maier*
 Claudia Majer*
 Johannes Mösl
 Kai Müller
 Niko Münzenrieder*
 Helmut Nesswetter
 Andre Neumann*
 Sabrina Niesar*
 Dominik Pawlizki*
 Andreas Reitinger*
 Daniel Rudolph

Paul Hampel
 Markus Hanl
 Moritz Hauf*
 Norman Hauke
 Birgit Hausmann
 Matthias Heigoldt*
 Robert Heydenreich*
 Malte Huck
 Eike Janocha*
 Christian Jendrysik*
 Konrad Klein*
 Philipp Koch
 Marion Kraus
 Volker Lang*

Master Students

Chiara Cordioli*
 Makiko Maruyama*
 Cate Morgan
 Swarnakamal Priyabadini

Bachelor Students

Christopher Birkenstock
 Martin Bucher*
 Denis Bytschkow*
 Martin Eberl*

Konrad Schönleber
 Torben Schüttfort*
 Markus Schuster*
 Christian Seidel*
 Christoph Stark*
 Wiebke Steins*
 Benedikt Stoib
 Ulrich Stützel*
 Sebastian Thunich
 Markus Trautwein
 Christoph Weiß
 Ruoshan Wie
 Andreas Wild
 Thomas Zabel*

Augustinas Vizbaras
 Kristijonas Vizbaras
 Wang Yizhen
 Stefan Ziegler*

Christian Kraeh*
 Thomas Künzig*
 Matthias Sachsenhauser*

5. Doctoral, Diploma, Bachelor, and Master Theses

Doctoral Theses

1. *Quanten-Kaskaden-Laser ohne Injektorbereiche*
Andrea Friedrich (24.1.2008)
2. *Resonant photon-exciton enteraction in semiconductor quantum dots*
Martin Kroner (3.2008)
3. *Das Materialsystem (AlGaIn) (AsSb): Eigenschaften und Eignung für GaSb-basierte Vertikalresonator-Laserdioden*
Oliver Dier (28.4.2008)
4. *Resonant interband transmission spectroscopy on single charge-tunable quantum dots*
Stefan Seidl (5.2008)
5. *Group-III-nitrides for bio- and electrochemical sensors*
Georg Steinhoff (14.7.2008)
6. *Guided self-assembly of InAs quantum dots arrays on (110) surfaces*
Emanuele Uccelli (22.10.2008)
7. *Magnetic and electrical properties of epitaxial GeMn*
Stefan Ahlers (8.12.2008)
8. *Growth optimization and characterization of high mobility two-dimensional electron systems in AlAs quantum wells*
Shivaji Dasgupta (16.12.2008)

Diploma Theses

1. *Funktionalisierte GaN-Oberflächen: Charakterisierung und Photostrukturierung*
Wiebke Steins (1/2008)
2. *Towards the detection of neurotransmitters with diamond ENFETs*
Andreas Adam Reitingner (2/2008)
3. *Charge transport and spin-dependent recombination at the Si/SiO₂-interface*
Bastian Tobias Galler (3/2008)
4. *AC-Starkeffekt Messungen an einzelnen ladungsdurchstimmbaren Quantenpunkten*
Christine Lux (3/2008)

5. *Spin-dependent transport in silicon nanocrystal*
Konrad Klein (4/2008)
6. *Epitaxie und Charakterisierung von GaAs- und InP-basierten InAs-Quantenpunkten mit Emissionswellenlängen bei 1,3 μm und 1,55 μm*
Daniela Baierl (5/2008)
7. *Electrically tunable single quantum dot nanocavity*
Jakob Angele (5/2008)
8. *Prozessierung und Untersuchung injektorloser QCLs auf cw-Betriebsfähigkeit und Doppel-Wellenlängen-Emission*
Michael Maier (5/2008)
9. *Metall-induzierter Schichtaustausch von Silizium mit unterschiedlichen Diffusionsbarrieren*
Robert Heydenreich (7/2008)
10. *Characterisation of two-dimensional electron systems in natural and isotopically pure Si/SiGe heterostructures*
Volker Lang (7/2008)
11. *Transport Untersuchungen an Germanium und dünnen Schichten von Germanium-Mangan*
Claudia Majer (7/2008)
12. *Optical properties of GaAs nanowires and their heterostructures*
Matthias Heigoldt (8/2008)
13. *Structural properties of III-V nanowires and their heterostructures*
Eike Janocha (8/2008)
14. *Elektrische Eigenschaften von III-Nitrid Nanostrukturen*
Christoph Johannes Markus Stark (9/2008)
15. *Charakterisierung von InP-basierten Quantenpunkten und Nano-Resonatoren für effiziente Einzelphotonenerzeugung*
Christian Seidel (9/2008)
16. *Single photon phenomena in photonic crystal nanostructures*
Andre Neumann (9/2008)
17. *Hybride Solarzellen mit Silizium-Nanopartikeln*
Sabrina Niesar (10/2008)
18. *Diamond SGFETs for the detection of cell signals*
Veit Moritz Hauf (10/2008)

19. *Optically induced charge storage in a single quantum dot*
Markus Cäsar (10/2008)
20. *Preparation and characterization of solid state nanopores in silicon nitride*
Matthias Firnkes (10/2008)
21. *Growth of organic semiconductors on diamond substrates*
Felix Buth (11/2008)
22. *Wachstum und Charakterisierung von ZnO/ZnMgO-Heterostrukturen*
Jochen Bruckbauer (11/2008)
23. *Surface conductivity at the diamond/electrolyte interface*
Eberhard Ulrich Stützel (11/2008)
24. *Technologieentwicklung für eine Einzelphotonenquelle bei 1,55 μm*
Christian Jendrysik (11/2008)
25. *Hochreflektierende und polarisationsselektive Subwellenlängengitter für oberflächenemittierende Laserdioden*
Niko Münzenrieder (11/2008)
26. *Engineering the structural and optical properties of single quantum dots and quantum dot molecules*
Dominik Pawlizki (11/2008)
27. *Spectroscopic characterization of metalized DYE-DNA complexes*
Markus Schuster (12/2008)
28. *Optical biosensing using SOI photonic crystal nanostructures*
Thomas Zabel (12/2008)
29. *Optical, structural, and electronic properties of thin polycrystalline silicon layers*
Matthias Jakob Bator (12/2008)
30. *Synthesis and spectroscopic studies of single-walled carbon nanotube – conjugated polymer compounds*
Torben Schüttfort (12/2008)
31. *Untersuchung indirekter Exzitonen in gekoppelten InGaAs-Quantentöpfen*
Markus Stallhofer (12/2008)

Bachelor Theses

1. *Application of diamond as an electrode*
Denis Bytschkow (7/2008)
2. *Soft-Lithographie nanopartikulärer Systeme*
Matthias Sachsenhauser (8/2008)
3. *Phosphorus in microcrystalline silicon*
Martin Eberl (8/2008)
4. *Detection of gold-induced defects in black-etched silicon for solar cells*
Martin Bucher (9/2008)
5. *Silver-induced nanotexturing for silicon surfaces*
Christian Kraeh (9/2008)
6. *Herstellung und Charakterisierung von Laserdioden im Bereich der Kommunikationswellenlängen*
Thomas Künzig (10/2008)

Master Theses

1. *Sensitivity increase of element specific metal detection in Si by DLTS and other physical methods*
Rhenda R Mukti (3/2008)
2. *Study of DNA hybridization and protein binding kinetics on wwitchable DNA surfaces*
Makiko Maruyama (10/2008)
3. *Diamond electrodes: an electrochemical characterization in sodium chloride*
Chiara Cordioli (12/2008)
4. *Development and characterization of active regions for GaSb-based VCSELs*
Stefan Ziegler (12/2008)

6. Publications

Injectorless quantum cascade lasers for the mid-infrared

M.-C. Amann and S. Katz

Radio Science Bulletin **326**, 20-28 (2008)

Gauge-invariant discretization in multiband envelope function theory and g factors in nanowire dots

T. Andlauer, R. Morschl, and P. Vogl

Phys. Rev. **B78**, 075317 (2008)

Ultra-thin polycrystalline Si layers on glass prepared by aluminum-induced layer exchange

T. Antesberger, C. Jäger, and M. Stutzmann

J. Non-Cryst. Sol. **354**, 2324-2328 (2008)

Influence of the (111) twinning on the formation of diamond cubic/diamond hexagonal heterostructures in Cu-catalyzed Si nanowires

J. Arbiol, A. Fontcuberta i Morral, S. Estradé, F. Peiró, B. Kalache, P. Roca I Cabarrocas, and J. R. Morante

J. Appl. Phys. **104**, 064312 (2008)

Continuous-wave operation of electrically pumped GaSb-based vertical cavity surface emitting laser at 2.3 μm

A. Bachmann, T. Lim, K. Kashani-Shirazi, O. Dier, C. Lauer, and M.-C. Amann

Electr. Lett. **44**, 202-U12 (2008)

GaSb-based electrically pumped VCSEL with buried tunnel junction operating continuous wave up to 50°C

A. Bachmann, K. Kashani-Shirazi, and M.-C. Amann

21th IEEE International Semiconductor Laser Conference, Sorrento, Italy, 39-40 (2008)

Shock waves in nanomechanical resonators

F. W. Beil, A. Wixforth, W. Wegscheider, D. Schuh, M. Bichler, and R. H. Blick

Phys. Rev. Lett. **100**, 026801 (2008)

Diffraction loss in long-wavelength buried tunnel junction VCSELs analyzed with a hybrid coupled-cavity transfer-matrix model

J. Bengtsson, J. Gustavsson, A. Haglund, A. Larsson, A. Bachmann, K. Kashani-Shirazi, and M.-C. Amann

Optics Express **16**, 25 (2008)

Photodoping with CdSe nanocrystals as a tool to probe trap state distributions in C60 crystals

Appl. Phys. **B 93**, 239 (2008)

A. Biebersdorf, R. Dietmueller, A. Ohlinger, T. A. Klar, J. Feldmann, D. V. Talapin, and H. Weller

Suppression of hole-mediated ferromagnetism in $Ga_{1-x}Mn_xP$ by hydrogen

C. Bihler, M. Kraus, M. S. Brandt, S. T. B. Goennenwein, M. Opel, M. A. Scarpulla, M. Farshchi, and O. Dubon

arXiv: 0707.2777 (2007)

J. Appl. Phys. **104**, 013908 (2008)

$Ga_{1-x}Mn_xAs$ /piezoelectric actuator hybrids: A model system for magnetoelastic magnetization manipulation

C. Bihler, M. Althammer, A. Brandlmaier, S. Geprägs, M. Weiler, M. Opel, W. Schoch, W. Limmer, R. Gross, M. S. Brandt, and S. T. B. Goennenwein

arXiv: 0804.1336 (2008)

Phys. Rev. **B78**, 045203 (2008)

Local structure of Mn in hydrogenated $Ga_{1-x}Mn_xAs$

C. Bihler, G. Ciatto, H. Huebl, G. Martinez-Criado, P. J. Klar, K. Volz, W. Stolz, W. Schoch, W. Limmer, F. Filippone, A. Amore Bonapasta, and M. S. Brandt

Phys. Rev. **B78**, 235208 (2008)

Simulation of quantum cascade lasers - optimizing laser performance

S. Birner, T. Kubis, and P. Vogl

Photonik international **2**, 60 (2008)

Simulation zur Optimierung von Quantenkaskadenlasern

S. Birner, T. Kubis, and P. Vogl

Photonik 1/2008, 44 (2008)

Theoretical model for the detection of charged proteins with a silicon-on-insulator sensor

S. Birner, C. Uhl, M. Bayer, and P. Vogl

J. Phys.: Conf. Ser. **107**, 012002 (2008)

In situ manipulation of magnetic anisotropy in magnetite thin films

A. Brandlmaier, S. Geprägs, M. Weiler, A. Boger, M. Opel, H. Huebl, C. Bihler, M. S. Brandt, B. Botters, D. Grundler, R. Gross, and S. T. B. Goennenwein

Phys. Rev. **B77**, 104445 (2008)

Bandstructure and photoluminescence of SiGe islands with controlled Ge concentration

M. Brehm, T. Suzuki, Z. Zhong, T. Fromherz, J. Stangl, G. Hesser, S. Birner, F. Schäffler, and G. Bauer

Microelectronics J. **39**, 485 (2008)

Silicon-on-insulator based nanopore cavity arrays for lipid membrane investigation
K. Buchholz, A. Tinazli, A. Kleefen, D. Dorfner, D. Pedone, U. Rant, R. Tampé,
G. Abstreiter, and M. Tornow
Nanotechnology **19**, 445305 (2008)

Organophosphonate based PNA-functionalization of silicon nanowires for label-free DNA detection
A. Cattani-Scholz, D. Pedone, M. Dubey, S. Neppel, B. Nickel, P. Feulner, J. Schwartz,
G. Abstreiter, and M. Tornow
ACS Nano **2**, 1653 - 1660 (2008)

Accurate extraction method of the FM response of VCSELs based on wavelength modulation spectroscopy
J. Chen, A. Hangauer, R. Strzoda, and M.-C. Amann
Appl. Phys. B: Lasers and Optics **90**, 243-247 (2008)

Simplified model of the dynamic thermal tuning behavior of VCSELs
J. Chen, A. Hangauer, and M.-C. Amann
IEEE Photonics Technology Letters **20**, 1082-1084 (2008)

Selected Peer-Reviewed Articles from the Symposium "O - Functional Organic and Inorganic Materials for Micro and Nano Bio-Sensing Systems" of the EMRS Spring Meeting 2007, Sensor Letters 6, (2008), ed. by N. Cioffi, E. Comini, M. Eickhoff, and L. Torsi

Ga-assisted catalyst-free growth mechanism of GaAs nanowires by molecular beam epitaxy
C. Colombo, D. Spirkoska, M. Frimmer, G. Abstreiter, and A. Fontcuberta i Morral
Phys. Rev. **B77**, 155326 (2008)

Resolving the controversy on the pH sensitivity of diamond surfaces
M. Dankerl, A. Reitingner, M. Stutzmann, and J. A. Garrido
phys. stat. sol. (RRL) **2**, No. 1, 31-33 (2008)

Single-valley high-mobility (110) AlAs quantum wells with anisotropic mass
S. Dasgupta, S. Birner, C. Knaak, M. Bichler, A. Fontcuberta i Morral, G. Abstreiter, and M. Grayson
Appl. Phys. Lett. **93**, 132102 (2008)

Modal properties of long-wavelength tunable MEMS-VCSELs with curved mirrors: comparison of experiment and modeling
P. Debernardi, B. Kögel, K. Zogal, P. Meissner, M. Maute, M. Ortsiefer, G. Böhm, and M.-C. Amann
IEEE J. Quantum Electr. **44**, 391-399 (2008)

Reduction of hetero-interface resistivity in n-type AlAsSb/GaSb distributed Bragg reflectors

O. Dier, C. Reindl, A. Bachmann, C. Lauer, T. Lim, K. Kashani-Shirazi, and M.-C. Amann
Semicond. Sci. & Techn. **23**, Art.No. 025018 (2008)

Silicon photonic crystal nanostructures for refractive index sensing

D. F. Dorfner, T. Hürlimann, T. Zabel, L. H. Frandsen, G. Abstreiter, and J. J. Finley
Appl. Phys. Lett. **93**, 181103 (2008)

Optical absorption glucose measurements using 2.3 μm vertical-cavity semiconductor lasers

S. T. Fard, W. Hofmann, P. T. Fard, G. Böhm, M. Ortsiefer, E. Kwok, M.-C. Amann, and L. Chrostowski
IEEE Photonics Techn. Lett. **20**, 930-932 (2008)

Nucleation mechanism of gallium-assisted molecular beam epitaxy growth of gallium arsenide nanowires

A. Fontcuberta I Morral, C. Colombo, G. Abstreiter, J. Arbiol, and J. R. Morante
Appl. Phys. Lett. **92**, 063112 (2008)

Erratum: Nucleation mechanism of gallium-assisted molecular beam epitaxy growth of gallium arsenide nanowires

A. Fontcuberta i Morral, K. Maslov, C. Colombo, G. Abstreiter, J. Arbiol, and J. R. Morante
Appl. Phys. Lett. **92**, 149903 (2008)

Prismatic quantum heterostructures synthesized on molecular-beam epitaxy GaAs nanowires

A. Fontcuberta i Morral, D. Spirkoska, J. Arbiol, M. Heigoldt, J. R. Morante, and G. Abstreiter
Small **4**, No. **7**, 899-903 (2008)

Nucleation and growth of GaN nanorods on Si(111) surfaces by plasma-assisted molecular beam epitaxy – The influence of Si and Mg-doping

F. Furtmayr, M. Vielemeyer, M. Stutzmann, J. Arbiol, S. Estradé, F. Peirò, J. Ramon Morante, and M. Eickhoff
J. Appl. Phys. **104**, 034309 (2008)

Optical properties of Si- and Mg-doped gallium nitride nanowires grown by plasma-assisted molecular beam epitaxy

F. Furtmayr, M. Vielemeyer, M. Stutzmann, A. Laufer, B. K. Meyer, and M. Eickhoff
J. Appl. Phys. **104**, 074309 (2008)

Loading indirect excitons into an electrostatic trap formed in coupled GaAs quantum wells

A. Gärtner, D. Schuh, A.W. Holleitner, and J. P. Kotthaus
Physica **E40**, 1828 (2008)

Electronic and optical properties of boron-doped nanocrystalline diamond films

W. Gajewski, P. Achatz, O. A. Williams, K. Haenen, E. Bustarret, M. Stutzmann, and J. A. Garrido
Phys. Rev. **B79**, 045206-1-14 (2008)

Exciton emission on PTCDA thin films under uniaxial pressure

V. R. Gangilenka, A. DeSilva, H. P. W. R. E. Tallman, B. A. Weinstein, and R. Scholz
Phys. Rev. **B77**, 115206 (2008)

Absorption of Frenkel excitons in PTCDA thin films, in PTCDA/Alq3 multilayers and in co-deposited films

V. R. Gangilenka, A. DeSilva, H. P. Wagner, H. Schmitzer, R. Scholz, and T. U. Kampen
in: Proc. 28th Int. Conf. Physics of Semiconductors (ICPS-28), Wien, 2006;
AIP Conf. Proc. 893, 357-8 (2007)

All-electric detection of the polarization state of terahertz laser radiation

S. D. Ganichev, W. Weber, J. Kiermaier, S. N. Danilov, P. Olbrich, D. Schuh, W. Wegscheider, D. Bougeard, G. Abstreiter, and W. Prettl
J. Appl. Phys. **103**, 114504 (2008)

The diamond/aqueous electrolyte interface: an impedance investigation

J. A. Garrido, S. Nowy, A. Härtl, and M. Stutzmann
Langmuir **24**, 3897-3904 (2008)

The surface conductivity at the diamond/aqueous electrolyte interface

J. A. Garrido, A. Härtl, M. Dankerl, A. Reitingner, M. Eickhoff, A. Helwig, G. Müller, and M. Stutzmann
J. Amer. Chem Soc. **130**, 4177-4181 (2008)

Intraband Auger effect in InAs/InGaAlAs/InP quantum dot structures

T. Gebhard, D. Alvarenga, P. L. Souza, P. S. S. Guimaraes, K. Unterrainer, M. P. Pires, G. S. Vieira, and J. M. Villas-Boas
Appl. Phys. Lett. **93**, 052103 (2008)

Hydrophobic and Hofmeister effects on the adhesion of spider silk proteins onto solid substrates: an AFM-based single molecule study

M. Geisler, T. Pirzer, C. Ackerschott, S.Q. Lud, J.A. Garrido, T. Scheibel, and T. Hugel
Langmuir **24** (4), 1350-1355 (2008)

Piezo-voltage control of magnetization orientation in a ferromagnetic semiconductor
S. T. B. Goennenwein, M. Althammer, C. Bihler, A. Brandlmaier, S. Geprägs,
M. Opel, W. Schoch, W. Limmer, R. Gross, and M. S. Brandt
phys. stat. sol. (RRL) **2**, 96 (2008)

Growth of various antimony-containing alloys by MOVPE
C. Grasse, G. Böhm, U. Breuer, R. Meyer, and M.-C. Amann
J. Cryst. Growth **310**, 4835-4838 (2008)

Sharp quantum Hall edges: Experimental realizations of edge states without incompressible strips
M. Grayson, L. Steinke, M. Huber, D. Schuh, M. Bichler, and G. Abstreiter
phys. stat. sol. (b) **245**, 356-365 (2008)

Optically injection-locked VCSEL as a duplex transmitter/receiver
Q. Gu, W. Hofmann, M.-C. Amann, and L. Chrostowski
IEEE Photonics Technology Letters **20**, 463-465 (2008)

Enzyme modified field effect transistors based on surface conductive single crystalline diamond
A. Härtl, B. Baur, M. Stutzmann, and J. A. Garrido
Langmuir **24** (1) 9898-9906 (2008)

Modeling of the n-th harmonic spectra used in wavelength modulation spectroscopy and their properties
A. Hangauer, J. Chen, and M.-C. Amann
Appl. Phys. B – Lasers and Optics **90**, 249-254 (2008)

Wavelength modulation spectroscopy with a widely tunable InP-based 2.3 μm vertical-cavity surface-emitting laser
A. Hangauer, J. Chen, R. Strzoda, M. Ortsiefer, and M.-C. Amann
Opt. Lett. **33**, 1566-1568 (2008)

Room temperature nanoimprint lithography using molds fabricated by molecular beam epitaxy
S. Harrer, S. Strobel, G. Scarpa, G. Abstreiter, M. Tornow, and P. Lugli
IEEE Transactions on Nanotechnology **7**, No. 3, 363-370 (2008)

Exciton phonon coupling in diindenoperylene thin films
U. Heinemeyer, R. Scholz, L. Gisslen, M. I. Alonso, J. O. Osso, M. Garriga,
A. Hinderhofer, M. Kytka, S. Kowarik, A. Gerlach, and F. Schreiber
Phys. Rev. **B78**, 085210 (2008)

Charge and spin readout scheme for single self-assembled quantum dots
D. Heiss, V. Jovanov, M. Bichler, G. Abstreiter, and J. J. Finley
Phys. Rev. **B77**, 235442 (2008)

Growth mechanisms and optical properties of GaAs-based semiconductor microstructures by selective area epitaxy

M. Heiß, E. Riedlberger, D. Spirkoska, M. Bichler, G. Abstreiter, and A. Fontcuberta i Morral
J. Cryst. Growth **310**, 1049-1056 (2008)

Gas sensing properties of hydrogen-terminated diamond

A. Helwig, G. Müller, J.A. Garrido, and M. Eickhoff
Sensors and Actuators B **133**, 156 (2008)

Dynamic photoconductive gain effect in shallow-etched AlGaAs/GaAs quantum wires

K.-D. Hof, C. Roessler, J. P. Kotthaus, A.W. Holleitner, D. Schuh, and W. Wegscheider
Phys. Rev. **B78**, 115325 (2008)

Optically induced charge transport through submicron channels

K.-D. Hof, C. Roessler, W. Wegscheider, S. Ludwig, and A. W. Holleitner
Physica **E40**, 6, 1820 (2008)

Long-wavelength vertical-cavity surface-emitting lasers for high-speed applications and gas sensing

W. Hofmann and M.-C. Amann
IET Optoelectr. **2**, 134-142 (2008)

1.55 μm VCSEL arrays for high-bandwidth WDM-PONs

W. Hofmann, E. Wong, G. Böhm, M. Ortsiefer, N. H. Zhu, and M.-C. Amann
IEEE Photonics Techn. Lett. **20**, 291-293 (2008)

Long-wavelength VCSELs and VCSEL arrays for high-speed, high-power and high sensitivity

W. Hofmann, G. Böhm, M. Ortsiefer, and M.-C. Amann
 in: Proc. of III. Intern. Conf. on Laser Processes and Components (LPC), Shanghai, China, (2008) pp 33-34

Monolithic 2-D high-power arrays of long-wavelength VCSELs

W. Hofmann, M. Görblich, M. Ortsiefer, G. Böhm, and M.-C. Amann
Photonics West, San Jose, USA, 6908-06 pp. 1-7 (2008)

One and two-dimensional long-wavelength VCSEL arrays for WDM applications and optical interconnects

W. Hofmann, E. Wong, M. Ortsiefer, M. Görblich, G. Böhm, and M.-C. Amann
 21th IEEE International Semiconductor Laser Conference, Sorrento, Italy, 165-166 (2008)

High-power long-wavelength VCSEL arrays

W. Hofmann, M. Görblich, M. Ortsiefer, G. Böhm, and M.-C. Amann
 21th IEEE International Semiconductor Laser Conference, Sorrento, Italy, 141-142 (2008)

- Diffuse x-ray scattering from inclusions in ferromagnetic $Ge_{1-x}Mn_x$ layers*
 V. Holý, R. T. Lechner, S. Ahlers, L. Horák, T. H. Metzger, A. Navarro-Quezada, A. Trampert, D. Bougeard, and G. Bauer
 Phys. Rev. **B78**, 144401 (2008)
- Single molecule peptide hydrophobicity results from the interplay of water structure effects and dispersion interaction*
 D. Horinek, A. Serr, M. Geisler, T. Pirzer, U. Slotta, S. Q. Lud, J. A. Garrido, T. Scheibel, T. Hugel, and R. R. Netz
 in: Proc. Nat. Acad. Sci. **105** (8) 2842-2847 (2008)
- Spin echoes in the charge transport through phosphorus donors in silicon*
 H. Huebl, F. Hoehne, B. Grolík, A.R. Stegner, M. Stutzmann, and M. S. Brandt
 Phys. Rev. Lett. **100**, 177602 (2008)
- Self-diffusion in germanium isotope multilayers at low temperatures*
 E. Hüger, U. Tietze, D. Lott, H. Bracht, D. Bougeard, E. E. Haller, and H. Schmidt
 Appl. Phys. Lett. **93**, 162104 (2008)
- Shadow modulated two-dimensional heterostructures using vertical pillars*
 N. Isik, M. Bichler, S. F. Roth, A. Fontcuberta, O. Göktas, and M. Grayson
 Appl. Phys. Lett. **92**, 173505 (2008)
- Hydrogen passivation of ultra-thin low-temperature polycrystalline silicon films for electronic applications*
 C. Jäger, T. Antesberger, and M. Stutzmann
 J. Non-Cryst. Sol. **354**, 2314-2318 (2008)
- GaN/AlN short-period superlattices for intersubband optoelectronics: A systematic study of their epitaxial growth, design, and performance*
 P. K. Kandaswamy, F. Guillot, E. Bellet-Amalric, E. Monroy, L. Nevou, M. Tchernycheva, A. Michon, F. H. Julien, E. Baumann, F. R. Giorgetta, D. Hofstetter, T. Remmele, M. Albrecht, S. Birner, and L. S. Dang
 J. Appl. Phys. **104**, 093501 (2008)
- Highly efficient single-photon emission from single quantum dots within a two-dimensional photonic band-gap*
 M. Kaniber, A. Laucht, T. Hürlimann, M. Bichler, R. Meyer, M.-C. Amann, and J. Finley
 Phys. Rev. **B77**, 073312 (2008)
- Tunable single quantum dot nanocavities for cavity QED experiments*
 M. Kaniber, A. Laucht, A. Neumann, M. Bichler, M.-C. Amann, and J. Finley
 3. Phys.: Condens. Matter **20**, 454209 (2008)

Investigation of the nonresonant dot-cavity coupling in two-dimensional photonic crystal nanocavities

M. Kaniber, A. Laucht, A. Neumann, J. M. Villas-Boas, M. Bichler, M.-C. Amann, and J. Finley
Phys. Rev. **B77**, 161303 (2008)

Simulation of active regions for GaSb-based VCSELs

K. Kashani-Shirazi, A. Bachmann, S. Arafin, S. Ziegler, and M.-C. Amann
International Nano Optoelectronics Workshop, Tokyo, Japan (2008)

MBE growth of active regions for electrically-pumped, cw-operating GaSb-based VCSELs

K. Kashani-Shirazi, A. Bachmann, G. Böhm, S. Ziegler, and M.-C. Amann
J. Crystal Growth **311**, 1908-1911 (2008)

Continuous wave operation of injectorless quantum cascade lasers at low temperatures

S. Katz, A. Friedrich, G. Böhm, and M.-C. Amann
Appl. Phys. Lett. **92**, Art.No. 181103 (2008)

Dual wavelength emission in injectorless quantum cascade lasers

S. Katz, M. Maier, G. Böhm, and M.-C. Amann
in: Proc. of 20th IPRM, Versailles, France (2008)

Low-threshold injectorless quantum cascade laser with four material compositions

S. Katz, G. Böhm, and M.-C. Amann
Electron. Lett. **44**, 580-581 (2008)

Resonant two-color high-resolution spectroscopy of a negatively charged exciton in a self-assembled quantum dot

M. Kroner, K. M. Weiss, B. Biedermann, S. Seidl, A. W. Holleitner, A. Badolato, P. M. Petroff, P. Öhberg, R. J. Warburton, and K. Karrai
Phys. Rev. **B78**, 075429 (2008)

Rabi splitting and AC-Stark shift of a charged exciton

M. Kroner, C. Lux, S. Seidl, A. W. Holleitner, K. Karrai, R. J. Warburton, A. Badolato, and P. M. Petroff
Appl. Phys. Lett. **92**, 031108 (2008)

Resonant saturation laser spectroscopy of a single self-assembled quantum dot

M. Kroner, S. Remi, A. Högele, S. Seidl, A. W. Holleitner, R. J. Warburton, B. D. Gerardot, P. M. Petroff, and K. Karrai
Physica **E40**, 1994 (2008)

Optical detection of single spin resonance in a quantum dot

M. Kroner, K. Weiss, B. Biedermann, S. Seidl, S. Manus, A. W. Holleitner,
A. Badolato, P.M. Petroff, B. Gerardot, R. J. Warburton, and K. Karrai
Phys. Rev. Lett. **100**, 156803 (2008)

Microscopic theory of spin-filtering in non-magnetic semiconductor nanostructures

T. Kubis and P. Vogl
phys. stat. sol. (c) **5**, 290 (2008)

Quantum theory of transport and optical gain in quantum cascade lasers

T. Kubis, C. Yeh, and P. Vogl
phys. stat. sol. (c) **5**, 232 (2008)

Non-equilibrium quantum transport theory: Current and gain in quantum cascade lasers

T. Kubis, C. Yeh, and P. Vogl
J. Comput. Electron. **7**, 432 (2008)

Electronic properties of doped silicon nanocrystal films

R. Lechner, A. R. Stegner, R. N. Pereira, R. Dietmüller, M. S. Brandt, A. Ebbers,
M. Trocha, H. Wiggers, and M. Stutzmann
J. Appl. Phys. **104**, 053701 (2008)

Advanced resistivity model for arbitrary magnetization orientation applied to a series of compressive- to tensile-strained (Ga,Mn)As layers

W. Limmer, J. Daeubler, L. Dreher, M. Glunk, W. Schoch, S. Schwaiger, and R. Sauer
Phys. Rev. **B 77**, 205210 (2008)

Spin polarization control via magnetic barriers and spin-orbit effects

A. T. Ngo, J. M. Villas-Boas, and S. E. Ulloa
Phys. Rev. **B78**, 245310 (2008)

High speed 1.3 μm VCSELs for 12.5 Gbit/s optical interconnects

M. Ortsiefer, W. Hofmann, E. Rönneberg, A. Boletti, A. Gatto, P. Boffi, J. Roskopf,
R. Shau, C. Neumeier, G. Böhm, M. Martinelli, and M.-C. Amann
Electron. Lett. **44**, 974-975 (2008)

Top-down versus bottom-up

W. J. Parak, F. C. Simmel, and A.W. Holleitner
in: Nanotechnology, Vol. 1: Principles and Fundamentals, ed.by Günter Schmid,
Wiley-VCH Verlag GmbH & C KGaA

Optically induced transport properties of freely suspended semiconductor submicron channels

C. Rössler, K.-D. Hof, S. Manus, S. Ludwig, J. P. Kotthaus, J. Simon,
A. W. Holleitner, D. Schuh, and W. Wegscheider
Appl. Phys. Lett. **93**, 071107 (2008)

Laterally defined freely suspended quantum dots in GaAs/AlGaAs heterostructures
C. Rössler, M. Bichler, D. Schuh, W. Wegscheider, and S. Ludwig
Nanotechnology **19**, 165201 (2008)

Non-magnetic compensation in ferromagnetic Ga_{1-x}MnxAs and Ga_{1-x}MnxP synthesized by ion implantation and pulsed-laser melting
M. A. Scarpulla, P. R. Stone, I. D. Sharp, E. E. Haller, O. D. Dubon, J. W. Beeman, and K. M. Yu
J. Appl. Phys. **103**, 123906 (2008)

Analysis of the exciton-exciton interaction in semiconductor quantum wells
C. Schindler and R. Zimmermann
Phys. Rev. **B78**, 045313 (2008)

Functionalization of 6H-SiC surfaces with organosilanes
S. J. Schoell, M. Hoeb, I.D. Sharp, W. Steins, M. Eickhoff, M. Stutzmann, and M. S. Brandt
Appl. Phys. Lett. **92**, 153301 (2008)

Silver-induced layer exchange for the low-temperature preparation of intrinsic polycrystalline silicon films
M. Scholz, M. Gjukic, and M. Stutzmann
Appl. Phys. Lett. **94**, 012108 (2008)

Potentiometry on pentacene OFETs: Charge carrier mobilities and injection barriers in bottom and top contact configurations
R. Scholz, D. Lehmann, A. D. Müller, F. Müller, and D. R. T. Zahn
phys. stat. sol. (a) **205**, 591 (2008)

Resonant transmission spectroscopy on the p- to-p transitions of a charge tunable InGaAs quantum dot
S. Seidl, M. Kroner, C. Lux, S. Seidl, A. W. Holleitner, K. Karrai, R. J. Warburton, A. Badolato, and P. M. Petroff
Appl. Phys. Lett. **92**, 153103 (2008)

Statistics of quantum dot exciton fine structure splittings and their polarization orientations
S. Seidl, B. D. Gerardot, P. A. Dalgarno, K. Kowalik, A. W. Holleitner, P. M. Petroff, K. Karrai, and R. J. Warburton
Physica **E40**, 2153 (2008)

Peptide adsorption on a hydrophobic surface results from an interplay of solvation, surface, and intrapeptide forces
A. Serr, M. Geisler, T. Pirzer, U. Slotta, S. Q. Lud, J. A. Garrido, T. Scheibel, T. Hugel, and R. R. Netz
in: Proc. Nat. Acad. Scie. **105**, no. 8 (2008)

Electronic properties of self-assembled alkyl monolayers on Ge surfaces

I. D. Sharp, S. J. Schoell, M. Hoeb, M. S. Brandt, and M. Stutzmann
 Appl. Phys. Lett. **92**, 223306-1-3 (2008)

Confinement effects on decay rate of surface electron states over liquid helium

S. S. Sokolov, Yu. P. Monarkha, J. M. Villas-Boas, and N. Studart
 Low Temp. Phys. **34**, 385 (2008)

A carbon nano-filament-bead necklace

L. Song, A. W. Holleitner, H. Qian, A. Hartschuh, M. Döblinger, E. M. Weig, and
 J. P. Kotthaus
 J. Phys. Chem. **B112**, 9644 (2008)

Size and environment dependence of surface phonon modes of gallium arsenide nanowires as measured by Raman spectroscopy

D. Spirkoska, G. Abstreiter, and A. Fontcuberta i Morral
 Nanotechnology **19**, 435704 (2008)

The use of molecular beam epitaxy for the synthesis of high purity III – V nanowires

D. Spirkoska, C Colombo, M Heiss, G Abstreiter, and A. Fontcuberta i Morral
 J. Phys.: Cond. Matt. **20**, 454225 (2008)

 S_1 - S_0 transition of 2,3-benzofluorene in the gas phase

A. Staicu, G. Rouille, R. Scholz, D. Pouladsaz, T. Henning, and F. Huisken
 J. Chem. Phys. **129**, 74302 (2008)

Electronic transport in phosphorus-doped silicon nanocrystal networks

A. R. Stegner, R. N. Pereira, K. Klein, R. Lechner, R. Dietmüller, M. S. Brandt,
 and M. Stutzmann
 Phys. Rev. Lett. **100**, 2 026803 (2008)

Nanometer-scale sharpness in corner-overgrown heterostructures

L. Steinke, P. Cantwell, D. Zakharov, E. Stach, N. J. Zaluzec, A. Fontcuberta i Morral,
 M. Bichler, G. Abstreiter, and M. Grayson
 Appl. Phys. Lett. **93**, 193117 (2008)

Hopping conduction in strongly insulating states of a diffusive bent quantum Hall junction

L. Steinke, D. Schuh, M. Bichler, G. Abstreiter, and M. Grayson
 Phys. Rev. **B77**, 235319 (2008)

Compensation-dependent in-plane magnetization reversal processes in $Ga_{1-x}Mn_xP_{1-y}S_y$

P. R. Stone, C. Bihler, M. Kraus, M. A. Scarpulla, J. W. Beeman, K. M. Yu,
 M. S. Brandt, and O. D. Dubon
 Phys. Rev. **B78**, 214421 (2008)

Silicon based nanogap device for studying electrical transport phenomena in molecule nanoparticle hybrids

S. Strobel, R. Murcia Hernández, A. G. Hansen, and M. Tornow
J. Phys.: Cond. Matt. **20** (37), 374126 (2008)

Deposition of PdAu thin films sectioned by sub-15-nm gaps on silicon using direct nanotransfer printing

S. Strobel, S. Harrer, G. Penso-Blanco, G. Scarpa, G. Abstreiter, P. Lugli, and M. Tornow

in: Proc. 8th IEEE Int. Conf. on Nanotechnology (IEEE-NANO), August 2008, Arlington, Texas, USA, art. no. **4617034** (2008) pp. 155-156

Electrical manipulation of DNA on metal surfaces

M. Tornow, K. Arinaga, and U. Rant

Invited book article for “NanoBioTechnology: BioInspired devices and materials of the future”, I. Levy and O. Shoseyov (Eds.), Humana Press (2008), pp. 187

Self-assembly of InAs quantum dot structures on cleaved facets, in “Self-Assembled Quantum Dots”

E. Uccelli, J. Bauer, M. Bichler, D. Schuh, J. J. Finley, G. Abstreiter and A. Fontcuberta i Morral

in: Self-Assembled Quantum Dots, ed. by Z.M. Wang et al, Springer Verlag, (2008), pp 25

Controlled synthesis of InAs wires, dot and twin-dot array configurations by cleaved edge overgrowth

E. Uccelli, M. Bichler, S. Nürnberger, G. Abstreiter, and A. Fontcuberta i Morral
Nanotechnology **19**, 045303 (2008)

Growth mechanisms of self assembled InAs quantum dots on (110) AlAs/GaAs cleaved facets

E. Uccelli, S. Nürnberger, M. Bichler, G. Abstreiter, and A. Fontcuberta i Morral
Superlatt. & Microstruct. **44**, 425-430 (2008)

Modelling absorption and photoluminescence of TPD

I. Vragovic, E. M. Calzado, M. A. D. Garcia, C. Himcinschi, L. Gisslen, and R. Scholz
J. Lumin. **128**, 845-7 (2008)

Quantum size effects in the optical properties of organic superlattices containing 3,4,9,10 perylene tetracarboxylic dianhydride (PTCDA)

I. Vragovic, J. P. Setrajcic, and R. Scholz
Eur. Phys. J. **B 66**, 185 (2008)

Broadband electrically detected magnetic resonance of phosphorus donors in a silicon field-effect transistor

L. H. Willems van Beveren, H. Huebl, D. R. McCamey, T. Duty, A. J. Ferguson, R. G. Clark, and M. S. Brandt

arXiv: 0805.4244 (2008)

Appl. Phys. Lett. **93**, 072102 (2008)

Microstructured horizontal alumina pore arrays as growth templates for large area few and single nanowire devices

Y. Xiang, W. Lee, K. Nielsch, G. Abstreiter, and A. Fontcuberta i Morral

phys. stat. sol. (RRL) **2**, No. 2, 59-61 (2008)

Inelastic light scattering study of the $\nu = 1$ quantum Hall ferromagnet

A. S. Zhuravlev, A. B. Van`kov, L. V. Kulik, I. V. Kukushkin, V. E. Kirpichev, J. H. Smet, K. v. Klitzing, V. Umsanky, and W. Wegscheider

Phys. Rev. **B77**, 155404 (2008)

Intersublevel polaron dephasing in self-assembled quantum dots

E. Zibik, T. Grange, B. Carpenter et al.

Phys. Rev. **B77**, 041307(R) (2008)

Coherent optoelectronics with single quantum dots

A. Zrenner, P. Ester, S. Michaelis de Vasconcellos, M. C. Hübner, L. Lackmann, S. Stufler, and M. Bichler

J. Phys: Condens. Matt. **20**, 454210 (2008)

7. Invited Talks

Gerhard Abstreiter

1. *Optical control of spins in single and coupled quantum dots*
Frontiers of Spintronics and Spin Coherent Phenomena in Semiconductors:
A Symposium in Honor of E. I. Rashba, Harvard University Cambridge MA,
Boston, USA (29.2.2008)
2. *Advanced GaAs based nanoscale structures and their potential use in quantum
information technology*
Int. Symp. on Secure Live Electronics, University of Tokyo, Japan (7.3.2008)
3. *Exzellenzcluster Nanosystems Initiative Munich – Nanoforschung im Münchener
Raum*
Symposium Markterfolg durch Spitzentechnologie: Nanotechnologie – Hype oder
Chance zur Wertsteigerung? Garching, Germany (13.3.2008)
4. *MBE growth of catalyst-free GaAs based nanowires*
UCSB Forschungsaufenthalt, Santa Barbara, USA (4.4.2008)
5. *Control of electron and hole spins in self-assembled InGaAs quantum dots*
53rd Conference on Magnetism and Magnetic Materials, Texas, Austin, USA
(11.11.2008)

Markus-Christian Amann

1. *Oberflächenemittierende Laserdioden für Nachrichtentechnik und Sensorik im nahen
Infrarot*
Universität Paderborn, Germany (5.2.2008)
2. *Basics of tunable lasers*
Workshop Laser and Spectroscopy, Universität Darmstadt, Germany (18.2.2008)
3. *Recent advances of long wavelength VCSELs*
Symposium Semiconductor Nanophotonics, DPG-Frühjahrstagung, Berlin, Germany
(25.2.08)
4. *Single-mode VCSELs*
Universität Karlsruhe, Germany (5.6.2008)
5. *Tunable single-mode VCSELs in the 1.3 – 2.3 μm wavelength range*
KTH Stockholm, Sweden (12.6.2008)
6. *Tunable near- and mid-infrared VCSELs for sensing and spectroscopy*
International Nano-Optoelectronic Workshop iNOW, Shonan Village, Japan
(11.8.2008)

7. *Single-mode and tunable VCSELs for communications and sensing*
University of California, USA (14.11.2008)

Alexander Bachmann

1. *Recent progress on electrically-pumped GaSb-based VCSELs emitting above 2 μm for sensing applications*
9th International Conference on Mid-Infrared Optoelectronics: Materials and Devices, Freiburg, Germany (10.9.2008)

Dominique Bougeard

1. *Germanium based magnetic semiconductors*
15th International Winterschool on New Developments in Solid State Physics, Bad Hofgastein, Austria (20.2.2008)

Martin S. Brandt

1. *Donor-based quantum computation: How to read the spin state and determine its decoherence*
Photonics West, San Jose, USA (22.1.2008)
2. *Donor-based quantum computation: How to read the spin state and determine its decoherence*
Lawrence Berkeley Laboratory, Berkeley, USA (25.1.2008)
3. *Donor-based quantum computation: How to read the spin state and determine its decoherence*
Materials Science Colloquium, University of Oxford, UK (7.2.2008)
4. *Beyond CMOS: Nanodevices for quantum computation*
4th International Nanotechnology Conference on Communication and Cooperation (INC4) Tokyo, Japan (15.4.2008)
5. *Donor-based quantum computation: How to read the spin state and determine its decoherence*
Keio University Yokohama, Japan (17.4.2008)
6. *Read-out of donor spin states for ensembles*
University of New South Wales Sydney, Australia (9.10.2008)
7. *Read-out of donor spin states for ensembles*
Physics Colloquium, University of Melbourne, Australia (14.10.2008)

Martin Eickhoff

1. *III-nitride quantum dot chemical sensor*
International Workshop on Nitride Semiconductors "IWN 2008", (6-10.10.2008)
Montreux, Switzerland
2. *Self assembly and properties of GaN nanostructures*
XXXVII. International School on the Physics of Semiconducting Compounds
Jaszowiec 2008, Jaszowiec, Poland (7.-13.6.2008)
3. *Biochemical analysis using group III-nitrides*
FUTUSENS International Workshop, Madrid, Spain (8.2.2008)

Jonathan Finley

1. *Non-resonant coupling of single quantum dots to photonic crystal nanocavities*
Frontiers in Nanoscale Science and Technology (FNST 2008), University of Basel,
Switzerland (6.-8.1.2008)
2. *Tunable quantum dot nanostructures for cavity-QED experiments*
Winterschool in Nanoscience, Bad Hofgastein, Austria (22.2.2008)
3. *Tunable quantum dot nanostructures for cavity-QED experiments*
QELS-08 International Conference, San Jose, California, USA (7.5.2008)
4. *Tunable quantum dot nanostructures for cavity-QED experiments*
ICTP-Workshop, Trieste, Italy (13.5.2008)
5. *Tunable quantum dot nanostructures for cavity-QED experiments*
EMRS-Strasbourg, France (27.5.2008)
6. *Tunable quantum dot nanostructures for cavity QED-experiments*
UK Semiconductors International Conference, Sheffield, U.K. (3.7.2008)
7. *Electrically tunable single dot nanocavities*
Bilateral Workshop on Nanoscale System, Technische Universität München, Germany
(10.7.2008)
8. *Tunable quantum dot nanostructures for cavity-QED experiments*
TUM-Keio University Joint Workshop, Technische Universität München, Germany
(15.9.2008)

9. *Introduction to fundamental properties of semiconductors and their low dimensional nanostructures*
10. *Single quantum dots: spectroscopy and coherent control*
11. *Optically probing charge and spin states in single and coupled QD-nanostructures*
12. *Tunable single dot nanostructures for cavity QED experiments*
4 Lectures at the Quantum & Nonlinear Optics PhD Summer School, Backfallsbyn, Hven, Sweden (24.-30.8.2008)
13. *Quantum optics with artificial atoms*
Physikalisches Kolloquium, Universität Graz, Austria (3.11.2008)
14. *Solid state cavity quantum electrodynamics*
Solid state quantum information workshop, Pisa, Italy (3.-6.12.2008)

Anna Fontcuberta i Morral

1. *Synthesis of catalyst-free semiconductor nanowires and their coaxial heterostructures*
Seminar of Laboratoire de Transport Electronique Quantique et Supraconductivité, CEA - Grenoble, France (1.2008)
2. *Synthesis of catalyst-free semiconductor nanowires and their coaxial heterostructures*
Nanosystems Initiative Munich Yearly Workshop, Germany (11.2.2008)
3. *Synthesis of catalyst-free semiconductor nanowires and their coaxial heterostructures*
Spring Meeting of the German Physical Society, Halbleiter-Physik-Symposium, Berlin, Germany (25.2.2008)
4. *Synthesis of catalyst-free semiconductor nanowires and their coaxial heterostructures*
Solid State Physics, The Nanometer Consortium, University of Lund, Sweden (11.6.2008)

Tonko Garma

1. *Introduction to nanotechnology*
Modern physics lectures, Technical University of Split, Split, Croatia (20.3.2008)
2. *Field effect and sensing devices on nano-scale,*
Technical University of Split, Split, Croatia (25.10.2008)

José Garrido

1. *Functionalization of diamond surfaces for bio-application*
19th European Conference on Diamond, Sitges, Spain (7-11.9.2008)

2. *Charge build-up at the diamond/water interface*
“Ion Specific Phenomena in Physics, Chemistry and Biology”, Garching, Germany
(15-17.9.2008)

Tobias Gründl

1. *Realisation of long wavelength lasers based on InP substrate*
Graduierten Kolleg, Darmstadt, Germany (4.12.2008)

Alexander Holleitner

1. *Optically induced transport phenomena in organic/inorganic nanosystems*
Seminar Chair of Prof. P. Lugli, Technische Universität München, Germany
(24.2.2008)
2. *Optisch induzierte Transportphänomene in organisch und anorganischen Nanosystemen*
Technische Universität, Carolo-Wilhelmina zu Braunschweig, Physikalisch-Chemisches Institut, Germany (25.2.2008)
3. *Mesoscopic optoelectronic transport across lithographically defined quantum wires*
Seminar, Universität Regensburg, Germany (14.4.2008)
4. *Optisch induzierte Transportphänomene in organischen und anorganischen Nanosystemen*
Physik-Seminar, Universität Regensburg, Germany (22.7.2008)
5. *Optically induced transport phenomena in organic and inorganic nanosystems*
CeNS Workshop 2008 on "Complex Nanosystems: Assembly, Control and Functionality" (29.9.-03.10.2008)
6. *Optically induced transport phenomena in organic and inorganic nanosystems*
Max-Bergmann Symposium 2008, Technische Universität Dresden, Germany
(4.-6.11.2008)
7. *Optisch induzierte Transportphänomene in organischen und anorganischen Nanosystemen*
Physik-Fakultätsseminar, Universität Dortmund, Germany (11.12.2008)

Tillman Kubis

1. *Predictive quantum theory of current and optical gain in quantum cascade lasers*
17th International Laser Physics Workshop, Trondheim, Norway (4.7.2008)

Arne Laucht

1. *Single quantum dots in photonic crystals*
TU Delft, The Netherlands (12.3.2008)

Leo Pecht

1. *Time-resolved photocurrent measurements on waveguide-circuits*
Universität Regensburg, Germany (14.4.2008)

Ulrich Rant

1. *Switchable DNA layers: Electrical interactions, molecular dynamics, and biosensing applications*
Humboldt Universität Berlin, Germany (9.12.2008)

Reinhard Scholz

1. *Spektroskopische Eigenschaften von Molekülkristallen*
Mathematisch-Naturwissenschaftliche Fakultät, Christian-Albrechts-Universität Kiel, Germany (15.5.2008)
2. *Zeitaufgelöste Photolumineszenzspektroskopie an organischen Halbleitern*
Institut für Physikalische und Theoretische Chemie, Rheinische Friedrich-Wilhelms-Universität Bonn, Germany (30.5.2008)
3. *Time-resolved photoluminescence spectroscopy on organic semiconductors*
Institut für angewandte Physik, Eberhard-Karls-Universität Tübingen, Germany (6.6.2008)
4. *Molecular crystals and their interfaces*
Physik-Department, Molekulare Nanowissenschaften & Chemische Physik von Grenzflächen, E20 Seminar, Technische Universität München, Germany (26.6.2008)
5. *Interference of Frenkel and charge transfer (CT) states: Absorption, PL, and PLE spectra of perylene compounds*
Tagung: Materials Science and Engineering, Nürnberg, 1.-4.9.2008, Germany (2.9.2008)
6. *Molecular crystals: A wonderful playground for Frenkel excitons and charge transfer states*
Theoretische Chemie, Technische Universität München, Germany (12.11.2008)

Martin Stutzmann

1. *Dotierte Silizium-Nanokristalle für druckbare Elektronik*
Kolloquium, Technische Universität Berlin, Germany (12.6.2008)
2. *Bioorganic layers on semiconductors: an introduction*
International WE Heraeus Physics School “Functional Hybrid Materials Design”,
Universität Bremen und Jacobs Universität, Bremen, Germany (18.6.2008)
3. *Novel bioelectronic devices*
International WE Heraeus Physics School “Functional Hybrid Materials Design”,
Universität Bremen und Jacobs Universität, Bremen, Germany (18.6.2008)
4. *Direct biofunctionalization of semiconductor surfaces for molecular biosensors*
Minerva Summer School “Molecules as Sensors”, Tsefat, Israel (17.9.2008)

Emanuele Uccelli

1. *Self assembly of ordered InAs chain of quantum dots and nanowire array*
Universität Regensburg, Germany (2.6.2008)

José Maria Villas-Boas

1. *Coherence and state control in self-assembled quantum dots system*
Theory Group Seminar, Max-Planck-Institut für Quantenoptik, Garching, Germany
(3.3.2008)

Ying Xiang

1. *Nanowires: template-assisted growth and structural characterizations*
Geballe Laboratory for Advanced Materials, Stanford University, USA (30.6.2008)

8. Courses, Seminars, and other Scientific Activities

Lectures

Gerhard Abstreiter

- WS 2007/2008 Physics of nanosystems I
- SS 2008 Halbleiterphysik II – Bauelementephysik
- WS 2008/2009 Festkörperspektroskopie
(together with Dominique Bougeard)

Markus-Christian Amann

- WS 2007/200 Werkstoffe der Elektrotechnik (Materials for electrical engineering)
- Technologie der III/V-Halbleiterbauelemente
(Technology of III/V semiconductor devices)
(together with Ralf Meyer)
- Optoelektronik II (Optoelectronics II)
- SS 2008 Optoelektronik I (Optoelectronics I)
- WS 2008/2009 Werkstoffe der Elektrotechnik (Materials for electrical engineering)
- Technologie der III/V-Halbleiterbauelemente
(Technology of III/V semiconductor devices)
(together with Ralf Meyer)
- Optoelektronik II (Optoelectronics II)

Dominique Bougeard

- WS 2008/2009 Festkörperspektroskopie
(together with Gerhard Abstreiter)

Martin S. Brandt

- WS 2007/2008 Magnetische Resonanz I: Grundlagen
- Seminar zu aktuellen Fragen der Magneto- und Spintronik
(together with Sebastian Gönnerwein)
- Seminar "Aktuelle Probleme der Halbleiterphysik"
- SS 2008 Quantum computing
- Seminar zu aktuellen Fragen der Magneto- und Spintronik
- Seminar "Aktuelle Probleme der Halbleiterphysik"
- WS 2008/2009 Grundlagen der Halbleiterphysik
- Tutorium zur Halbleiterphysik
- Seminar zu aktuellen Fragen der Magneto- und Spintronik
- Seminar "Aktuelle Probleme der Halbleiterphysik"

Jonathan Finley

- WS 2007/2008 Experimental physics I
- SS 2008 Experimental physics II
- WS 2008/2009 Experimental physics I

Anna Fontcuberta i Morral

- WS 2007/2008 Grundlagen der Halbleiterphysik
- SS 2008 Halbleiterphysik II - Physik niedrigdimensionaler Systeme

Seminar zur Festkörperspektroskopie

Seminar "Aktuelle Probleme der Halbleiterphysik"

SS 2008

Renewable energy II

Seminar zu "Renewable energy II"
(together with José Garrido)

NANO 301-1 Electronic properties of nanoengineered materials
Prof. Dr. Gerhard Abstreiter, Prof. Dr. Martin Stutzmann, Dr. José Antonio Garrido Ariza (together with Matthew Grayson)

JASS2008 - Joint Advanced Student Seminar 2008 on Frontiers of Nanotechnology, Sankt Petersburg, Russia

Seminar "Aktuelle Probleme der Halbleiterphysik"

WS 2008/2009

Renewable Energy I

Seminar zu "Renewable Energy"

Seminar „Aktuelle Probleme der Halbleiterphysik“

Peter Vogl

WS 2007/2008

Theoretical physics 2 (für Bachelor)

SS 2008

Theoretische Physik 5B – Thermodynamik

WS 2008/2009

Theoretical semiconductor physics I
(Theoretische Halbleiterphysik)

In der Schriftenreihe des Walter Schottky Instituts der Technischen Universität München sind bisher folgende Bände erschienen:

Vol. 1

Cornelia Engel

Si/SiGe basierende Phototransistoren

131 Seiten

ISBN 3-932749-01-4

Vol. 7

Markus Sexl

Verspannte und gitterrelaxierte

In(GaAl)As Heterostrukturen

144 Seiten

ISBN 3-932749-07-3

Vol. 2

Peter Schittenhelm

**Selbst-Organisation und Selbst-Ordnung
in Si/SiGe-Heterostrukturen**

151 Seiten

ISBN 3-932749-02-2

Vol. 8

Christian Obermüller

**Photolumineszenzspektroskopie mit
optischen Nahfeldmethoden an GaAs-
Nanostrukturen**

140 Seiten

ISBN 3-932749-08-1

Vol. 3

Andreas Nutsch

**Selektive Epitaxie von (GaIn)(AsP)
Schichtstrukturen**

129 Seiten

ISBN 3-932749-03-0

Vol. 9

Edilson Silveira

**Inelastische Lichtstreuung an niedrig-
dimensionalen Halbleiterstrukturen**

104 Seiten

ISBN 3-932749-09-X

Vol. 4

Peter Baumgartner

**Optische und elektronische Eigenschaften
lasergeschriebener GaAs-Nanostrukturen**

180 Seiten

ISBN 3-932749-04-9

Vol. 10

Eberhard Christian Rohrer

**Photoleitungs-Spektroskopie von
Diamant**

153 Seiten

ISBN 3-932749-10-03

Vol. 5

Walter Franz Rieger

**Untersuchung der elektronischen und
strukturellen Eigenschaften von
GaNAIN und deren Legierungen**

158 Seiten

ISBN 3-932749-05-7

Vol. 11

Thomas Wimbauer

**Magnetische Resonanz-Untersuchungen an
modernen Halbleitermaterialien**

125 Seiten

ISBN 3-932749-11-1

Vol. 6

Markus Hauser

**Oberflächenemittierende Laserdioden
mit Mehrfachepitaxie**

148 Seiten

ISBN 3-932749-06-5

Vol. 12

Herbert Verhoeven

**Thermische Eigenschaften von
CVD-Diamantschichten**

154 Seiten

ISBN 3-932749-12-X

- Vol. 13
Hans-Christoph Ostendorf
Trennung von Volumen- und Oberflächenrekombination in Silizium
128 Seiten
ISBN 3-932749-13-8
- Vol. 14
Martin Städele
Dichtefunktionaltheorie mit exaktem Austausch für Halbleiter
202 Seiten
ISBN 3-932749-14-6
- Vol. 15
Helmut Angerer
Herstellung von Gruppe III-Nitriden mit Molekularstrahlepitaxie
144 Seiten
ISBN 3-932749-15-4
- Vol. 16
Wolfgang Heller
Spektroskopie einzelner Quantenpunkte in magnetischen und elektrischen Feldern
128 Seiten
ISBN 3-932749-16-2
- Vol. 17
Molela Moukara
Pseudopotentiale mit exaktem Austausch
117 Seiten
ISBN 3-932749-17-0
- Vol. 18
Ralph Oberhuber
Elektronische Struktur und Transport in verspannten Halbleiterschichtsystemen
110 Seiten
ISBN 3-932749-18-9
- Vol. 19
Reiner Pech
High-Energy Boron-Implantation into Different Silicon Substrates
158 Seiten
ISBN 3-932749-19-7
- Vol. 20
Christoph Martin Engelhardt
Zyklotronresonanz zweidimensionaler Ladungsträgersysteme in Halbleitern, Effekte der Elektron-Elektron-Wechselwirkung und Lokalisierung
317 Seiten
ISBN 3-932749-20-0
- Vol. 21
Eduard Neufeld
Erbium-dotierte Si/SiGe-Lichtemitter und -Wellenleiter
136 Seiten
ISBN 3-932749-21-9
- Vol. 22
Gert Schedelbeck
Optische Eigenschaften von Halbleiternanostrukturen hergestellt durch Überwachsen von Spaltflächen
154 Seiten
ISBN 3-932749-22-7
- Vol. 23
Jürgen Zimmer
Optoelektronisches Verhalten von Dünnschichtbauelementen aus amorphem und mikrokristallinem Silizium
171 Seiten
ISBN 3-932749-23-5
- Vol. 24
Berthold Schmidt
Leistungsoptimierung abstimmbarer InGaAsP/InP Halbleiterlaser
85 Seiten
ISBN 3-932749-24-3
- Vol. 25
Jianhong Zhu
Ordering of self-assembled Ge and SiGe nanostructures on vicinal Si surfaces
120 Seiten
ISBN 3-932749-25-1

- Vol. 26
Gerhard Groos
Herstellung und Charakterisierung von Silizium-Nanostrukturen
168 Seiten
ISBN 3-932749-26-X
- Vol. 27
Uwe Hansen
Theorie der Reaktionskinetik an Festkörperoberflächen
119 Seiten
ISBN 3-932749-27-8
- Vol. 28
Roman Dimitrov
Herstellung und Charakterisierung von AlGaIn/GaN-Transistoren
196 Seiten
ISBN 3-932749-28-6
- Vol. 29
Martin Eickhoff
Piezowiderstandsmechanismen in Halbleitern mit großer Bandlücke
151 Seiten
ISBN 3-932749-29-4
- Vol. 30
Nikolai Wieser
Ramanspektroskopie an Gruppe III-Nitriden
161 Seiten
ISBN 3-932749-30-8
- Vol. 31
Rainer Janssen
Strukturelle und elektronische Eigenschaften amorpher Silizium-Suboxide
275 Seiten
ISBN 3-932749-31-6
- Vol. 32
Martin W. Bayerl
Magnetic resonance investigations of group III-nitrides
155 Seiten
ISBN 3-932749-32-4
- Vol. 33
Martin Rother
Elektronische Eigenschaften von Halbleiternanostrukturen hergestellt durch Überwachsen von Spaltflächen
196 Seiten
ISBN 3-932749-33-2
- Vol. 34
Frank Findeis
Optical spectroscopy on single self-assembled quantum dots
156 Seiten
ISBN 3-932749-34-0
- Vol. 35
Markus Ortsiefer
Langwellige Vertikalresonator-Laserdioden im Materialsystem InGaAlAs/InP
152 Seiten
ISBN 3-932749-35-9
- Vol. 36
Roland Zeisel
Optoelectronic properties of defects in diamond and AlGaIn alloys
140 Seiten
ISBN 3-932749-36-7
- Vol. 37
Liwen Chu
Inter- und Intradband Spektroskopie an selbstorganisierten In(Ga)As/GaAs Quantenpunkten
124 Seiten
ISBN 3-932749-37-5
- Vol. 38
Christian Alexander Miesner
Intra-Valenzbandspektroskopie an SiGe-Nanostrukturen in Si
100 Seiten
ISBN 3-932749-38-3
- Vol. 39
Szabolcs Kátai
Investigation of the nucleation process of chemical vapour deposited diamond films
178 Seiten
ISBN 3-932749-39-1

- Vol. 40
Markus Arzberger
Wachstum, Eigenschaften und Anwendungen selbstorganisierter InAs-Quantenpunkte
236 Seiten
ISBN 3-932749-40-5
- Vol. 41
Markus Oliver Markmann
Optische Eigenschaften von Erbium in Si/Si_{1-x}C_x, Si/Si_{1-x}Ge_x und Si/SiO_x Heterostrukturen
182 Seiten
ISBN 3-932749-41-3
- Vol. 42
Rainer Alexander Deutschmann
Two dimensional electron systems in atomically precise periodic potential
210 Seiten
ISBN 3-932749-42-1
- Vol. 43
Uwe Karrer
Schottky-Dioden auf Galliumnitrid: Eigenschaften und Anwendungen in der Sensorik
182 Seiten
ISBN 3-932749-43-X
- Vol. 44
Günther Anton Johann Vogg
Epitaxial thin films of Si and Ge based Zintl phases and sheet polymers
169 Seiten
ISBN 3-932749-44-8
- Vol. 45
Christian Strahberger
Vertikaler Transport und extreme Magnetfelder in Halbleitern
167 Seiten
ISBN 3-932749-45-6
- Vol. 46
Jan Schalwig
Feldeffekt-Gassensoren und ihre Anwendung in Abgasnachbehandlungssystemen
125 Seiten
ISBN 3-932749-46-4
- Vol. 47
Christopher Eisele
Novel absorber structures for Si-based thin film solar cells
126 Seiten
ISBN 3-932749-47-2
- Vol. 48
Stefan Hackenbuchner
Elektronische Struktur von Halbleiter-Nanobaelementen im thermodynamischen Nichtgleichgewicht
213 Seiten
ISBN 3-932749-48-0
- Vol. 49
Andreas Sticht
Herstellung und Charakterisierung von dünnen Silizium/Siliziumoxid-Schichtsystemen
166 Seiten
ISBN 3-932749-49-9
- Vol. 50
Giuseppe Scarpa
Design and fabrication of Quantum Cascade Lasers
193 Seiten
ISBN 3-932749-50-2
- Vol. 51
Jörg Frankenberger
Optische Untersuchungen an zwei-dimensionalen Ladungsträgersystemen
158 Seiten
ISBN 3-932749-51-0

- Vol. 52
Doris Heinrich
Wavelength selective optically induced charge storage in self-assembled semiconductor quantum dots
144 Seiten
ISBN 3-932749-52-9
- Vol. 53
Nicolaus Ulbrich
Entwurf und Charakterisierung von Quanten-Kaskadenlasern und Quantenpunktkaskaden
133 Seiten
ISBN 3-932749-53-7
- Vol. 54
Lutz Carsten Görgens
Analyse stickstoffhaltiger III-V Halbleiter-Heterosysteme mit hochenergetischen schweren Ionen
116 Seiten
ISBN 3-932749-54-5
- Vol. 55
Andreas Janotta
Doping, light-induced modification and biocompatibility of amorphous silicon suboxides
180 Seiten
ISBN 3-932749-55-3
- Vol. 56
Sebastian Tobias Benedikt Gönnerwein
Two-dimensional electron gases and ferromagnetic semiconductors: materials for spintronics
198 Seiten
ISBN 3-932749-56-1
- Vol. 57
Evelin Beham
Photostromspektroskopie an einzelnen Quantenpunkten
186 Seiten
ISBN 3-932749-57-X
- Vol. 58
Po-Wen Chiu
Towards carbon nanotube-based molecular electronics
116 Seiten
ISBN 3-932749-58-8
- Vol. 59
Tobias Graf
Spin-spin interactions of localized electronic states in semiconductors
194 Seiten
ISBN 3-932749-59-6
- Vol. 60
Stefan Klein
Microcrystalline silicon prepared by hot wire CVD: preparation and characterization of material and solar cells
157 Seiten
ISBN 3-932749-60-X
- Vol. 61
Markus Krach
Frequenzverdreifacher mit Anti-Seriellen Schottky-Varaktor für den Terahertzbereich
156 Seiten
ISBN 3-932749-61-8
- Vol. 62
Ralph Thomas Neuberger
AlGaIn/GaN-Heterostrukturen als chemische Sensoren in korrosiven Medien
153 Seiten
ISBN 3-932749-62-6
- Vol. 63
Sonia Perna
Wasserstoff-Passivierung von tri-kristallinem Silizium durch hydrogenisiertes Siliziumnitrid
136 Seiten
ISBN 3-932749-63-4

- Vol. 64
Oliver Schumann
Einfluss von Stickstoff auf das Wachstum und die Eigenschaften von InAs-Quantenpunkten
148 Seiten
ISBN 3-932749-64-2
- Vol. 65
Gerhard Rösel
Entwicklung und Charakterisierung von Typ-II-Heterostrukturen für die Abstimmregion in abstimmbaren Laserdioden
101 Seiten
ISBN 3-932749-65-0
- Vol. 66
Angela Link
Zweidimensionale Elektronen- und Löcher-Gase in GaN/AlGaN Heterostrukturen
156 Seiten
ISBN 3-932749-66-9
- Vol. 67
Matthias Sabathil
Opto-electronic and quantum transport properties of semiconductor nanostructures
156 Seiten
ISBN 3-932749-67-7
- Vol. 68
Frank Fischer
Growth and electronic properties of two-dimensional systems on (110) oriented GaAs
139 Seiten
ISBN 3-932749-68-5
- Vol. 69
Robert Shau
Langwellige oberflächenemittierende Laserdioden mit hoher Ausgangsleistung und Modulationsbandbreite
198 Seiten
ISBN 3-932749-69-3
- Vol. 70
Andrea Baumer
Structural and electronic properties of hydrosilylated silicon surfaces
163 Seiten
ISBN 3-932749-70-7
- Vol. 71
Andreas Florian Kreß
Manipulation of the Light-Matter-Interaction in Photonic Crystal Nanocavities
185 Seiten
ISBN 3-932749-71-5
- Vol. 72
Markus Grau
Molekularstrahlepitaktische Herstellung von antimonidischen Laserdioden für die Gassensorik
138 Seiten
ISBN 3-932749-72-3
- Vol. 73
Karin Buchholz
Microprocessing of silicon on insulator substrates and biofunctionalisation of silicon dioxide surfaces for sensing applications in fluids
170 Seiten
ISBN 3-932749-73-1
- Vol. 74
Dominique Bougeard
Spektroskopische Charakterisierung von Germanium-Quantenpunkten in Silizium
154 Seiten
ISBN 3-932749-74-X
- Vol. 75
Jochen Bauer
Untersuchungen zum kontrollierten Wachstum von InAs-Nanostrukturen auf Spaltflächen
140 Seiten
ISBN 3-932749-75-8
- Vol. 76
Ingo Bormann
Intersubband Spektroskopie an Silizium-Germanium Quantenkaskadenstrukturen
124 Seiten
ISBN 3-932749-76-6

- Vol. 77
Hubert Johannes Krenner
Coherent quantum coupling of excitons in single quantum dots and quantum dot molecules
160 Seiten
ISBN 3-932749-77-4
- Vol. 78
Ulrich Rant
Electrical manipulation of DNA-layers on gold surfaces
249 Seiten
ISBN 3-932749-78-2
- Vol. 79
René Todt
Widely tunable laser diodes with distributed feedback
152 Seiten
ISBN 3-932749-79-0
- Vol. 80
Miroslav Kroutvar
Charge and spin storage in quantum dots
150 Seiten
ISBN 3-932749-80-4
- Vol. 81
Markus Maute
Mikromechanisch abstimmbare Laser-Dioden mit Vertikalresonator
170 Seiten
ISBN 3-932749-81-2
- Vol. 82
Frank Ertl
Anisotrope Quanten-Hall-Systeme, Vertikale Ultrakurzkanal- und Tunneltransistoren
170 Seiten
ISBN 3-932749-82-0
- Vol. 83
Sebastian M. Lubber
III-V semiconductor structures for biosensor and molecular electronics applications
212 Seiten
ISBN 978-3-932749-83-4
- Vol. 84
Claudio Ronald Miskys
New substrates for epitaxy of group III nitride semiconductors: challenges and potential
207 Seiten
ISBN 978-3-932749-84-1
- Vol. 85
Sebastian Friedrich Roth
n- and p-type transport in (110) GaAs substrates, single- and double-cleave structures
138 Seiten
ISBN 978-3-932749-85-8
- Vol. 86
Mario Gjukic
Metal-induced crystallization of silicon-germanium alloys
309 Seiten
ISBN 978-3-932749-86-5
- Vol. 87
Tobias Zibold
Semiconductor based quantum information devices: Theory and simulations
151 Seiten
ISBN 978-3-932749-87-2
- Vol. 88
Thomas Jacke
Weit abstimmbare Laserdiode mit vertikal integriertem Mach-Zehnder-Interferometer
165 Seiten
ISBN 978-3-932749-88-9
- Vol. 89
Nenad Ocelić
Quantitative near-field phonon-polariton spectroscopy
174 Seiten
ISBN 978-3-932749-89-6

Vol. 90
 Kenji Arinaga
Control and manipulation of DNA on gold and its application for biosensing
 111 Seiten
 ISBN 978-3-932749-90-2

Vol. 91
 Hans-Gregor Hübl
Coherent manipulation and electrical detection of phosphorus donor spins in silicon
 162 Seiten
 ISBN 978-3-932749-91-9

Vol. 92
 Andrea Friedrich
Quanten-Kaskaden-Laser ohne Injektorbereiche
 140 Seiten
 ISBN 978-3-932749-92-6

Vol. 93
 Oliver Dier
Das Materialsystem (AlGaIn) (AsSb): Eigenschaften und Eignung für GaSb-basierte Vertikalresonator-Laserdioden
 174 Seiten
 ISBN 978-3-932749-93-3

Vol. 94
 Georg Steinhoff
Group III-nitrides for bio- and electro-Chemical sensors
 197 Seiten
 ISBN 978-3-932749-94-0

Vol. 95
 Stefan Harrer
Next-generation nanoimprint lithography: Innovative approaches towards improving flexibility and resolution of nanofabrication in the sub-15-nm region
 161 Seiten
 ISBN 978-3-932749-95-7

Vol. 96
 Stefan Ahlers
Magnetic and electrical properties of epitaxial GeMn
 184 Seiten
 ISBN 978-3-932749-96-0

Vol. 97
 Emanuele Uccelli
Guided self-assembly of InAs quantum dots arrays on (110) surfaces
 172 Seiten
 ISBN 978-3-932749-97-1

Vol. 98
 Shavaji Dasgupta
Growth optimization and characterization of high mobility two-dimensional electron systems in AlAs quantum wells
 152 Seiten
 ISBN 978-3-932749-98-8

Important addresses

Walter Schottky Institut
Technische Universität München
Am Coulombwall 3
85748 Garching
Germany
www-address: <http://www.wsi.tum.de>

Secretaries:

Veronika Enter
Tel.: ++49-89-289 12761, Fax: ++49-89-289 12737, e-mail: veronika@wsi.tum.de

Daniela Huber
Tel.: ++49-89-289 12781, Fax: ++49-89-320 6620, e-mail: d.huber@wsi.tum.de

Regina Morinaga (NIM)
Tel.: ++49-89-289 12782, Fax: ++49-89-320 6620, e-mail: regina.morinaga@wsi.tum.de

Irmgard Neuner
Tel.: ++49-89-289 12771, Fax: ++49-89-320 6620, e-mail: irmgard@wsi.tum.de

Liane Lindner (SFB 631)
Tel.: ++49-89-289 12751, Fax: ++49-89-289 12737, e-mail: liane@wsi.tum.de

Faculty Members and Scientific Staff

Gerhard Abstreiter
Tel.: ++49-89-289 12770, Fax: ++49-89-320 6620, e-mail: abstreiter@wsi.tum.de

Markus-Christian Amann
Tel.: ++49-89-289 12780, Fax: ++49-89-320 6620, e-mail: mcamann@wsi.tum.de

Martin Brandt
Tel.: ++49-89-289 12758, Fax: ++49-89-289 12737, e-mail: brandt@wsi.tum.de

Jonathan Finley
Tel.: ++49-89-289 12782, Fax: ++49-89-320 6620, e-mail: finley@wsi.tum.de

Alexander Holleitner
Tel.: ++49-89-289 12775, Fax: ++49-89-320 6620, e-mail: holleitner@wsi.tum.de

Martin Stutzmann

Tel.: ++49-89-289 12760, Fax: ++49-89-289 12737, e-mail: stutz@wsi.tum.de

Peter Vogl

Tel.: ++49-89-289 12750, Fax: ++49-89-289 12737, e-mail: vogl@wsi.tum.de

Gerhard Böhm

Tel.: ++49-89-289 12791, Fax: ++49-89-320 6620, e-mail: boehm@wsi.tum.de

Dominique Bougeard

Tel.: ++49-89-289 12777, Fax: ++49-89-320 6620, e-mail: bougeard@wsi.tum.de

Martin Eickhoff

Tel.: ++49-89-289 12889, Fax: ++49-89-289 12737, e-mail: eickhoff@wsi.tum.de

Anna Fontcuberta i Morral

Tel.: ++49-89-289 12779, Fax: ++49-89-320 6620, e-mail: annafm@wsi.tum.de

Jürgen Freyer

Tel.: ++49-89-289 12789, Fax: ++49-89-320 6620, e-mail: freyer@wsi.tum.de

José Antonio Garrido Ariza

Tel.: ++49-89-289 12766, Fax: ++49-89-289 12737, e-mail: garrido@wsi.tum.de

Ralf Meyer

Tel.: ++49-89-289 12790, Fax: ++49-89-320 6620, e-mail: meyer@wsi.tum.de

Ulrich Rant

Tel.: ++49-89-289 12776, Fax: ++49-89-320 6620, e-mail: rant@wsi.tum.de

Reinhard Scholz

Tel.: ++49-89-289 12752, Fax: ++49-89-289 12737, e-mail: reinhard.scholz@wsi.tum.de